Computational Modelling Study on the Stability of $Li_{1.2}Mn_{0.8}O_2$ Cathode Material

By

Vusani Mikosi

Research dissertation

Submitted in fulfilment of the requirements for the degree of

Master of Science

In

Physics

In the

Faculty of Science and Agriculture

School of Physical and Mineral Sciences

At the

University of Limpopo

Supervisor: Prof P.E Ngoepe

Co-supervisor: Dr K.T Malatji

: Dr N.N Ngoepe

2024

Abstract

Lithium-ion batteries are significant rechargeable power sources for use in various electronic devices and electric vehicles due to their high specific energy and high energy density. The cathode material of lithium-ion batteries greatly influences specific energy, lifespan, and safety since they possess a minimised specific capacity and a more unstable structure than anode materials. As a result, it is crucial to develop high performance cathode materials.

Lithium-rich Mn-based layered oxides have been extensively investigated as possible cathodes with high capacity of over 250mAh/g, low cost, safety, and long lifetime for lithium-ion batteries, however, commercial applications of these cathodes are mainly hindered by voltage fade, irreversible oxygen loss, structural transition, and low coulombic efficiency which results in poor cycling performance. To solve these challenges, many approaches have been used, including elemental doping, surface modification, anionic doping, and coating. Nevertheless, finding suitable cathode materials with appropriate characteristics and stable structural compositions is still difficult, and as such, materials such as Li_2MnO_3, $LiMnO_2$, $LiNiO_2$, and $LiCoO_2$ are being studied for a satisfactory outcome.

This study merges computational and experimental methods to study the stability of the $Li_{1.2}Mn_{0.8}O_2$ cathode material which is derived from the promising cathode material Li_2MnO_3. Firstly, structural, electronic, and mechanical properties of $Li_{1.2}Mn_{0.8}O_2$ were calculated using the density functional theory within the Vienna ab initio simulation package implementing the generalized gradient approximation functionals.

It was found that the $Li_{1.2}Mn_{0.8}O_2$ material is thermodynamically stable with a negative heat of formation, it was also found to be a semi-conductor with a band gap of 0.269eV at the Fermi level. Moreover, the structure was found to be mechanically stable under a strain of 0.001 and mechanically unstable under larger strains 0.005 and 0.025. In addition, the Pugh ratio predicted the material to be brittle.

Secondly, the material was doped with Nickel on the manganese sites and also doped with fluorine on the oxygen sites to study the effects of these elements on the material $Li_{1.2}Mn_{0.8}O_2$. First-principles calculations coupled with cluster expansion simulations were performed on the doped structures to generate new phases of the doped material. The

cluster expansion generated 12, 78, and 165 new phases for the Ni-doped $Li_{1.2}Mn_{0.8}O_2$, F-doped $Li_{1.2}Mn_{0.8}O_2$, and F-doped $Li_{1.2}Mn_{0.6}Ni_{0.2}O_2$ structures respectively. It was observed that doping $Li_{1.2}Mn_{0.8}O_2$ with Ni enhances the thermodynamic stability of the material and improves the material's conductivity as it led to a magnetic metal with no bandgap. We further observed that the presence of Ni in the structure does not compromise the mechanical stability of the material as the generated phases were found to be mechanically stable. However, the Ni-doped phases are more brittle than the pristine structure suggesting that introducing Ni into the material reduces the ductility of the material.

From the F-doped materials it was found that the presence of fluorine in the material increases the thermodynamic stability of the material. Consequently, the generated materials retain the pristine structure's electronic conductivity as they show metallic behaviour. Furthermore, it was found that only a minimum concentration of fluorine is required for the material to be mechanically stable, in addition, the presence of fluorine has the potential to improve the ductility of the material.

Experimentally a co-precipitation method was used to generate precursors for the $Li_{1.2}Mn_{0.8}O_2$, $Li_{1.2}Mn_{0.6}Ni_{0.2}O_2$, and $Li_{1.2}Mn_{0.4}Ni_{0.2}Co_{0.2}O_2$ structures using the semi-batch technique. Morphology of the samples was studied with the Scanning Electron Microscopy (SEM). The SEM analysis of the material $Li_{1.2}Mn_{0.8}O_2$ showed spherical shaped particles. With $Li_{1.2}Mn_{0.6}Ni_{0.2}O_2$ the morphology analysis revealed primary particles with irregular shapes, and which agglomerate into secondary particles with spherical shapes. The $Li_{1.2}Mn_{0.4}Ni_{0.2}Co_{0.2}O_2$ particles also showed spherical particles and empty spaces in between the agglomerated particles. The measured tapped density ($1.43 g/cm^3$) of the $Li_{1.2}Mn_{0.6}Ni_{0.2}O_2$ material was consistent with the tapped density value reported in literature, and this suggests the accuracy of the synthesis method. Furthermore, particle size distribution analysis was performed on the $Li_{1.2}Mn_{0.6}Ni_{0.2}O_2$ material and it was found that D10=14.29µm, D50=22.95µm, and D90=33.16µm.

Declaration

I declare that the dissertation hereby submitted to the University of Limpopo for the degree of Master of science (physics) has not been previously submitted by me for a degree at this or any other university; that it is my work in design and execution, and that all material contained herein has been duly acknowledged.

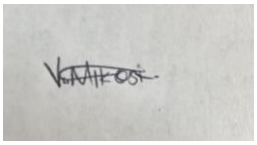

Mikosi V

22/12/2023
Date

Acknowledgement

I would like to express my sincere gratitude to my supervisors Dr Malatji, Dr Ngoepe, and Prof Ngoepe for the immeasurable guidance, support, and enlightening discussions they provided throughout the project.

I am thankful to the National Research Foundation for financial support. I would like to thank the Centre for High Performance Computing (CHPC) Cape Town and Materials Modelling Centre at the University of Limpopo for computing recourses. Lastly, I would like to thank the University of Limpopo for the studying opportunity.

Table of Contents

Abstract **2**
Acknowledgement **5**
Chapter 1 ..... **9**
1.1 General background **9**
1.1.1 Lithium-ion batteries 9
1.1.2 Cathode materials for Lithium-ion batteries 10
1.2 Literature review **12**
1.3 Structures **16**
1.4 Background of Properties to be Investigated. **17**
1.4.1 Heats of Formation 17
1.4.2 Mechanical properties 17
1.4.3 Density of States 18
1.5 Rationale **20**
1.6 Aim **21**
1.7 Objectives **21**
1.8 Outline of the study **22**
Chapter 2 ..... **23**
2.1 Density Functional Theory **23**
2.2 Approximation Methods **25**
2.2.1 Local Density Approximation (LDA) 25
2.2.2 Generalized Gradient Approximation 26
2.3 K-Sampling **27**
2.4 VASP Code **28**
2.5 Cluster Expansion **29**
2.5.1 Genetic Algorithm selection 30
2.6 Experimental methodology **31**
2.6.1 Synthesis 31
2.6.1.1 Chemical reactor 31
2.5.2 Analysis 33
2.5.2.1 X-ray powder diffraction (XRD) 33
2.5.2.2 Scanning electron microscope (SEM) 34
2.5.2.3 X-ray Fluorescence (XRF) 36
Chapter 3 ..... **39**

Structural, Mechanical, and Electronic Properties of $Li_{1.2}Mn_{0.8}O_2$ and Li_2MnO_3. 39
3.1 Cut-off energy and K-points convergence 39
3.1.1 Cut-off energy 39
3.1.2 K-points 41
3.2 Lattice Parameters and Heats of Formation 44
3.3 Mechanical Properties 45
3.4 Density of states 47
3.5 Band structure 50
Structural, Mechanical, and Electronic Properties of $Li_{1.2}Mn_{0.6}Ni_{0.2}O_2$ 52
3.6 Lattice Parameters and Heats of Formation. 52
3.7 Mechanical properties 53
3.8 Density of states 55
Structural, Mechanical, and Electronic properties of $Li_{1.2}Mn_{0.3}Ni_{0.5}O_2$. 57
3.9 Lattice Parameters and Heats of Formation. 57
3.10 Mechanical properties 58
3.11 Density of states 60
Structural, mechanical, and electronic properties of Co-doped $Li_{1.2}Mn_{0.6}Ni_{0.2}O_2$ clusters. 62
3.12 Structural analysis 62
3.13 Mechanical properties 63
3.14 Density of states ..... Error! Bookmark not defined.
3.15 Fluorination 65
3.15.1 $Li_{1.2}Mn_{0.8}O_2F_2$ 65
3.15.1.1 Density of states 68
3.15.1.2 Mechanical properties 72
3.15.2 $Li_{1.2}Mn_{0.6}Ni_{0.2}O_2F_2$ 75
3.15.2.1 Density of states 77
3.15.2.2 Mechanical properties 79
Chapter 4 82
4.1 Cluster Expansion 82
4.1.1 Ni-doped $Li_{1.2}Mn_{0.8}O_2$ cluster expansion 82
4.1.2 F-doped $Li_{1.2}Mn_{0.8}O_2$ cluster expansion 84
4.1.3 F-doped $Li_{1.2}Mn_{0.6}Ni_{0.2}O_2$ cluster expansion 86
4.1.4 Co-doped $Li_{1.2}Mn_{0.6}Ni_{0.2}O_2$ cluster expansion 89
Chapter 5 93

Experimental results. **93**
5.1 Tapped density. **93**
$Li_{1.2}Mn_{0.6}Ni_{0.2}O_2$ **93**
5.2 XRF analyses **94**
5.3 SEM analyses **97**
5.4 Particle size distribution **99**
References **103**

Chapter 1

Introduction

1.1 General background

1.1.1 Lithium-ion batteries

The increasing demand and use of energy is gradually leading to the depletion of fossil fuels and at the same time leads to various environmental issues such as global warming. The use of clean and new energy, as well as the associated energy storage technologies is thus of great importance to human society's maintainable development. Because of high specific capacity, long cycle life, and environmental friendliness, rechargeable batteries have emerged as the primary powering technology in recent decades [1].

LIBs are rechargeable batteries that possess high energy power density, have a long-life span, have high charge, and discharge rates, and have moderately low maintenance [2], as such they attract wide interest as renewable energy storage systems. The cycle life of LIBs can be greater than 10000 cycles depending on the depth of their charge and discharge, yielding energy densities of about 250 $Whkg^{-1}$ [3]. Their significant success in portable devices shows potential in static energy storage as their cost tends to reduce and their safety and cycling life problems are improved. Their dominance and significance come from their high energy densities when compared to other battery technologies for use in electric, hybrid, and plug-in hybrid vehicles [4].

However, the need for more durable devices and longer-range electric vehicles per charge/discharge cycle encourages the continuing development of LIBs to improve on present state-of-the-art LIBs [5]. Several critical components, like a cathode and anode materials, electrolyte, separators, and presentation or packaging, influence the performance of a LIB at the cell level and it is understood that the fundamental limitation for generating high-energy and low-cost LIBs is currently cathode materials [6].

1.1.2 Cathode materials for Lithium-ion batteries

Even though the global commercial demand for LIBs continues to surge, the problem is to produce LIBs with much longer life spans and higher energy density. Research around good cathode materials to overcome these challenges has been ongoing and Goodenough [7] and colleagues anticipated the tremendous future promise of transition metal oxides in 1980 and identified layered $LiCoO_2$ as a viable cathode material for LIBs [8].

After commercialization of this cathode material, studies for alternative electrode materials with higher energy densities has escalated in recent years. Layered oxides, spinel oxides, and polyanion compound such $LiNi_{0.8}Co_{0.1}Mn_{0.1}O_2$ $LiMn_2O_4$, and $LiFePO_4$, and have been extensively studied and used in large-scale LIBs as substitutes for $LiCoO_2$ [8].

The most popular cathode materials for LIBs are the layered oxides. These materials compose of a general formula $LiMO_2$ where M is the transition metal Mn, Ni, or Co. Within the lattice of the $LiMO_2$ structure, the Li and the transition metal occupy the 3a and 3b sites respectively forming an ABC stacking sequence [9]. These layered oxides have garnered widespread study attention as positive electrodes for LIBs owing to their high capacity, high energy density, rate capability, and high output voltage [10].

For layered oxides with Co as the transition metal i.e., $LiCoO_2$, the theoretical capacity is high (274 $mAhg^{-1}$), and it is twice the practical capacity which is 135 $mAhg^{-1}$. However, the toxicity and high cost of this material has resulted in the development of alternative Ni-based layered oxides. The Ni based cathode possesses high energy density and gives a higher reversible capacity than $LiCoO_2$, nonetheless, it is difficult to achieve their stochiometric synthesis and they have an unstable crystalline structure [11]. Lastly there is the Mn-based material. This is cheaper than the Co and Ni based layered cathodes. The $LiMnO_2$ is easy to synthesize, and it has a practical capacity of 200mAhg-1 in the voltage range 2.5-4.3V. However, the material suffers from structural transformation, capacity loss, and structural degradation [12].

The second type of cathode materials for LIBs is the spinel oxides. $LiMn_2O_4$ was reported as the first spinel oxide cathode material for LIBs in 1980 by Michael Thackeray [13]. This material possesses fast intercalation and deintercalation rates of Li^+ ion, and it is also

cheap to prepare. $LiMn_2O_4$ has a face-centred cubic packing that is generated by anions situated at the 32e Wyckoff position [9]. It is thought that this material is one of the most suitable cathode materials for LIBs due to its high operation potential, safety, and the abundance of its components [14]. The spinel structure, however, suffers from rapid capacity decay at high temperatures which hinders its application in large scale systems. Furthermore, it suffers from oxygen evolution and Mn dissolution which results in irreversible damage of the structure [15].

Lastly there is the polyanion compounds, these are a moderately new group of cathode materials which was originally reported by Goodenough and Manthiram [16] [17]. Polyanions have a general formula of $LiM(XO_4)^{3-}$ where (M= Fe, Ni, Co, and Mn) and (X= Ar, W, P, Si, Mo). The most common polyanion is $LiFePO_4$ which is an olivine structure. This material can deliver high power densities and it also exhibits good structural and thermal stability. It exhibits a constant redox potential of 3.5V (vs Li^+/Li) and an elevated theoretical capacity of 170 $mAhg^{-1}$. However, it suffers from low electrical conductivity which limits its utilization as a cathode material [9].

1.2 Literature review

High-energy lithium-rich manganese-based layered cathode materials are among the most promising options for lithium-ion battery cathode materials. As a result of, numerous electron transfers including both cationic and anionic redox processes, these cathode materials can give extraordinarily high capacity [18].

Li_2MnO_3, being a member of the lithium-rich and manganese-rich layered oxide group, has been regarded as a possible cathode material due to its ability produce capacities of 250 mAh/g or higher and because of its high voltage [19]. However, Li_2MnO_3 encounters the critical issues of inadequate rate capacity, capacity degradation, and oxygen evolution in practical applications [19] which is due to the Mn oxidation state (+4) in Li_2MnO_3 which does not participate in the redox reactions when charging and discharging occurs [20].

Li_2MnO_3 suffers from poor cycling performance caused by the structural transition from layered to spinel structure throughout the charge/discharge process. Layered Li_2MnO_3 conforms to the C2/m symmetry in which Li and Mn ions fill the octahedral interstices of a cubic close-packed oxygen lattice [21]. The electrochemical reaction mechanism of the compound is a two-step mechanism. When the Li_2MnO_3 component is charged to 4.5V, it loses Li^+ and the corresponding quantity of oxygen, leading to a net loss of Li_2O and the formation of the electrochemically layered MnO_2 component. Then the as-formed MnO_2 constituent intercalate/de-intercalate Li^+ in the discharge/charge process [22].

Xiao et al., conducted a thorough computational analysis of the electronic structure, redox mechanism, de-lithiation process, lithium diffusion kinetics, and structural stability of Li_2MnO_3. Their findings confirmed the low intrinsic electrical conductivity of Li_2MnO_3 and indicated that doping might provide a scientific solution to the low conductivity problem in practical applications [23]. Doping enhances the electrochemical performance of the electrode material of lithium-ion batteries. Furthermore, many studies have shown that doping can improve the overall performance of cathode materials [24]. Research has been done on doping Li_2MnO_3 with various transition metals. Xiao et al., reported that substituting Mn with Ti increases band gap and prevents oxygen loss, meanwhile, doping with Co increases oxygen loss [23]. Doping with Cr improves the lithium-ion diffusion in Li_2MnO_3, but because of the toxicity of Cr, its applications can be limited in commercial products [25]**.** Gao et al., conducted a first principles calculation which showed that doping

with Mo can improve lithium-ion diffusion while suppressing O_2 releasing reactions. Their findings were later confirmed by their experiments [23].

To improve this material, derivatives of Li_2MnO_3 such as $Li_{1.2}Ni_{0.2}Mn_{0.6}O_2$ have recently been of high interest in research due to high initial discharge capacity, while difficulties of capacity loss and voltage degradation caused by layered to spinel structural transitions have not yet been overcome significantly [26]. As a result, it is crucial to research alternative cathode materials with the chemical composition of $Li_{1.2}Ni_xMn_{0.8-x}O_2$ and determine other parameters influencing discharge capacity and voltage decay, as well as what measures should be made to enhance the structure [26].

Mengchu et al., examined the impact of surface K^+ doping on $Li_{1.2}Ni_{0.2}Mn_{0.6}O_2$ in an attempt to mitigate voltage decay in the cathode material. Upon studying the electrochemical behaviour of the K^+ doped $Li_{1.2}Ni_{0.2}Mn_{0.6}O_2$ (KLMNO) and pure $Li_{1.2}Ni_{0.2}Mn_{0.6}O_2$ (LMNO) during cycling, they discovered that at 3.8V the KLMNO has a sharp oxidation peak followed by a shoulder at 4.1V and futhermore shows a reduced peak at 4.7V implying that K^+ doping has the potential to successfully reduce irreversible LiO_2 removal and consequently mitigating the release of O_2 surface unlike with LMNO which shows a sharp anodic peak at 4.7V due to the activation of the Li_2MnO_3 phase with loss of LiO_2 resulting in structural transformation [27]. However, structural aspects of the oxygen dimer creation through out the anionic redox activity in $Li_{1.2}Ni_{0.2}Mn_{0.6}O_2$ has not yet been thouroughly investigated, particularly the factors leading to oxygen evolution from the cathode surface, hence it is crucial to further study other attributes that contribute to the instability of the cathode material [28].

Rapulenyane et. al., synthesised the $Li_{1.2}Mn_{0.6}Ni_{0.2}O_2$ using a simple one-pot co-precipitation method with several concentrations of urea from 1.0 to 1.8 at pH 9.0, 9.5, 10.0 and 10.5. They found that the $Li_{1.2}Mn_{0.6}Ni_{0.2}O_2$ particles are agglomerated with a spherical shape and however, show less agglomeration and have higher surface area at pH 10.0. They also observed that the Mn and Ni metals are evenly distributed throughout the different pHs implying that the process used for synthesis is capable of producing homogenous Lithium manganese-rich transition metal cathode materials. Upon performing the electrochemical measurements of the synthesized $Li_{1.2}Mn_{0.6}Ni_{0.2}O_2$ at $20mAg^{-1}$ current density between 2.0V and 4.8V, they found that all the materials have

adequate stability at elevated potentials of 4.8V. Furthermore they show high discharge capacities at >4.5V at 20mAg^{-1}. For pH 10.0 the first charge and discharge capacities were 373mAhg^{-1} and 266mAhg^{-1} respectively suggesting that this material has coulombic efficiency of 71% which is higher than 65% of the materials at other pH values. However, all materials displayed capacity loss during the first dicharge cycle [29].

An additional method that has been proved to be suitable for improving the electrochemical performance of Li-rich cathode materials is surface fluorination. The introduction of fluorine into a Li-rich cathode material potentially improves the initial coulombic efficiency, discharge capacity and cycling stability of the material. Doping with the fluorine element partially replaces the lattice oxygen, forming F-Metal bonding and consequently reducing irreversible oxygen loss and improve the stability of the crystal structure during cycling [30]. Li et al., studied the $Li_{1.2-x}Mn_{0.54}Ni_{0.13}Co_{0.13}O_{2-x}F_x$ (x=0, 0.02, 0.05, 0.08) components to examine the impact of F doping on the material's structure, morphology, and electrochemical performance.

They discovered that doping with fluorine increases the unit cell volume and significantly improves the rate capability. Furthermore, they found that fluorine doping has a noticeable effect on impeding the unwanted phase transition from layered to spinel phase during charging and discharging, permitting the fluorine doped materials to produce a significant amount of reversible energy output [31]. Song et al. also investigated the effects of F doping on Li-rich Mn-based ($Li[Li_{0.16}Ni_{0.16}Co_{0.16}Mn_{0.5}]O_{2-x}F_x$) materials by first-principle calculations and analytical techniques and found that the addition of fluorine aided the reduction of manganese and cobalt which assisted in suppressing structural changes in the material [32]. In another work Guo et al., discovered that co-doping with cation and anion (Mg and F) improves cycling performance of Li-rich Mn-based materials as a result of the lattice structure stabilization brought by the F and Mg dopants and the lowering of Ni valence by the F-ions bonded during the charge compensation process [33].

The technique of co-doping with cation and anion is being investigated extensively as an approach to improve the electrochemical performance of Li and Mn-rich layered cathodes. Ngoc et al., explored the effects of co-doping the $Li_{1.2}Mn_{0.6}Ni_{0.2}O_2$ cathode material with F and Ti. They found that co-doping with Ti and F boosts the cycling performance and coulombic efficiency of the cathode material. They discovered that the

lattice parameters expand which improves the diffusion of Li^+. It was further found that the co-doped material exhibits a steady capacity of 180mAhg^{-1} with 93% capacity retention after 150 cycles. However, they found that the doped sample is spinel rich implying that the issue of layered to spinel phase transformation is not solved by doping the material with F and Ti [34]. This suggests that there is still a need to study the co-doping technique on these materials and study other elements along with different compositions.

In this work we explore the effects of doping the $Li_{1.2}Mn_{0.8}O_2$ material with F, with Ni, and co-doping it with F and Ni to test the influence of the presence of these elements in the material. The electrochemical performance and characteristics of LIB cathodes are greatly influenced by the synthesis methods, and the direct solid-state synthesis is one of the common methods used to synthesize cathodes for LIBs as it produces correct stoichiometries. However, it is costly due to the calcination step at high temperatures, and it is difficult to use for large quantities. Co-precipitation on the other hand, is simple to use and it is able to achieve homogenous atomic level mixing of the elements in the precursor. It also allows for calcination to occur at lower temperatures and shorter time. For these reasons, we employ the co-precipitation reaction synthesis method in achieving Li-rich Mn-based layered oxides.

1.3 Structures

Figure 1 below is a representation of the Li_2MnO_3 and $Li_{1.2}Mn_{0.8}O_2$ structures. Li_2MnO_3 is the bulk structure from which $Li_{1.2}Mn_{0.8}O_2$ was built. This Li_2MnO_3 is a potential cathode for LIBs because of its high specific capacity of 250mAh/g. However, it suffers from low-rate capacity, voltage fade, and oxygen evolution [35], hence a lot of research is being done on the material in a quest to enhance its stability and performance.

The Li_2MnO_3 structure is monoclinic with a space group of C2/m and lattice parameters a=4.985, b=8.616, c=5.066, α=90, β=109.59, and γ=90. Li_2MnO_3 has an O3-type structure with Li^+-ions occupying the inter-slab octahedral sites, and the Li^+ and Mn^{4+}-ions occupy the slab octahedral sites in a ratio of 1:2.

Herein, a 1x1x1 supercell of the Li_2MnO_3 structure is studied, namely $Li_7Mn_5O_{12}$ with a stoichiometry equivalent to $Li_{1.2}Mn_{0.8}O_2$. The structure $Li_{1.2}Mn_{0.8}O_2$ has a space group of P2 and lattice parameters a=5.066, b=8.874, c=5.059, α=90, β=108.179, and γ=90. This is an O2-type structure with Mn^{3+} and Li^+ ions occupying the slab octahedral sites with a ratio of 2:1 and 1 Mn^{3+} and Li^+ occupying the inter-slab octahedral sites.

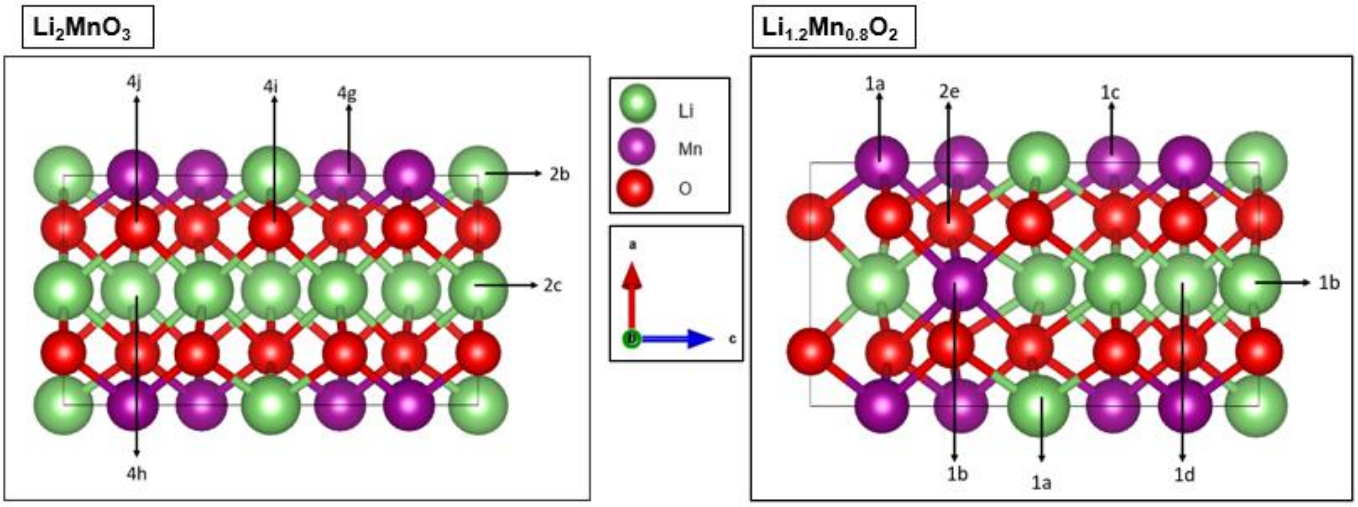

Figure 1: A representation of the crystal structures of bulk structure Li_2MnO_3 and the supercell $Li_{1.2}Mn_{0.8}O_2$ along with the site occupancy of atoms.

1.4 Background of Properties to be Investigated.

1.4.1 Heats of Formation

The amount of heat absorbed or evolved when one mole of a compound is produced from its chemical composition, with each material in its normal physical state is known as the heat of formation, often referred to as enthalpy of formation or standard enthalpy of formation. Heat of formation can also be defined as enthalpy of formation at 298.15K of a chemical process where a molecule is converted into a group of products that corresponds to a more stable form of its constituents' elements at room temperature [36]. Typically, the environments in which the compound is created are assumed to be 25 °C (77 °F) and 1 atmospheric pressure, in which case the heat of formation is called the standard heat of formation [37]. These are based on Hess's law, which states that the standard enthalpy of an overall reaction is the sum of the standard enthalpies of individual reactions via which the reaction can be diffused [38]. The heats of formation and related entropies provide a good basic comprehension of the compound's stability and the generation of phase diagrams. The heat of formation (ΔH_f) is approximated using the formula:

$$\Delta H_f = E_m - \sum_i N_i E_i \qquad (1.4.1\text{-}1)$$

Where the total molecular energy is E_m, E_i is the total energy of the element and N_i represents the number of atoms in the molecule.

1.4.2 Mechanical properties

Solid-state concepts such as equations of state, brittleness, ductility, anisotropy, elastic wave propagation, and normal mode oscillations are all related to the elastic properties of solids, which makes them extremely significant. The elastic constants control how a material reacts to pressure [39]. They gauge a material's relationship between strain and stress, given that the strain is not too large such that it violates Hook's law [40]. Elastic constants of a material define how the material reacts to applied strain or, conversely, how much stress is needed to keep a specific deformation. Three components of both tensile and shear make up the stress and strain respectively [41].

Young's modulus, shear modulus, bulk modulus, and Poisson's ratio are frequently used to describe a material's elastic properties. Just two of these elastic constants are distinct

for isotropic materials; the additional constants are computed using the relationships given by the theory of elasticity.

The bulk modulus is a measure of a material's resistance to contraction or compression. It is also described as a measure of the proportion of the rise in pressure to the relative decrease in volume of the material. It is thus a depiction of how resistant a material is to changing volume when compression is applied to it on all sides. The bulk modulus is often represented as pressure exerted to a relative shift in volume [42].

Shear modulus is a measure of a material's stiffness and its ability to withstand shear deformation. The ratio of shear stress to shear strain is known as the shear modulus [43].

Young's modulus is a measure of the material's resistance to elastic deformation, given by the proportion of stress to strain, it is essentially influenced by the strength of the chemical bonding in the solid state, and it is essential in predicting the behaviour of a material under stress and determining the residual stress in a material [44]. The elastic constant that is most well-known, however, is Young's modulus, which is a common application in engineering design [45].

1.4.3 Density of States

Due to its simplicity in describing complex electronic systems, the density of states (DOS) concept is arguably the most important concept for understanding the physical properties of materials. The DOS provides visually perceptible indicators that govern a material's electrical and optical properties, such as the band gap and effective masses of carriers [46].

The density of states represents the number of distinct states in system, that electrons can occupy at a given energy level. A material's properties, including its electrical conductivity, specific heat, and paramagnetic susceptibility are dependent on the DOS [47] [48]. The carriers' energy distributions and concentrations are described by DOS; therefore, one can comment on a material's property by analysing the DOS gap at Fermi level [49].

Density distributions are continuous as opposed to discrete like spectral density, in contrast to isolated systems like atoms or molecules in the gas phase. When the DOS is high at a certain energy level, it means that there are many states that are free to occupy. A density of states of zero means that there are no available states at that specific energy

level. In general, DOS represents an average of the system's space and time domains. Local variations, most of which are caused by distortions in the original system, are often known as local density of states (LDOS). When an undisturbed system shows a DOS of zero, the LDOS can still be nonzero in a specific region, which is caused by the existence of local potential [46].

The DOS for conduction and valence bands is determined by the states that are available for occupation and the probability of occupancy at a certain energy. As a result, the DOS can be used to determine the overall distribution of states as a function of energy, as well as the spacing between energy bands in semiconductors [50] [51].

1.5 Rationale

The pursuit for novel high energy cathode materials for Li-ion batteries has led to a discovery of various promising but complex materials such as the Li and Mn-rich layered oxides. These lithium manganese oxides are electroactive, and they act as host materials for intercalation in lithium cells. Li_2MnO_3 is one of the most intriguing materials in this group of oxides, and this is due to its structure and electrochemical activity along with its low cost, environmental friendliness, and non-toxicity [52].

Li_2MnO_3 can deliver a high theoretical capacity of 460mAh/g for total Li extraction, however, this material is electrochemically inactive in its microcrystalline form for the insertion and removal of lithium between 2.0 and 4.4V [53] which restricts its practical applications. The material also suffers from voltage fade, low coulombic efficiency and poor rate performance which contributes to the barrier in commercialization.

This has led to an increased research interest around the Li_2MnO_3 material wherein several techniques such as surface coating, doping, and modification of particle morphologies have been implemented to enhance the performance and stability of the material [54].

Recently, transition metal ion substitution has been implemented to enhance the electrochemical properties of the Li_2MnO_3 material. Kim et al., studied the $Li_{1.96}Ni_{0.056}Mn_{0.648}O_2$ ($Li_{1.944}Ni_{0.084}Mn_{0.972}O_3$) components which were prepared by Ni doping. They discovered that this material has a discharge capacity of $192mAhg^{-1}$ between 2.0 and 4.8V vs. Li/Li^+ at a current density of $0.2mAcm^{-2}$ [55]. In other studies, Tabuchi et al., showed that partially substituting Mn with Fe in Li_2MnO_3 gives a high initial discharge capacity with 78% of the capacity retained after 20 cycles [56]. They also investigated the effects of co-substituting the material with Ni and Fe and they found that the capacity retention is increased to 80% after 20 cycles between 2.0V and 4.8V [57]. Daisuke et al., [58] observed that substituting Mn with Ru shows a discharge capacity of $192mAhg^{-1}$ in the initial cycle and $169mAhg^{-1}$ after 10 cycles. However, these capacity retentions and cycling stability obtained by transition metal substitution are still not sufficient to meet the requirement of practical application for this material [59]. This implies that there is still a need to study substitution of other transition metals or study other compositions of the material.

Anion substitution for oxygen is among the strategies used to address the shortcomings in lithium manganese oxides. This is believed to improve the stability of these materials by suppressing the irreversible oxygen loss that occurs in the materials during charging and discharging. Song et al. investigated the effects of fluorine doping on Li-rich layered oxide in a quest to supress the irreversible capacity loss. They studied the electrochemical properties of a fluorine doped lithium manganese oxide with the composition $Li[Li_{1/6}Ni_{1/6}Co_{1/6}Mn_{1/2}]O_{2-x}F_x$ (x=0.00-0.07). They observed that the material exhibits an increased reversible capacity along with an enhanced cycling performance and rate capability. They further discovered that the addition of fluorine promoted the reduction of the transition metal ions and reduced oxygen loss [60]. However, fluorination of lithium manganese layered oxides is performed via high temperature solid state reactions which produce powders that have large irreversible capacity losses due to particle size growth caused by the added fluorine. Therefore, it is essential to explore other synthesis methods to achieve better materials.

1.6 Aim

The aim of this project is to study the stability of $Li_{1.2}Mn_{0.8}O_2$ cathode material and investigate the effects of fluorination and transition metal doping on the material.

1.7 Objectives

The objectives of this study are to:

i. study the structural, mechanical, and electronic properties of $Li_{1.2}Mn_{0.8}O_2$.
ii. fluorinate $Li_{1.2}Mn_{0.8}O_2$ and study the interaction of the oxygens with fluorine.
iii. investigate phase stability with cluster expansion.
iv. dope $Li_{1.2}Mn_{0.8}O_2$ with Ni and study the generated phases.
v. synthesise and characterize the $Li_{1.2}Mn_{0.8}O_2$ material experimentally.

1.8 Outline of the study

Chapter 1 discusses the general background of Li-ion batteries and their cathode materials. It reviews the literature of Lithium-rich manganese oxide cathode materials including reference to some of the work that has been done towards the development and enhancement of Lithium-rich manganese oxide cathodes. Furthermore, Chapter 1 includes the background of the properties studied and outlines the aims and objectives of the study.

Chapter 2 gives a background of the simulations and methods used in this study. It discusses the DFT, Vienna ab-initio Simulation Package (VASP), the approximation methods, the Universal Cluster Expansion (UNCLE) code and the experimental approach of the study. It further gives the theoretical background of experimental methods.

Chapter 3 is a discussion of results from First-principles calculations. This chapter gives a detailed discussion of the structural properties, mechanical properties, and electronic properties of all the structures studied in this project.

Chapter 4 details the cluster expansions performed in this study along with brief discussions of the results yielded from the cluster expansions.

Chapter 5 gives the results obtained in the experimental section of the project. It also gives details of the procedures followed in synthesizing and analysing the materials experimentally.

Chapter 6 gives a summary of the work and a conclusion of the findings.

Chapter 2

2.1 Density Functional Theory

Density Functional Theory (DFT) is a method in machine learning that's employed to investigate the electronic arrangement of extensive systems, mainly focusing on atoms, molecules, and substances in a condensed state. Its primary purpose is to derive comparative knowledge of material qualities from quantum mechanics' fundamental laws [61]. In 1964, Hohenberg and Kohn developed DFT, followed by Kohn and Sham in 1965 [62]. It has contributed to the emergence of independent-particle methods that incorporate the correlations and interactions of the particles [63]. Walter Kohn and Pierre Hohenberg first used this theory theoretically in the 1960s. In contrast to conventional electronic structure approaches, which sought approximate answers to the Schrodinger equation of multiple electrons interacting within an external electrostatic field, density functional theory relies solely on the one-body density as the primary variable [64]. The DFT is computationally viable even for massive systems since well the density is only a component of three dimensions of space instead of just the wave function's 3N coordinates. In DFT, the main components are the theorems of Hohenberg-Kohn and Kohn-Sham [64]. The focus of the binary ground state DFT is on a system of N functionally related electrons that is identified by the Hamiltonian in equation (1) below, according to these two theorems.

$$\widehat{H} = \hat{T} + \hat{V} + \widehat{V_{ee}} = -\sum_{i=1}^{N}\left(\frac{\nabla_i^2}{2}\right) + \sum_{i=1}^{N} v(r_i) + \frac{1}{2}\sum_{i=1}^{N} 1 \sum_{J=1}^{N} \frac{1}{|r_i - r_j|} \quad (2.1)$$

The fundamental proposition of density functional theory is summed up in the Hohenberg-Kohn theorem which can be summarized in three statements for non-degenerate ground states. 1. The ground state electron density, $n(r)$, in a system of interacting electrons uniquely dictates the external potential $v(r)$ governing the electrons' movement, subsequently determining the Hamiltonian and all physical attributes of the system. 2. The ground state energy and density of a system defined by its potential can be derived using a variational principle that solely concerns the density. This suggests that the ground state energy can be expressed as a functional of the density, providing the accurate ground state energy when the actual ground state density is applied. However, for any other densities the inequality listed in (2.2) holds.

$$E_0 = E_{v0}[n_0] < E_{v0}[n] \quad (2.2)$$

3. There exists a functional f(n) which permits the expression of the energy functional as:

$$E_{v0}[n] = F[n] + \int d^3 r v_0(r) n(r). \quad (2.3)$$

The functional f(n) is universal, meaning that it remains consistent regardless of the system's specific potential or particle-particle interaction. In other words, its functional form remains unchanged across all systems [64].

According to the Hohenberg-Kohn variational principle, the ground state density corresponding to the external potential can be derived by solving the Euler equation.

$$\frac{\delta E_v[n]}{\delta n(r)} = \frac{\delta F[n]}{\delta n(r)} + v(r) = 0 \quad (2.4)$$

Currently, the Euler equation is not commonly employed in electronic structure computations. Instead, the Hohenberg-Kohn theorem serves as the fundamental theoretical basis for creating an effective single-particle method to compute the ground-state density and energy of systems with interacting electrons. The accompanying equations, known as the Kohn–Sham equations, are central to modern density-functional theory. They take the form of a single-particle Schrodinger equation. The density can then be calculated using the N single-particle orbitals occupied by the slater determinant in its ground state [64].

Almost all DFT applications operate within the framework Kohn-Sham method, where a non-interacting electronic system is utilized to compute the density of an interacting system. This scheme results in the following equation with Hartree atomic units.

$$\left[-\frac{\nabla^2}{2} + v_{ext}(r) v_{Hartree}[n](r) + v_{xc}[n](r)\right] \varphi_i(r) = \varepsilon_i \varphi_i(r) \quad (2.5)$$

The initial term in the equation represents the electrons' kinetic energy; while the second term represents the external potential, typically induced by a collection of Coulombic point charges. The third component, the Hartree potential, characterizes the classical electrostatic repulsion among the electrons [65]. The exchange correlation energy, which describes all non-trivial many body effects, is the scheme's central quantity. The actual shape of this quantity is unknown, hence any practical use of DFT must estimate it. The shape of this variable determines the precision of any computation because it is the only genuine approximation in the DFT [65].

2.2 Approximation Methods

2.2.1 Local Density Approximation (LDA)

The Local Density Approximation is a feasible method for exchange energy correlation ($E_{XC}[\rho_0]$) which is given by:

$$E_{XC}^{LDA}[\rho_0] = \int \rho_0(r)\varepsilon_{XC}(r)dr \quad (2.6)$$

Where ε_{XC} is the exchange correlation energy per electron of gas (a system created by evenly distributed electrons travelling on a positive charge background, resulting in an electrically neutral system) whose electronic density is approximately ρ_0 at each position r.

The LDA can be understood like this: in a molecule or a solid, there is a clear electron density at every location. It is assumed that an electron at any given point experiences the collective effect of the surrounding electrons as if the density of those surrounding electrons were constant throughout the entire space, matching the density at the electron's specific location. The exchange-correlation energy of the entire molecule or solid is calculated by summing up the contributions from each volume element through integration. The LDA estimates the energy associated with the actual density by using the energy of a uniform density that is constant locally. The local spin density method has been utilized for numerous years to compute the electronic structure in the field of solid-state physics [66]. This approximation is expressed as:

$$E_{XC}^{LSD}[n_\uparrow, n_\downarrow] = \int d^3 r n(r)\varepsilon_{XC}^{unif}[n_\uparrow(r), n_\downarrow(r)], \quad (2.7)$$

where $\varepsilon_{Xc}^{unif}(n_\uparrow, n_\downarrow)$ is the exchange-correlation energy per particle of a uniform electron gas [67] [68]. "One method to surpass the limitations of the local density approximations involves expanding the exchange-correlation functional to include terms that incorporate gradients of the electron density. These gradients quantify alterations in the electron density and can be utilized to enhance the local density approximation. Local density approximations in DFT are a set of approximations to the exchange-correlation (E_{XC}) functional, which are based on the electronic density at every point in space. LDA suggests that the E_{XC} behaves similarly to that of a locally uniform electron gas when the charge density changes gradually in certain regions [69]. This is the most commonly employed approximation, where the exchange-correlation (E_{XC}) density of a non-uniform

system is replaced by that of an electron gas assessed at the local density. LDA relies on two fundamental assumptions: firstly, that the exchange and correlation effects primarily originate from the immediate vicinity of point r , and secondly, that these effects are somewhat insensitive to changes in the electron density in the vicinity of r [70]. When these two conditions are met, the contribution from the volume element dr is equivalent to what it would be if this volume element were encompassed by a constant electron density $p(r)$ identical to that within dr. In this approximation, the exchange-correlation energy density of the homogenous electron gas remains unchanged.

2.2.2 Generalized Gradient Approximation

Gradient-corrected density functionals as proposed by Perdew [71], Burke [72], Perdew and Wang [73] and Perdew, Burke and Ernzerhof [74] provide a solution to the limitations of the previously discussed LDA. The fundamental concept in these approaches involves incorporating terms in the exchange-correlation expressions that rely on the gradient of the electron density, rather than solely on its value at specific points in space. Hence, these corrections are occasionally termed “non-local” potentials. [75]

Although dissociation energies computed using these corrections approach the accuracy of the most advanced post-Hartree-Fock quantum chemistry methods, gradient corrected density functional calculations are significantly less computationally intensive and have broader applicability. Gradient corrected density functionals have been thoroughly investigated for molecular systems, such as by researchers like Andzelm and Wimmer [76]. The outcomes are highly promising, suggesting that this approach could prove immensely valuable in furnishing precise thermodynamical data. The one-particle eigenvalues derived from gradient-corrected exchange-correlation potentials show no substantial deviation from those obtained with the LDA. Hence, these potentials do not aim to eliminate the discrepancy between calculated and measured energy band gaps. Figure 2 presents a comparison between LDA and GGA with experimental data. Utilizing GGA has minimal impact on local characteristics, typically resulting in an overestimation of bond lengths and cell parameters. However, it generally leads to a notable enhancement in overall changes in total energy, particularly when two atoms combine to form a molecule. In this study, we employed the PBE version of the GGA, [77] which was developed to be more robust and precise compared to the original GGA formulation [78].

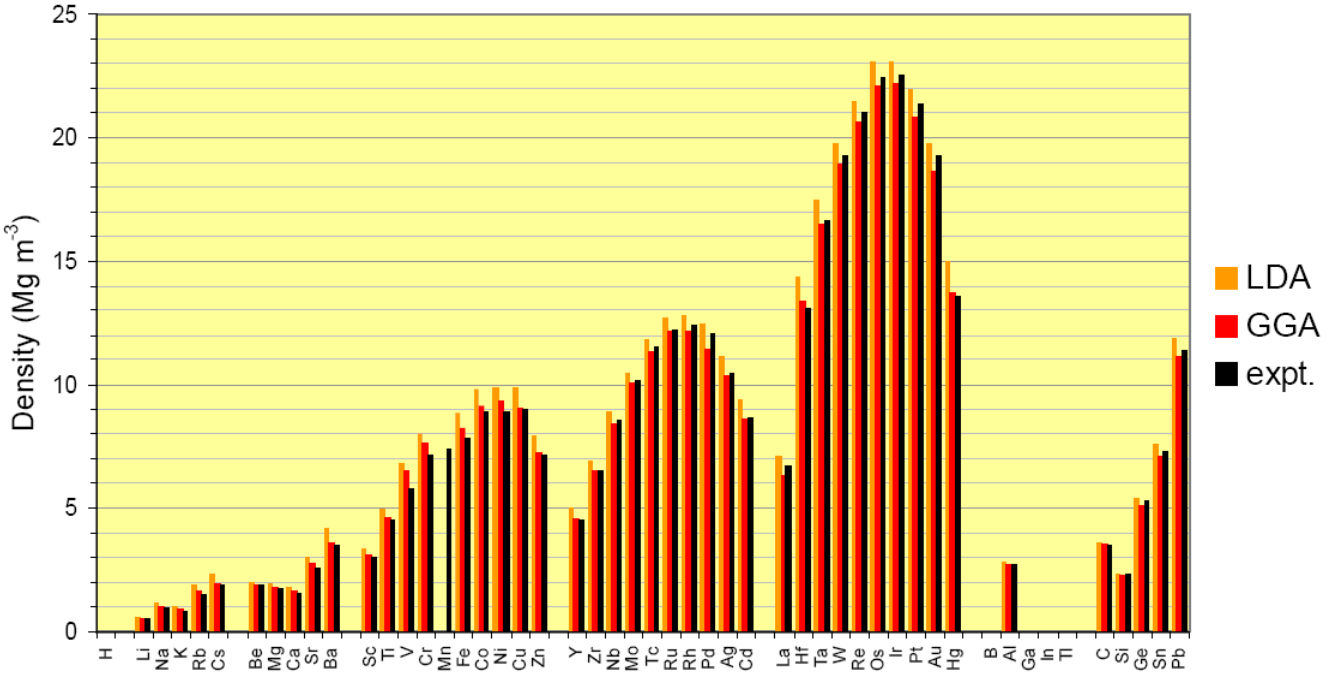

Figure 2: A comparison of the density of selected elements computed with the local density approximation, the generalized gradient approximation and the experimental findings.

2.3 K-Sampling

In the electronic structure, states are permitted only at specific k-points defined by the boundary conditions applicable to the solid's bulk. The density of permissible k-points increases with the solid's volume. To accommodate the infinite number of electrons in the solid, an infinite number of k-points are considered, yet only a finite number of electronic states are occupied at each k-point.

The Bloch theorem simplifies the task from computing an infinite number of electronic wave-functions to evaluating a finite number of *k*-points. The filled states at each k-point add to the electronic potential throughout the solid, meaning theoretically an infinite number of computations are required to determine this potential, nevertheless, the electronic wavefunctions at k-points that are extremely near each other are indistinguishable. Therefore, it is feasible to represent the electronic wavefunctions across a portion of k-space using the wavefunctions at a single k-point. Consequently,

only a finite number of k-points are necessary to compute the electronic potential and consequently determine the total energy of the solid.

Techniques have been developed to derive highly precise estimates of the electronic potential from a filled electronic band by computing the electronic wavefunctions at specific sets of k-points. The two prevalent methods are the approaches pioneered by Chadi and Cohen [79] and Monk-horst and Pack [80]. With these approaches, the electronic potential and the total energy of an insulator can be determined by assessing electronic states at a minimal number of k-points. However, to accurately delineate the Fermi surface and compute the electronic potential and total energy of a metallic system, a denser set of k-points is necessary.

Nevertheless, the expense in computational resources associated with densely sampling k-space escalates proportionally with the quantity of k-points within the Brillouin zone. Density functional codes simplify these k-space integrals by employing a finite set of k-points for sampling. To mitigate computational burden, specialized schemes for selecting k-points have emerged, aiming to achieve desired accuracy with the fewest possible k-points. The Monkhorst-Pack scheme stands out as the most widely utilized approach in this regard [81].

2.4 VASP Code

The Vienna Ab-initio Simulation Package (VASP) is a software suite designed for conducting ab-initio quantum mechanical molecular dynamics (MD) simulations, utilizing pseudopotentials and a basis set comprised of plane waves. VASP's methodology relies on a finite-temperature local-density approximation, where the variational quantity is the free energy, and it involves precise evaluation of the instantaneous electronic ground state at each molecular dynamics (MD) step. This is achieved through efficient matrix diagonalization techniques and Pulay mixing methods. These methods circumvent the issues associated with the original Car-Parrinello approach, which involves the simultaneous integration of electronic and ionic equations of motion. The interactions between ions and the electrons are characterised using ultrasoft Vanderbilt pseudopotentials (US-PP) or the projector augmented wave method (PAW) [82]. Both methods enable a significant decrease in the required number of plane waves per atom, particularly for transition metals and first-row elements. VASP facilitates the

straightforward calculation of forces and stresses, which can then be utilized to relax atoms into their instantaneous ground state.

In VASP, the implementation of the projector-augmented wave method reconstructs the complete all-electron density, eliminating the need for nonlinear core-corrections. VASP employs effective matrix diagonalization techniques and an efficient Pulay/Boyden charge density mixing. These methods sidestep the challenges associated with the original Car-Parrinello method, which involves the simultaneous integration of electronics and ionic equations of motion.

2.5 Cluster Expansion

Cluster Expansion is an approximation calculation approach that has been used to define the partition function represented as a power series expansion since Mayer suggested it in 1941. It is frequently used in computational materials science to pipeline calculation models (e.g., as a junction that integrates first principles calculation with Monte Carlo Simulation) with the goal of estimating material properties [83]. When combined with Monte Carlo simulations [84], the cluster expansion provides a solution to the restriction of standard DFT applications which accommodates a limited number of atoms [85].

The concept of cluster expansion represents the dependence of energy (or another observable) on configuration by expressing it as a sum of bonds. A specific configuration, denoting the type of atom at each site, is denoted by a vector σ, with each component corresponding to one site. The energy is dependent on the configuration $E(\sigma)$, and can be reduced formally [85] into a sum over bonds (not just pairs, but triplets, quadruplets, etc.) [86]. The bonds are referred to as clusters in the cluster expansion community and are denoted by F in equation 2.5-1 below. The idea is formally expressed as:

$$E(\sigma) = N \sum_F d_F J_F \prod F(\sigma) \qquad (2.5\text{-}1)$$

The factor d_F represents the count of degeneracies within the figure-class F normalised to the number of sites N in the configuration σ. Effective cluster interactions j and the pseudospin configurational variable σ_i for each lattice site i can be used to express the configurational energy E in a binary system as:

$$E = J_0 + J_1 \sum_i \sigma_i + \sum_{i>j} J_{ij}\sigma_i\sigma_j + \sum_{i>j>k} J_{ijk}\sigma_i\sigma_j\sigma_k + \cdots = \sum_\alpha J_\alpha \varphi_\alpha \qquad (2.5\text{-}2)$$

φ_α is the correlation function of a cluster α. The count of ordered structures for DFT calculations, N, is set to be equal to the number of effective cluster interactions, m, in a

simplified manner. As a result, all effective cluster interactions can be calculated analytically [87].

The choice of input structures impacts the effective clusters due to the atomic configurations from which they are derived. The database is increased systematically to avoid biasing the input database and therefore the effective cluster interactions. The ground state and other structures with enthalpies of formation around the convex hull are predicted by the first cluster expansion calculated from the set that was chosen initially. These predictions are then added to the input database using first principles calculations. This cycle is repeated, allowing the current cluster expansion to choose new structures for the database on its own [86].

2.5.1 Genetic Algorithm selection

To identify the best solution to a problem, genetic algorithms (Gas) apply the biological concept of “survival of the fittest”. These are helpful when dealing with highly correlated search spaces, other algorithms such as sequential optimization of individual parameters or Monte Carlo approaches based on individual, random parameter “flips” would wind up in local minima or even fail to converge at all. Figure 3 below is an illustration of the genetic algorithm. In general, the trial solutions in a GA are represented as binary sequencies of 0s and 1s, referred to as “genomes”.

The goal is to select a few many body-interaction types (MBIT) from a big pool to be included in a trial cluster expansion. A genome “…01110100011…” is a natural encoding of trial cluster expansion, with one gene for each possible MBIT in the pool and a one zero indication whether that figure is included. A set of genomes is monitored throughout many iterations, or “generations” during the GA.

“Child” genomes are formed by a cross-over “mating’” of two selected “parent” genomes from a previous iteration from one iteration to the next. Each gene in a child’s genome takes a value of the same gene in one of the parents. Only pre-existing “genetic” information could be spread in a mating step if this technique were carefully followed. As a result, if a particular MBIT or combination were removed from the whole population of trial cluster expansions in a single generation, that MBIT could never appear [88].

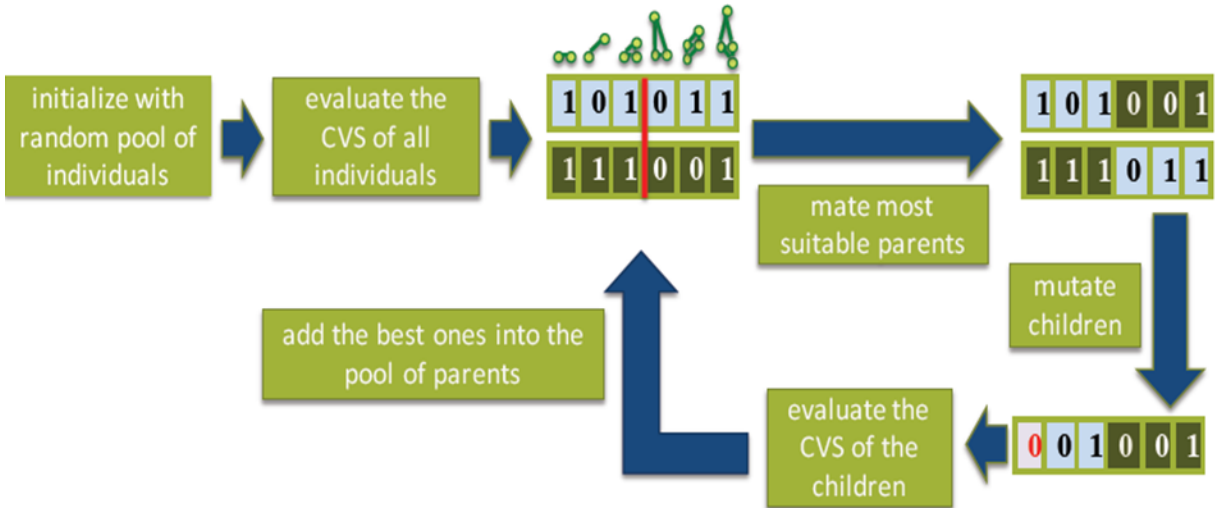

Figure 3: An illustration of the genetic algorithm approach used in cluster expansion.

2.6 Experimental methodology

2.6.1 Material synthesis of $Li_{1.2}Mn_{0.8}O_2$, $Li_{1.2}Mn_{0.6}Ni_{0.2}O_2$, and $Li_{1.2}Mn_{0.4}Ni_{0.2}Co_{0.2}O_2$.

2.6.1.1 Chemical reactor

A 4L chemical reactor was used for the synthesis of the precursor ($Ni_{0.25}Mn_{0.75}(CO_3)$) for the material $Li_{1.2}Mn_{0.6}Ni_{0.2}O_2$. The reactor consists of a tank with a stirrer, feeding tubes, thermal water jacket, and temperature and pH probes. This system is represented in figure 4 below.

$NiSO_4.6H_2O$ and $MnSO_4.H_2O$ were used as the metal sources. A 1L NH_4OH solution, 2L transition metal solutions of $NiSO_4.6H_2O$, and $MnSO_4.H_2O$ were prepared in deionized water. Na_2CO_3 solution was prepared with 2M Na_2CO_3 and deionized water to a volume of 2000ml and then used to control the pH. Each solution was transferred into a beaker through which they were fed into the reactor by the feeding tubes. The reaction was carried out under a N_2 atmosphere to prevent oxidation.

The pH was calibrated to 8 and the temperature set to 50˚C before the reaction started. Before feeding the solutions into the reactor, the reactor was filled with 0.05M $NH_3.H_2O$ (800ml). Mixing was continued for 24hrs with the temperature and pH recorded for each hour. At the completion of the reaction the product was filtered and dried in an oven for 24hrs at 100˚C. When dry, the product was ground with a pestle and mortar into a fine

powder. To lithiate the precursor, $LiCO_3$ was added to the precursor and heated at 900 ° C for 15hrs.

The same system was used to synthesize the precursor ($Ni_{0.25}Mn_{0.50}Co_{0.25}(CO_3)$) for $Li_{1.2}Ni_{0.2}Mn_{0.4}Co_{0.2}O_2$ to have a cobalt doped $Li_{1.2}Mn_{0.6}Ni_{0.2}O_2$. $NiSO_4.6H_2O$, $CoSO_4.7H_2O$, and $MnSO_4.H_2O$ all with 2mol/L concentrations were used as the metal sources with the solutions prepared in deionized water. Na_2CO_3 solution used for controlling pH was prepared with 2M Na_2CO_3 and deionized water to a volume of 2000ml. A solution of 0.05M $NH_3.H_2O$ (800ml) was prepared and used to fill 22.9% of the reactor before the start of the reaction process. The reactants were mixed in the reactor for 24hrs. The product was filtered and dried for 24hrs at 100°C at the completion of the reaction. $LiCO_3$ was added to the precursor and heated at 900°C to lithiate the precursor.

$MnCO_3$ was synthesized as a precursor for $Li_{1.2}Mn_{0.8}O_2$. A 2M solution of $MnSO_4.H_20$ was prepared with deionized water and used as the metal source for the reaction. 5M concentration of NH_4OH was prepared by mixing $8cm^3$ of NH_3 with deionized water, this solution was used to fill 22.9% (800ml) of the reactor before the start of the reaction. Na_2Co_3 solution was prepared by 2M of Na_2CO_3 with deionized water and used to control pH. The solutions were stirred for 24hrs with pH and temperature recorded for each hour. At the completion of the reaction the product was filtered and dried in an oven for 24hrs at 100°C. to lithiate the product $LiCO_3$ was added to the precursor and heated at 900°C.

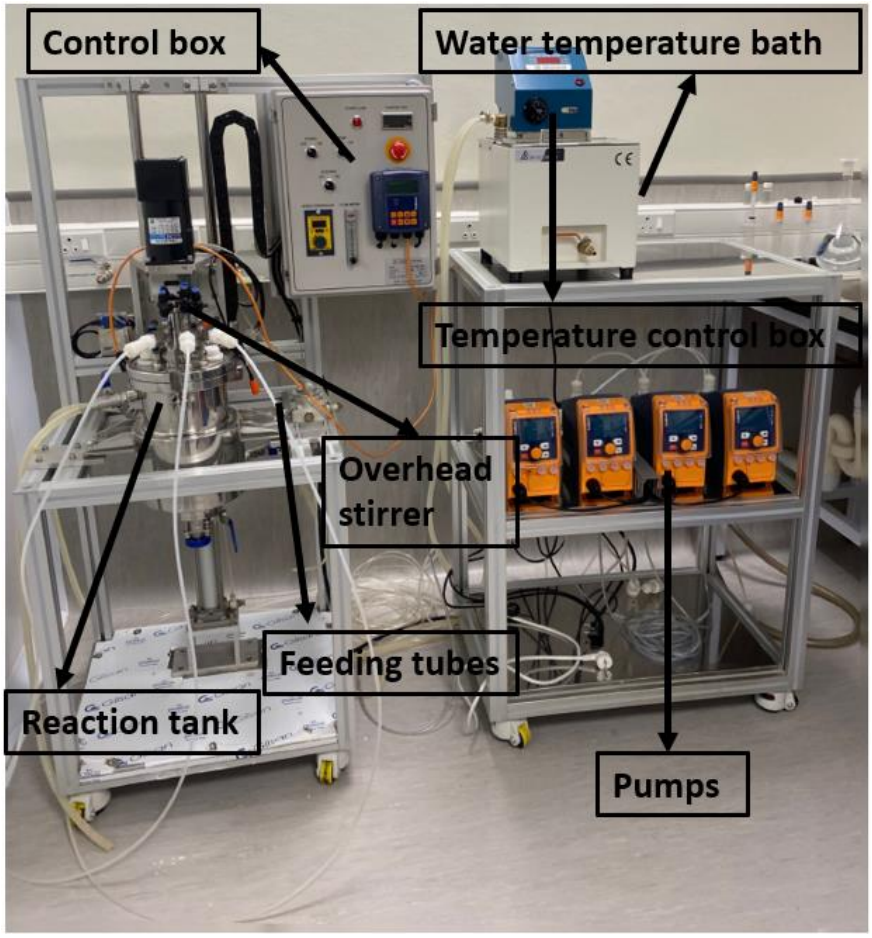

Figure 4: A representation of the 4L reactor system.

2.6.2 Materials characterization

2.6.2.1 X-ray powder diffraction (XRD)

X-ray powder diffraction method was used for phase structure characterisation. XRD is a method employed to identify and measure the quantities of crystalline phases [89]. XRD is a highly adaptable method that offers insights into the structural make-up of a material for phase analysis [90]. By fitting XRD patterns, it becomes possible to determine material lattice parameters, crystal orientation, and the presence of secondary phases within the sample. This method is a bulk characterisation technique that produces a representative diffraction pattern for the area being measured. XRD is a dependable technique that can be conducted under typical room temperature and pressure conditions [91]. Crystals and

polycrystalline materials possess crystal planes that allow for diffraction, forming the foundation of XRD. This technique relies on Bragg's equation principle,

$$n\lambda = 2dsin\theta \qquad (2.6.2.1\text{-}1)$$

described in terms of reflection of collimated X-ray beam incidence on a crystal plane of the sample of interest. This method relies on wide-angle elastic scattering and is typically applied to ordered materials, specifically long-range order crystalline material. A beam of X-rays passes through the sample and is deflected or diffracted by the atoms encountered along the X-ray's trajectory. This is graphically shown in figure 5 below. By applying Bragg's law and a well-placed detector the interference occurring due to scattering of X-rays can be observed and consequently help determine the material's crystalline structure characteristics [92].

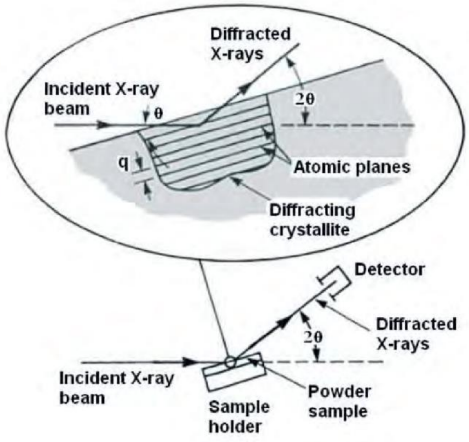

Figure 5: Schematic representation of X-ray diffraction.

2.6.2.2 Scanning electron microscope (SEM)

In this study, particle morphology characterisation is done with a scanning electron microscope. Scanning electron microscopy involves directing a focused beam of high-energy electrons onto the surface of a solid specimen, which generated various signals. These signals, resulting from interactions between electrons and the sample, provide details about the sample's morphology, chemical composition, and the crystalline structure and orientation of its constituent materials [93]. Electron microscopy is based on fundamental principles. When incident electrons decelerate in the sample, there are

electron-sample interactions that produce an array of signals (dissipated energy) which are a result of the accelerated electrons in an SEM which carry significant amounts of kinetic energy. This is depicted in figure 6 below. Examples of these signals are, secondary electrons that generate SEM images, backscattered electrons and diffracted backscattered electrons that provide information on the crystal structure and orientation of the materials, photons which give elemental analysis and continuum x-rays, visible light, and heat [93].

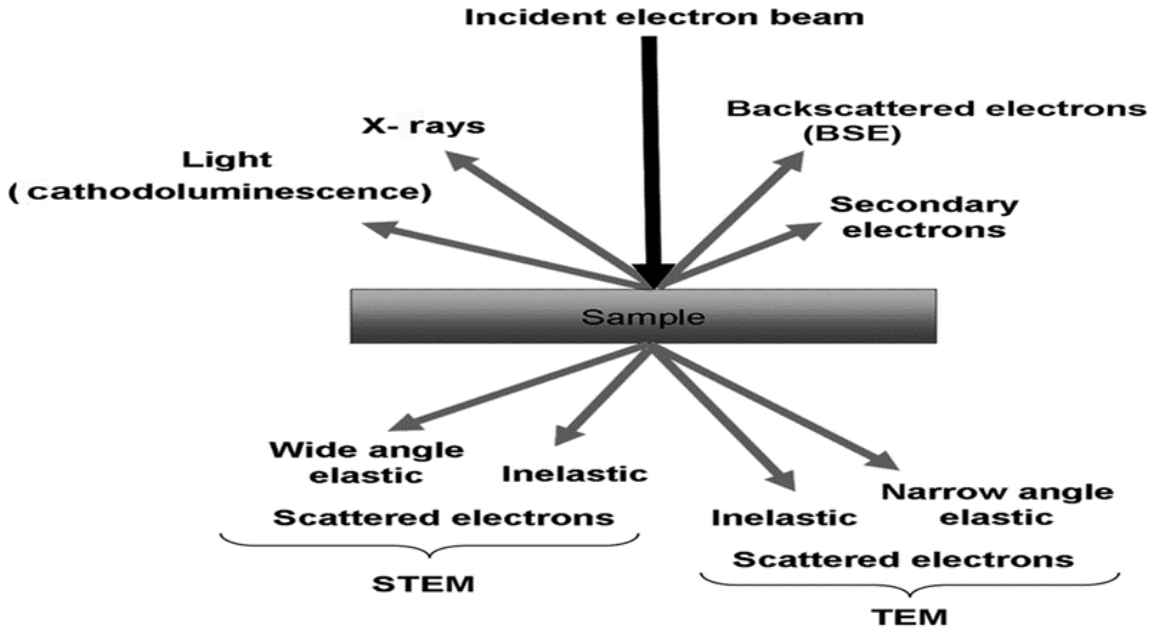

Figure 6: Schematic representation of a scanning electron microscopy.

Secondary electrons and backscattered electrons are widely used for visualizing or detecting samples. Secondary electrons are best for displaying shape (morphology) and topography on samples, while backscattered electrons are best for displaying compositional contrasts in multi-phase samples. SEM analysis is regarded as non-destructive since the generated x-rays by electron interactions do not result in loss of sample volume, as a result it is possible to analyse the same material repeatedly [94]. Figure 7 below is a representation of a typical SEM instrument with the electron column, sample chamber, EDS detector, electronic console, and visual display monitors.

Figure 7: Image of a Jeol, a typical SEM instrument *[93]*.

2.6.2.3 X-ray Fluorescence (XRF)

X-ray fluorescence analysis is a method employed for both quantitative and qualitative examination of elements, employing secondary X-rays generated by irradiating a sample with X-rays [95]. It is a precise and fast method to analyse the elemental composition of many samples non-destructively. When subjected to X-rays, the analyte's inner shell electrons become excited and emitted, leading to the formation of a vacancy in the inner shell. When outer shell electrons migrate to fill the vacancy in the inner shell, the energy difference between the electron energy levels of the element is discharged as an electromagnetic wave within the x-ray spectrum, known as a fluorescent x-ray. As the x-ray fluorescent spectrum originates directly from the element composition of the sample, qualitative analysis of the element present in the sample can be performed based on the spectrum. Moreover, as the intensity of the fluorescent x-rays correlates directly with the concentration of the element in the sample, quantitative analysis can be conducted using this intensity measurement [96].

2.6.2.4 Particle size analysis

Particle size analysis is essential for the characterisation of the size distributions of particles in each sample. A particle size distribution shows the percentage of particles of

a specific size. Particle size distribution affects a wide range of material qualities, including compressibility, reactivity, abrasiveness, solubility, and conveying behaviour for bulk materials. Based on the type of material and the extent of the analysis, a variety of techniques are employed for this. These consists of sieve analysis, dynamic image analysis, dynamic light scattering, and laser diffraction. In most cases, bulk materials, emulsions, suspensions, and in rare instances, aerosols are analysed.

Particle size measurement approaches can be logically divided into two main classes: field scanning and stream scanning. When determining particle size by stream scanning, a single particle is observed as a function of time, on the other hand, field scanning involves scanning a collection of particles [97]. Both classes are particularly useful for online particle size analysis in industrial settings. A probe is put directly into a process line during an experiment, the entire process flow should ideally be evaluated, however, process streams frequently operate at high particle flow rates [94].

Particle size measurements can be carried out in wet or dry methods. Wet method is the most popular method of sample dispersion for laser diffraction particle size measurement, which is particularly suitable for samples containing fine particles smaller than a few microns in size. This is because surface wetness significantly reduces particle to particle bonding forces, allowing agglomerated particles to be scattered with relatively low energy input [98].

In this study we use the laser diffraction particle analyser depicted in figure 8 below. Particle size analysers based on laser diffraction are used to determine the size of particles in a material. The angle of light scattered by particles as they pass through a laser beam is measured and used to determine the particle size. A laser diffraction particle size analyser employs several light detectors, with additional detector elements increasing sensitivity and limiting particle size. The time required to measure particle sizes differ depending on the instrument and can vary from 2 seconds to 10 minutes for each sample. A laser particle size analyser’s light source also influences particle size detecting limits; shorter wavelength violet and UV lasers are more appropriate to measuring submicron-sized particles than red lasers.

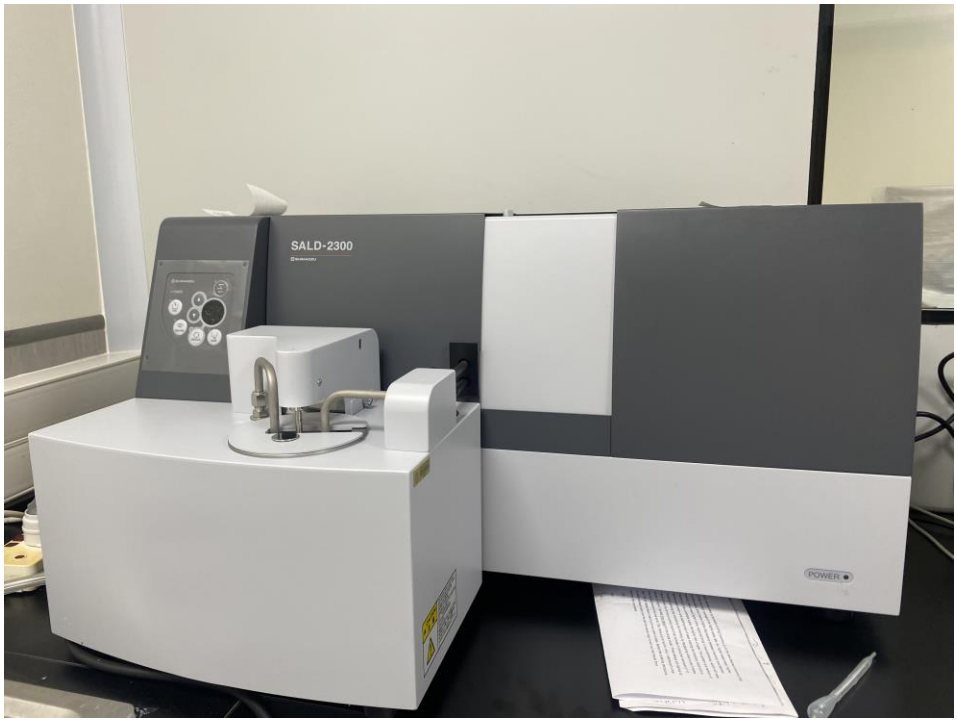

Figure 8: Laser diffraction particle size analyser.

Chapter 3

Structural, Mechanical, and Electronic Properties of $Li_{1.2}Mn_{0.8}O_2$ and Li_2MnO_3.

The structural, mechanical, and electronic properties of the two materials, Li_2MnO_3 and $Li_{1.2}Mn_{0.8}O_2$ are studied in depth in this section. The stabilities of the two materials are studied to infer whether the Li-rich 1x1x1 supercell $Li_{1.2}Mn_{0.8}O_2$ is more stable than the layered Li_2MnO_3.

3.1 Cut-off energy and K-points convergence

3.1.1 Cut-off energy

To find the convergence point of the cut-off energy for the Li_2MnO_3 and $Li_{1.2}Mn_{0.8}O_2$ structures, plane wave cut-off energy was varied from (100-900) eV at an interval of 100 eV for both structures, with default k-point mesh parameters in the Perdew-Burke-Ernzerhof Generalized Gradient Approximation (GGA-PBE) and carefully tested for convergence. Table 1 below shows the total energies corresponding to the cut-off energy for Li_2MnO_3 and $Li_{1.2}Mn_{0.8}O_2$, these energies are further represented in figure 9 and figure 10 respectively. The total energies of both structures decrease with increasing cut-off energies to a point where the change in total energy is minimal.

Table 1: Cut-off energies and corresponding total energies for the Li_2MnO_3 and $Li_{1.2}Mn_{0.8}O_2$ structures.

Cut-off energy (eV)	Total energy (eV)	
	Li_2MnO_3	$Li_{1.2}Mn_{0.8}O_2$
100	53.352	331.726
200	-45.538	-187.033
300	-38.113	-162.872
400	-36.840	-158.151
500	-36.707	-157.654
600	-36.714	-157.681
700	-36.723	-157.713
800	-36.726	-157.725
900	-36.726	-157.726

Figures 9 and 10 below are a representation of the energy values tabulated in table 1. The total energy versus cut-off energy graphs decrease exponentially up to the cut-off energy of 500eV. From this point onwards, the change in total energy is minimal so much that the graphs become linear. As a result, the energy at this point of convergence was selected and employed throughout the study.

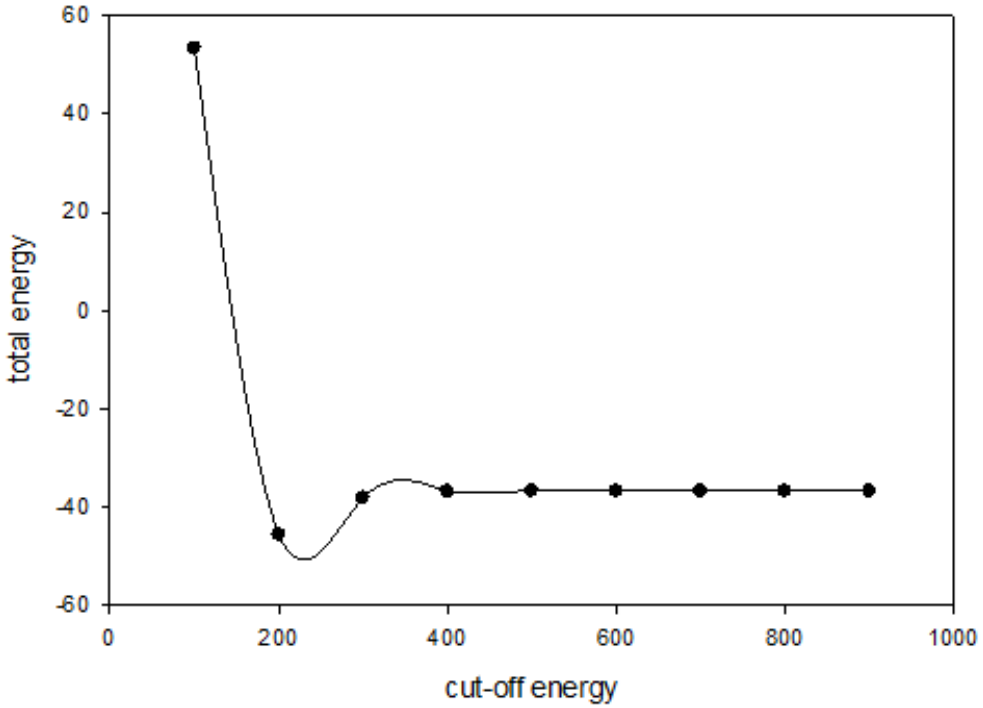

Figure 9: Graphical representation of the total energy versus cut-off energy for Li_2MnO_3 structure.

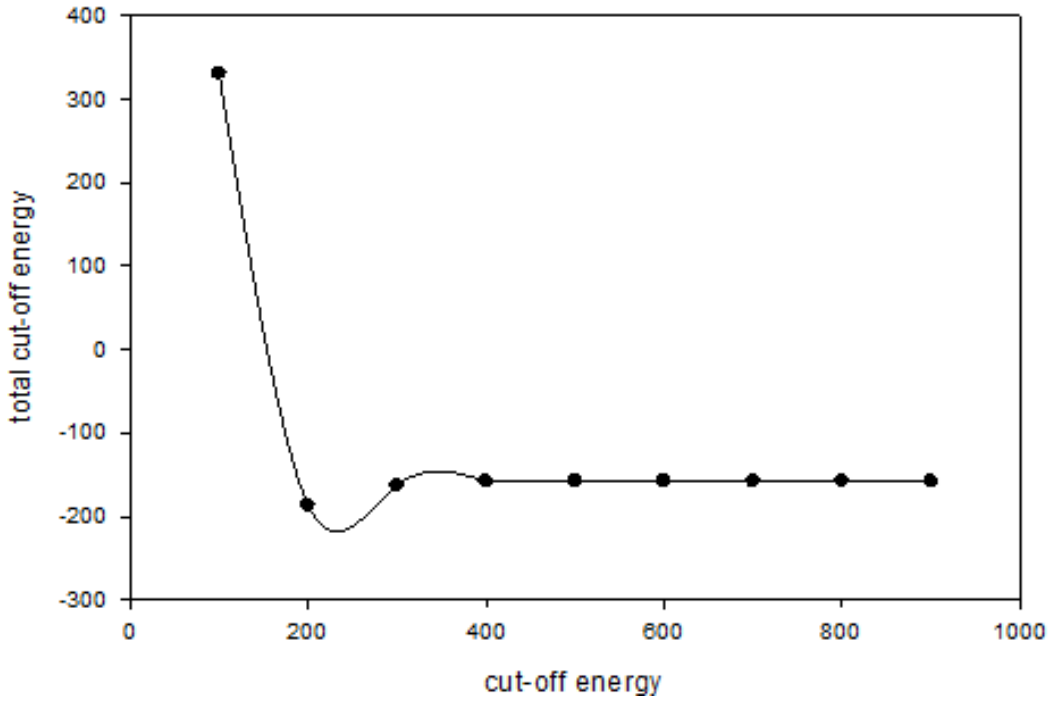

Figure 10: Graphical representation of the total energy against cut-off energy for the 1x1x1 supercell $Li_{1.2}Mn_{0.8}O_2$.

3.1.2 K-points

Table 2 below shows the total energies correlating to various k-point mesh parameters for Li_2MnO_3 and $Li_{1.2}Mn_{0.8}O_2$. The total energy calculations were carried out at a fixed cut-off energy of 500eV for both structures while the k-point mesh was varied from 1x1x1 to 9x9x9. The systems are considered converged when the change in total energy is minimal. For the Li_2MnO_3 structure, the convergence point was found to be at 5x5x5 and for the $Li_{1.2}Mn_{0.8}O_2$ structure it was found at k-points of 4x4x4.

Table 2: K-points and corresponding total energies for the bulk structure Li_2MnO_3 and the supercell $Li_{1.2}Mn_{0.8}O_2$.

K-points	Total energy (eV)	
	Li_2MnO_3	$Li_{1.2}Mn_{0.8}O_2$
1x1x1	-37.6567	-157.034
2x2x2	-38.0782	-158.175
3x3x3	-38.1200	-158.146
4x4x4	-38.1095	-158.141
5x5x5	-38.1124	-158.142
6x6x6	-38.1200	-158.144
7x7x7	-38.1133	-158.147
8x8x8	-38.1102	-158.150
9x9x9	-38.1120	-158.152

Figures 11 and 12 below are plots of the total energy against k-points for Li_2MnO_3 and $Li_{1.2}Mn_{0.8}O_2$ respectively. The graphs decrease exponentially until a point where the change is small, and the graphs become linear. For the Li_2MnO_3, the point where the graph shows minimal change is at 5x5x5, and for $Li_{1.2}Mn_{0.8}O_2$ it is at 4x4x4 which provides confirmation for the data in table 2. Since these k-points 5x5x5 and 4x4x4 were found to be enough to converge the system, they were selected and used throughout the study for property calculations of Li_2MnO_3 and $Li_{1.2}Mn_{0.8}O_2$ respectively.

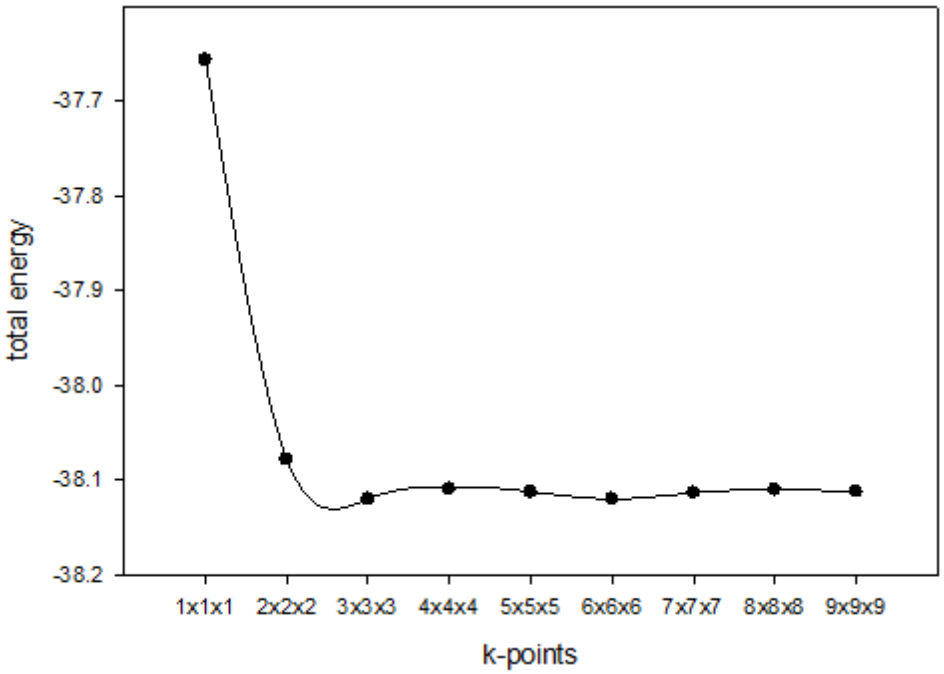

Figure 11: Graphical representation of the total energy versus k-points for Li_2MnO_3.

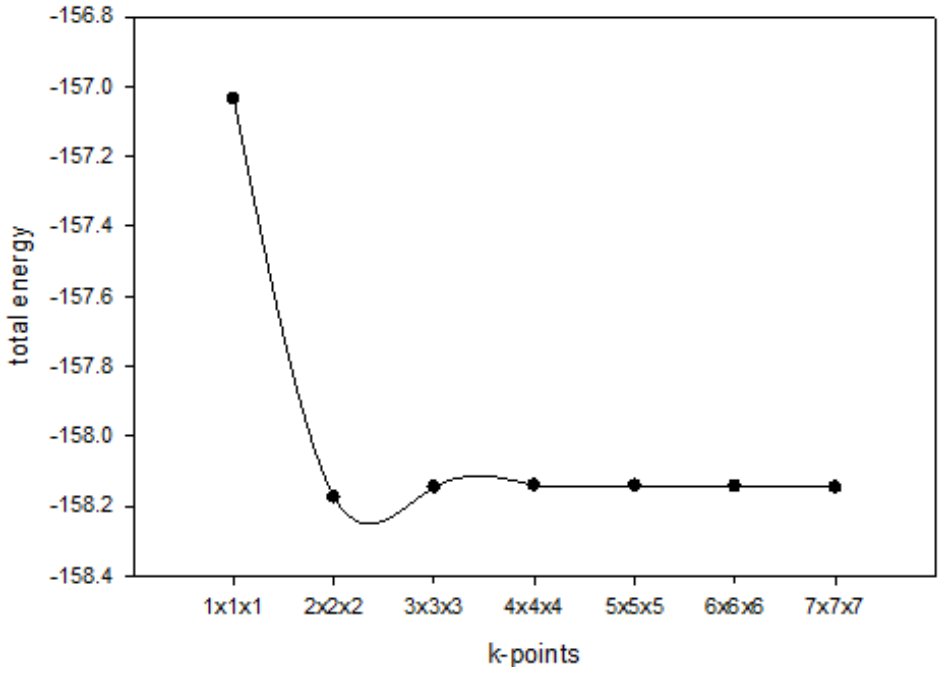

Figure 12: Graphical representation of the total energy versus k-points for $Li_{1.2}Mn_{0.8}O_2$.

3.2 Lattice Parameters and Heats of Formation

A common process in chemistry is the geometric optimization of crystal formations, which modifies the geometrical arrangement of particles inside a structure. Prior to doing any computations, structural optimization calculations were carried out to thoroughly relax the structures and determine their lattice parameters. The cut-off energy and k-points at the sites of convergence listed in section 3.1 above were adequate to perform these optimizations. The lattice parameters that were obtained after full geometry optimization of the two structures Li_2MnO_3 and $Li_{1.2}Mn_{0.8}O_2$ are tabulated in Table 3 below. The calculated lattice parameters a, b, and c for Li_2MnO_3 are in good agreement with experimental values as shown in table 3 below. To the best of our knowledge, there is currently no published lattice parameters of the $Li_{1.2}Mn_{0.8}O_2$ structure to compare with.

The heats of formation are essential in verifying the thermal stability of a material and a negative value indicates good stability [99]. Li_2MnO_3 and $Li_{1.2}Mn_{0.8}O_2$ have negative heats of formation, with the latter having the highest negative value which suggests that $Li_{1.2}Mn_{0.8}O_2$ is thermodynamically more stable than Li_2MnO_3. The increase in volume from Li_2MnO_3 to $Li_{1.2}Mn_{0.8}O_2$ is an indication of the increased number of the Li and Mn atoms.

Table 3: Calculated lattice parameters and a comparison with experimental results for the Li_2MnO_3, heats of formation, and cell volume of the Li_2MnO_3 and $Li_{1.2}Mn_{0.8}O_2$ structures.

Structure	Lattice Parameters			Heats of Formation (kJ/mol)	Volume (Å^3)
Li_2MnO_3	VASP a=4.895 b=8.616 c=5.062	EXP [100] a=4.937 b=8.532 c=5.03	α= 90° β=109.590° γ= 90°	-1283.73	204.97
$Li_{1.2}Mn_{0.8}O_2$	a=5.066 b=8.874 c=5.059		α=90° β=108.179° γ=90°	-4090.78	216.11

3.3 Mechanical Properties

By establishing different strain values of 0.001, 0.005, and 0.025, the elastic constants of Li_2MnO_3 and $Li_{1.2}Mn_{0.8}O_2$ were determined to assess the mechanical stability of the structures. Elastic properties are essential in determining the strength and hardness of material since the elastic constants show how the material responds to interatomic forces, and phase transitions [101]. Studying the elastic constants that typically indicate mechanical stability is crucial since the mechanical stability of the cathode material has influence on the electrochemical characteristics of the LIBs [102]. The stability criteria for monoclinic crystals are given by the following equations [103].

$$C_{11} > 0, C_{22} > 0, C_{33} > 0, C_{44} > 0, C_{55} > 0, C_{66} > 0 \quad (3.3\text{-}1)$$

$$(C_{44}C_{66} - C_{46}^2) > 0 \quad (3.3\text{-}2)$$

$$(C_{35}C_{55} - C_{35}^2) > 0 \quad (3.3\text{-}3)$$

$$(C_{22} + C_{33} - 2C_{23}) > 0 \quad (3.3\text{-}4)$$

$$[C_{11} + C_{22} + C_{33} + 2(C_{12} + C_{13} + C_{23})] > 0 \quad (3.3\text{-}5)$$

$$[C_{22}(C_{33}C_{55} - C_{35}^2) + 2C_{23}C_{25}C_{35} - C_{23}^2C_{55} - C_{25}^2C_{33}] > 0 \quad (3.3\text{-}6)$$

Table 4 below shows the calculated elastic constants for Li_2MnO_3 and $Li_{1.2}Mn_{0.8}O_2$. The results show that Li_2MnO_3 meets the stability criteria where the following strains: 0.001, 0.005, and 0.025 were used. The elastic constants C_{11}, C_{22}, C_{33}, C_{44}, C_{55}, and C_{66} values are positive implying that Li_2MnO_3's stability is not affected when the material is subjected to the strains above. On the other hand, $Li_{1.2}Mn_{0.8}O_2$ only satisfy the mechanical stability criterion under strain 0.001 and 0.025 but not 0.005. Under strain 0.005, both C_{22} and C_{66} become negative, indicating mechanical instability.

Considering the values of the elastic constants across all three strains, conditions for equations 3.3-1 to 3.3-6 are met for the Li_2MnO_3 structure, and this means that it is more mechanically stable than the $Li_{1.2}Mn_{0.8}O_2$ structure which does not meet the stability criteria under strain 0.005. The observed trend in the elastic constants with strain is a decrease with increasing strain and this observation suggests that the structures are likely to be mechanically unstable at higher strains and mechanically stable under low strains.

Table 4: A comparison of the elastic constants of the Li_2MnO_3 and $Li_{1.2}Mn_{0.8}O_2$ structures calculated under 3 different strains.

Elastic Constant	Strain 0.001		Strain 0.005		Strain 0.025	
	Li_2MnO_3	$Li_{1.2}Mn_{0.8}O_2$	Li_2MnO_3	$Li_{1.2}Mn_{0.8}O_2$	Li_2MnO_3	$Li_{1.2}Mn_{0.8}O_2$
C_{11}	326.64	277.58	273.57	261.82	278.73	241.84
C_{12}	81.52	81.87	63.69	57.07	65.10	80.32
C_{13}	82.23	85.11	34.22	82.93	35.88	79.73
C_{15}	-11.63	6.26	8.43	-2.15	7.37	-1.50
C_{22}	329.84	246.05	277.31	-227.31	281.26	131.08
C_{23}	85.88	89.46	37.48	97.66	38.55	84.70
C_{25}	17.28	30.23	-3.81	-5.40	-0.81	4.58
C_{33}	293.69	257.89	215.04	244.27	214.92	233.62
C_{35}	2.98	18.49	1.33	0.97	2.47	-1.85
C_{44}	121.99	78.51	78.93	130.65	78.78	75.38
C_{46}	14.73	11.27	-3.95	39.52	5.19	-3.52
C_{55}	122.15	96.45	80.49	85.16	80.50	71.36
C_{66}	123.49	84.79	107.65	-79.40	123.49	49.63

To further study the elastic stability of the materials, elastic moduli were calculated under the strains 0.001, 0.005, and 0.025 and shown in table 5 below. Elastic moduli are significant in evaluating a material's resistance to elastic deformation [104]. From the calculated moduli shown in table 5, Li_2MnO_3 has higher bulk modulus values than $Li_{1.2}Mn_{0.8}O_2$ for strains 0.001 and 0.005. Since the bulk modulus measure how resistant a material is to compression [101], this implies that Li_2MnO_3 has higher compressive strength than $Li_{1.2}Mn_{0.8}O_2$ because it has high bulk modulus values. Regarding the shear modulus, $Li_{1.2}Mn_{0.8}O_2$ continues to exhibit values lower than those of Li_2MnO_3 under all three strains, suggesting that Li_2MnO_3 is stiffer than $Li_{1.2}Mn_{0.8}O_2$ since the shear modulus measures the stiffness of the material. Furthermore, the Young's modulus values show that Li_2MnO_3 is more resistant to elastic deformation under strain as compared to $Li_{1.2}Mn_{0.8}O_2$. These findings collectively indicate that Li_2MnO_3 is more mechanically stable than $Li_{1.2}Mn_{0.8}O_2$.

Table 5: Calculated Bulk, Shear, Young's modulus, and Pugh's ratio of Li_2MnO_3 and $Li_{1.2}Mn_{0.8}O_2$ under strains 0.001, 0.005, and 0.025.

Strain 0.001					
Structure	Bulk (GPa)	Shear (GPa)	Young's (GPa)	Pugh's ratio B/G	Ductility
Li_2MnO_3	161.05	120.23	288.81	1.34	Brittle
$Li_{1.2}Mn_{0.8}O_2$	143.82	86.96	217.11	1.65	Brittle
Strain 0.005					
Li_2MnO_3	115.19	95.45	224.37	1.21	Brittle
$Li_{1.2}Mn_{0.8}O_2$	83.79	30.03	80.46	2.79	Ductile
Strain 0.025					
Li_2MnO_3	117.11	98.91	231.55	1.18	Brittle
$Li_{1.2}Mn_{0.8}O_2$	121.78	63.39	162.06	1.92	Ductile

3.4 Density of states

Figures 13 and 14 below represent the total and partial density of states of $Li_{1.2}Mn_{0.8}O_2$ and Li_2MnO_3 respectively. The electronic structure of a material determines its electrical conduction properties, and by analysing the density of states of the electron we can deduce whether the material is an insulator, semiconductor or a conductor [105].

The total density of states (TDOS) of $Li_{1.2}Mn_{0.8}O_2$ shows a band gap of 0.269eV at Fermi level, represented by a straight line at 0 energy and the Fermi level falls into the band gap. This presence of a band gap at the Fermi level indicates that the system is a semiconductor. The partial density of states (PDOS) of the Li atom shows that Li has minimum contribution to the TDOS of the bulk structure. The PDOS of the manganese atom indicates a significant contribution of manganese d-states to the TDOS around the energy range of 0-4eV. These manganese d-states are also visible in the valence band region from -7eV to -5eV, they further show contribution at the Fermi level where the shape of the Mn PDOS resembles that of the bulk structure's TDOS. With the manganese atom there is minimum contribution by the Mn p-states and little to no contribution by the Mn s-states to the TDOS of the bulk material. The oxygen atom also has a high

contribution to the TDOS of the structure. The O p-states contribute more to the TDOS at -7eV to -1eV and to the conduction band between 0eV and 4eV but at this region the contribution of the O p-states is less compared to that of the Mn d-states.

The total density of states of Li_2MnO_3 shows an indirect band gap of 1.888 eV. Like $Li_{1.2}Mn_{0.8}O_2$, the presence of a band gap implies that the system is a magnetic semiconductor, however, the gap of Li_2MnO_3 is considerably larger than that of $Li_{1.2}Mn_{0.8}O_2$ meaning that the latter is more favourable to electrical conduction. In Li_2MnO_3, the Manganese atom shows greater contribution to the TDOS of the material with the Mn d-states being dominant throughout the shape of the density of states. The Mn d-states have high contribution between 2eV to 4eV and -6eV to -4eV. The Li atom has little contribution to the TDOS, and the Li p and d states are the ones that are slightly visible on the PDOS than the s states. However, the shape of the PDOS of the Li atom is different from that of the TDOS of the structure, hence the contribution of the Li atom to the TDOS of the bulk structure is very little. The O atom also contributes to the TDOS, where it shows significant contribution between -2eV and 0eV. Its p-states contribute more around the Fermi level were the shape of the O p states close to the Fermi level is much like that of the TDOS compared to the states of the other atoms. These densities of states result for both Li_2MnO_3 and $Li_{1.2}Mn_{0.8}O_2$ suggest that the manganese atom in these materials is a determining factor in the conducting properties of these materials.

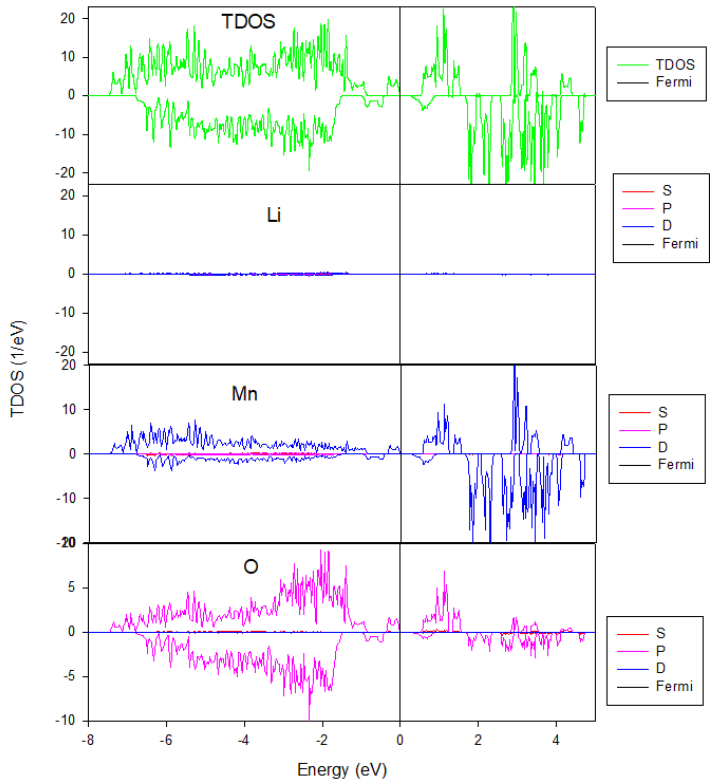

Figure 13: Density of states of the supercell $Li_{1.2}Mn_{0.8}O_2$ showing both the total density of states and the partial density of states of the Li, Mn, and O atoms along with the contributions of their s, p, and d orbitals..

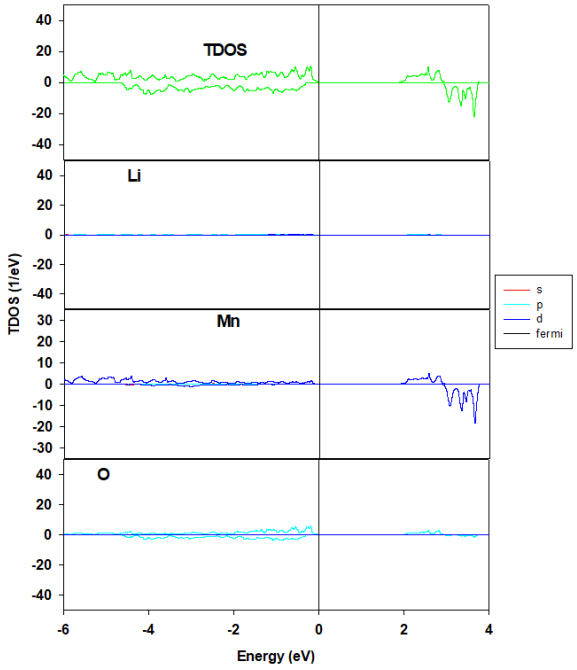

Figure 14: Total density of states of Li_2MnO_3 and the partial density of states of the Li, Mn, and O atoms and their s, p, and d orbitals.

3.5 Band structure

To further study the electronic behaviour of the structures Li_2MnO_3 and $Li_{1.2}Mn_{0.8}O_2$, we have calculated the band structures. A material's band structure can be used to identify if it is an insulator, conductor, or semiconductor by showing the energy levels of the material. It can also be used to find the valence and conduction bands, as well as direct or indirect band gaps in the material [106]. The band structure of $Li_{1.2}Mn_{0.8}O_2$ as represented in figure 15 below consists of the x-axis which is the Brillouin zone, and the y-axis which is the energy. The zero line represents the Fermi level and at this level it is observed that the valence band does not overlap into the conduction band which results in a band gap at the Fermi level. The band gap is 0.263eV and the presence of this band gap implies that the material is a semiconductor. Furthermore, this result confirms what was predicted by the density of states in section 3.4 above.

Figure 16 below represents the band structure of Li_2MnO_3. Just like in $Li_{1.2}Mn_{0.8}O_2$, the x-axis represents the Brillouin zone, and the y-axis represent the energy. Similarly, it is also observed with the Li_2MnO_3 that there is no overlap of the valence band into the conduction band resulting in a band gap. The value of the band gap in the band structure is 1.964eV, which also supports the density of states which showed a band gap of 1.888eV. With a large band gap, fewer electrons are present in the gap and electrical conductivity is less. With this, $Li_{1.2}Mn_{0.8}O_2$ is better in electric conduction compared to Li_2MnO_3 and this confirms the predictions made by the density of states.

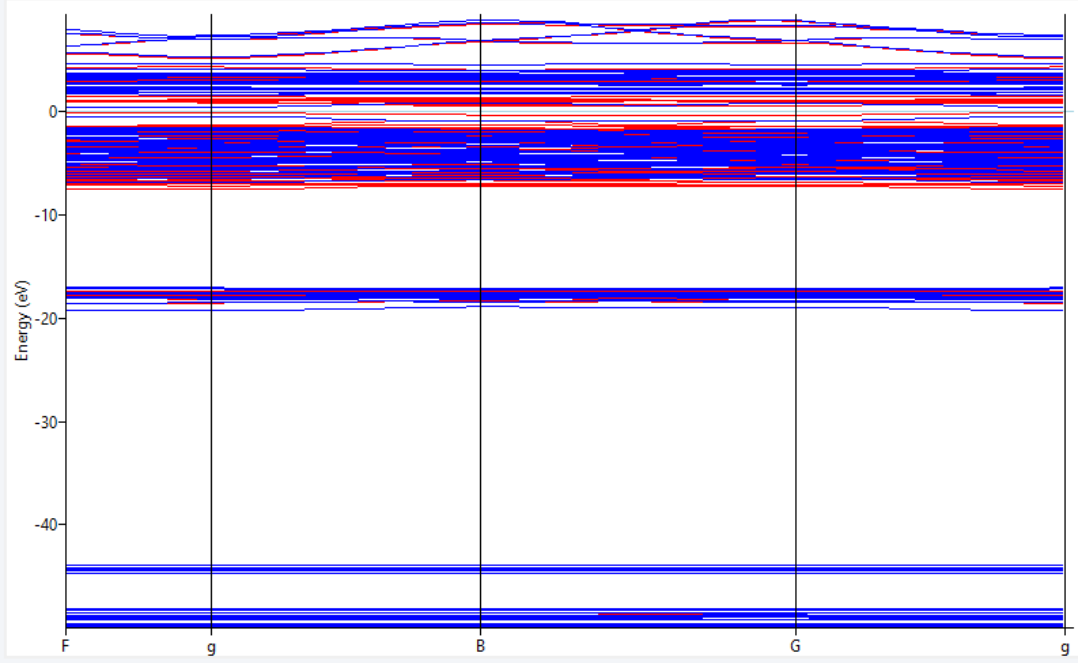

Figure 15: Band structure of $Li_{1.2}Mn_{0.8}O_2$ showing an overlap of electrons from the valence band to the conduction band at the Fermi level (zero line).

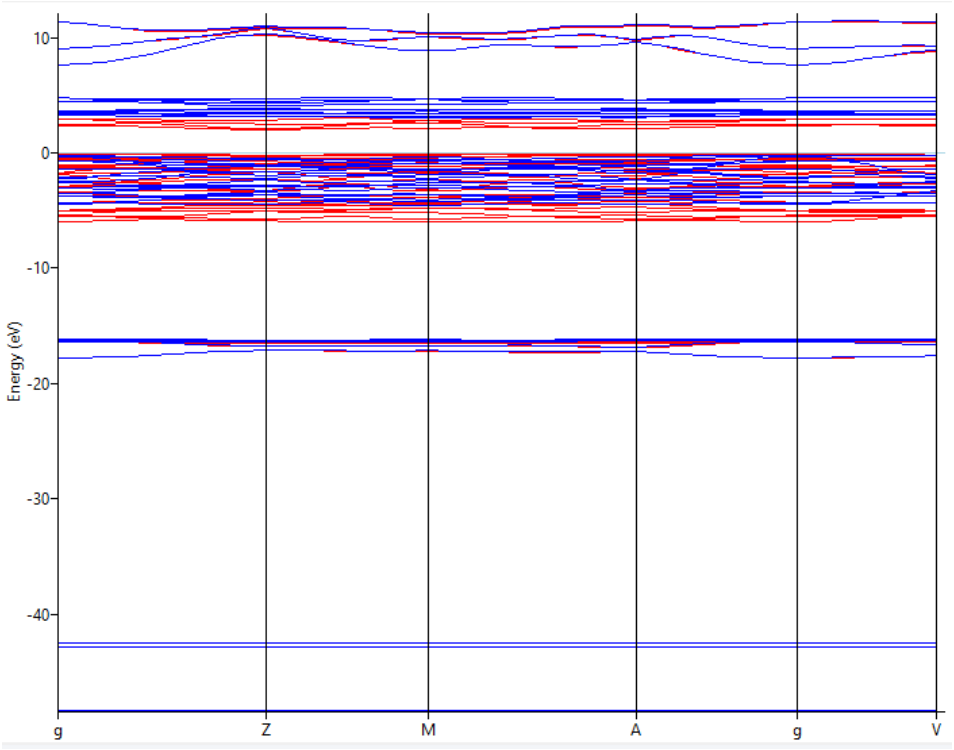

Figure 16: Band structure of Li_2MnO_3 showing a band gap at the Fermi level (zero line).

Structural, Mechanical, and Electronic Properties of $Li_{1.2}Mn_{0.6}Ni_{0.2}O_2$.

3.6 Lattice Parameters and Heats of Formation.

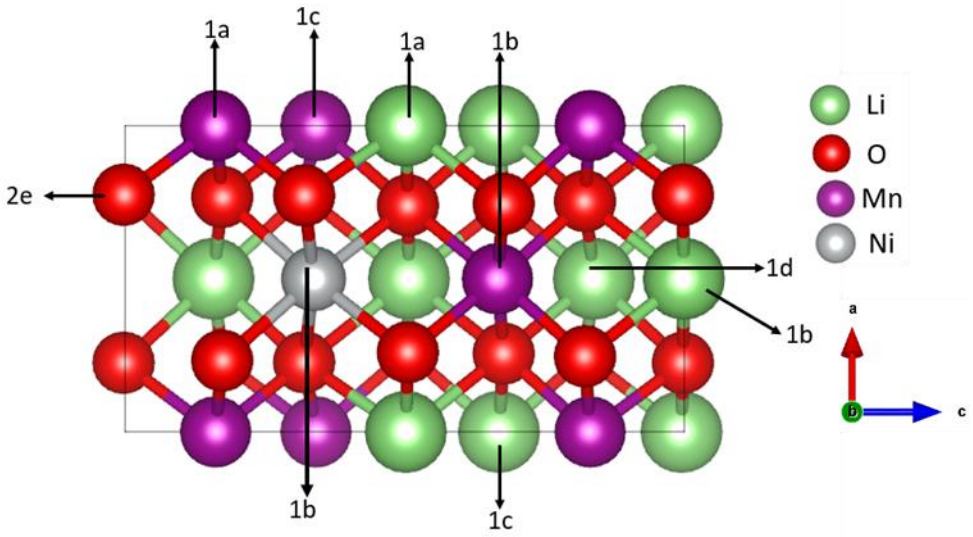

Figure 17: A schematic representation of a unit cell of the $Li_{1.2}Mn_{0.6}Ni_{0.2}O_2$ containing 75% of Mn and 25% of Ni and the Wyckoff positions of the Li, Mn, Ni, and O atoms.

The structure studied in this section ($Li_{1.2}Mn_{0.6}Ni_{0.2}$) was generated by cluster expansion wherein $Li_{1.2}Mn_{0.8}O_2$ was doped with nickel on all the manganese sites detailed in Chapter 4. $Li_{1.2}Mn_{0.6}Ni_{0.2}O_2$ is among the predicted stable structures and it contains the least number of nickel atoms from all the generated phases.

The crystal structure of $Li_{1.2}Mn_{0.6}Ni_{0.2}O_2$ is represented in figure 17 above, it shows 2 Mn and 1 Li atoms occupying the 1a site, 1 Mn and 2 Li in the 1c site, 1 Mn, 1 Ni, and 1 Li in the 1b site, 6 O atoms occupying the 2e site, and 3 Li atoms occupying the 1d site. Furthermore, $Li_{1.2}Mn_{0.6}Ni_{0.2}O_2$ has a space group symmetry of P1, it is a triclinic crystal with lattice parameters of the form $a \neq b \neq c$ and $\alpha \neq \beta \neq \gamma$ shown in table 6 below. The obtained lattice parameters differ from those found in literature which might be because with the structure in literature the symmetry of the material is C2/m whereas the material in this study is of the symmetry P1. The heats of formation of $Li_{1.2}Mn_{0.6}Ni_{0.2}O_2$ is negative implying thermodynamic stability. Furthermore, it is more negative than the heats of formation of $Li_{1.2}Mn_{0.8}O_2$ meaning that the addition of Nickel to the structure brought about an increase in the thermodynamic stability.

Table 6: Calculated lattice Parameters a, b, and c, the angles, volume, and heats of formation of the $Li_{1.2}Mn_{0.6}Ni_{0.2}O_2$ structure.

Lattice Parameters (Å)			Heats of Formation (kJ/mol)	Volume ($Å^3$)
VASP a=5.079 b=5.059 c=8.592	EXP [107] [108] a=4.939, a=4.962 b=8.548, b=8.571 c=9.637, c=5.035	VASP α= 90.132° β=90.024° γ= 110.834°	-4465.09	206.336

3.7 Mechanical properties

To evaluate the mechanical stability of the $Li_{1.2}Mn_{0.6}Ni_{0.2}O_2$ structure, the elastic constants of the materials were calculated and tabulated in table 7 below. The structure is a triclinic crystal with 21 independent elastic constants and for it to be considered mechanically stable, it must adhere to the conditions for the triclinic mechanical stability criteria given by the equations below: [109]

$$C_{11} > 0, C_{22} > 0, C_{33} > 0, C_{44} > 0, C_{55} > 0, C_{66} > 0 \quad (3.7\text{-}1)$$

$$[C_{11} + C_{22} + C_{33} + 2 \times (C_{12} + C_{13} + C_{23})] > 0 \quad (3.7\text{-}2)$$

$$(C_{33} \times C_{55} - C_{35}^2) > 0, (C_{44} \times C_{66} - C_{46}^2) > 0 \quad (3.7\text{-}3)$$

$$(C_{22} + C_{33} - 2 \times C_{23}) > 0 \quad (3.7\text{-}4)$$

In section 3.3 the elastic constants were calculated with different strains (0.001, 0.005, and 0.025) to check for the strain in which these types of materials show mechanical stability. The materials were all stable under strain 0.001 as explained in section 3.3 implying that these types of materials are mechanically stable under small strains. For this reason, the elastic constants of $Li_{1.2}Mn_{0.6}Ni_{0.2}O_2$ were calculated using strain 0.001. The mechanical stability criteria for triclinic crystals are satisfied by the calculated elastic constants shown in table 7 below, when incorporating the elastic constants into equations 3.7-1 to 3.7-3 the conditions are met. The findings suggests that the structure

$Li_{1.2}Mn_{0.6}Ni_{0.2}O_2$ exhibits mechanical stability when subjected to a strain of 0.001. Moreover, the presence of Ni in the structure does not compromise the mechanical stability of the material.

Table 7: Elastic Constants of the $Li_{1.2}Mn_{0.6}Ni_{0.2}O_2$ structure calculated under strain 0.001.

Elastic Constant (Cij)	$Li_{1.2}Mn_{0.6}Ni_{0.2}O_2$
C_{11}	213.01
C_{12}	46.83
C_{13}	59.12
C_{14}	1.77
C_{15}	1.87
C_{16}	18.55
C_{22}	245.40
C_{23}	63.34
C_{24}	0.35
C_{25}	0.56
C_{26}	4.54
C_{33}	262.82
C_{34}	1.13
C_{35}	1.14
C_{36}	-4.44
C_{44}	61.35
C_{45}	-27.63
C_{46}	0.27
C_{55}	62.60
C_{56}	0.45
C_{66}	73.06

To further examine the mechanical stability of this structure, the elastic moduli were considered. Table 8 displays the bulk, shear, and Young's moduli and as with the elastic constants, the elastic moduli were calculated under strain 0.001. The shear, bulk, and

Young's modulus values of $Li_{1.2}Mn_{0.6}Ni_{0.2}O_2$ are less than those of Li_2MnO_3 and $Li_{1.2}Mn_{0.8}O_2$ implying that $Li_{1.2}Mn_{0.6}Ni_{0.2}O_2$ has less compressive strength, less stiffness, and is less resistant to elastic deformation compared to Li_2MnO_3 and $Li_{1.2}Mn_{0.8}O_2$ under strain 0.001. The Pugh ratio further indicates that the material is brittle.

Table 8: Bulk, Shear, Young's modulus and Pugh's ratio of $Li_{1.2}Mn_{0.6}Ni_{0.2}O_2$ calculated with an applied strain of 0.001.

Structure	Bulk (GPa)	Shear (GPa)	Young's (GPa)	Pugh's ratio B/G	Ductility
$Li_{1.2}Mn_{0.6}Ni_{0.2}O_2$	117.76	76.20	188.03	1.55	Brittle

3.8 Density of states

The density of states was calculated to study the electronic behaviour of the $Li_{1.2}Mn_{0.6}Ni_{0.2}O_2$ structure and the obtained results are depicted in the plot of total density of states against energy in figure 18 below. Of the four atoms, the Mn and Ni atoms show the greatest contribution to the TDOS of the material. The O atom also shows contribution to the TDOS, it contributes better than the Li-atom but not greater than Mn and Ni. The Li-atom shows the least contribution to the TDOS of the material.

The Mn d-orbital is dominant in the conduction band from 0eV to 4eV wherein the shape of the Mn d orbital at this region matches that of the TDOS better than the other atoms do. This implies that at this region in the conduction band the Mn d-states have the greatest contribution. The contribution of the Mn p and s orbitals is little, the two are not dominant anywhere.

In the PDOS of the Ni atom, the Ni d-orbital shows a larger contribution than the p and s orbitals. The Ni d-orbital is dominant in the valence band at -3eV to 0eV, it also appears to be dominating in the conduction band at 0eV to 3eV but its contribution in this region is not greater than that of Mn-d. On the other hand, the Ni s and p orbital show very little contribution to the TDOS of the material. The Ni p-orbital is visible in the region between -8eV and -3eV, however its contribution is small. The oxygen p-orbital contributes to the TDOS of the material at -7eV to -3eV, it is the most dominant orbital at this region

compared to the orbitals of the other atoms. The s-orbital contributes to the valence band further away from the Fermi level, at -20eV to -18eV and the O d-orbital shows minimum contribution to the TDOS. The Fermi level falls onto a peak right after the pseudo gap as seen on the TDOS. The system is a half-metallic ferromagnetic metal with an indirect band gap of 0.00eV, a half-metallic ferromagnet refers to a material in which there is only one spin channel for conductions, the structure shows a metallic behaviour for one spin channel whereas the other spin shows a band gap at the Fermi level [110]. In the case of the $Li_{1.2}Mn_{0.6}Ni_{0.2}O_2$ structure, bands for spin one are metallic and bands for spin two are semiconducting.

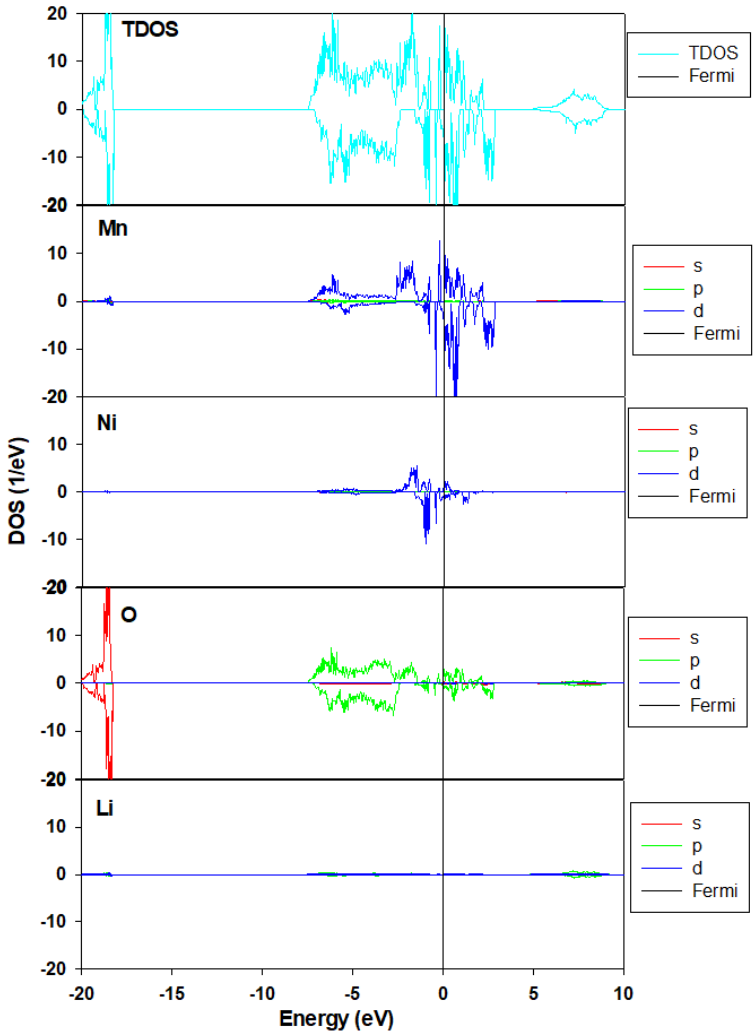

Figure 18: Spin polarized density of states of $Li_{1.2}Mn_{0.6}Ni_{0.2}O_2$ showing the total density of states of the structure and the partial density of states of the Mn, Ni, O, and Li atoms along with their orbital contributions.

Structural, Mechanical, and electronic properties of $Li_{1.2}Mn_{0.3}Ni_{0.5}O_2$.

3.9 Structural analysis

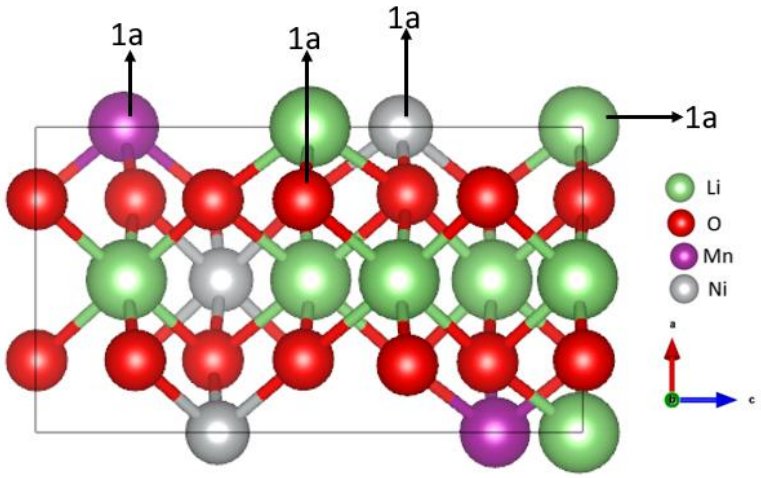

Figure 19: Unit cell representation of the $Li_{1.2}Mn_{0.3}Ni_{0.5}O_2$ crystal structure and Wyckoff positions of the Li, Mn, Ni, and O atoms.

The structure $Li_{1.2}Mn_{0.3}Ni_{0.5}O_2$ was obtained from the DFT ground state line on the binary phase diagram of Ni doped $Li_{1.2}Mn_{0.8}O_2$(detailed in chapter 4). Its crystal structure is represented in figure 19, the structure has 2 Mn, 3 Ni, 7 Li, and 12 O all occupying 1a sites. Moreover, $Li_{1.2}Mn_{0.3}Ni_{0.5}O_2$ has a space group symmetry of P1 and it is a triclinic crystal with lattice parameters of the form $a \neq b \neq c$ and $\alpha \neq \beta \neq \gamma$ as shown in the table 9 below. No literature information was found to compare the lattice parameters of the structure $Li_{1.2}Mn_{0.3}Ni_{0.5}O_2$ with.

The heat of formation of $Li_{1.2}Mn_{0.3}Ni_{0.5}O_2$ is negative implying thermodynamic stability, however, it is less negative than that of $Li_{1.2}Mn_{0.8}O_2$ and $Li_{1.2}Mn_{0.6}Ni_{0.2}O_2$ meaning that it is less thermodynamically stable than these structures. From this, it is evident that when the Ni content is greater than the Mn content there is a drastic increase in the formation energy leading to a decrease in thermodynamic stability. The cell volume is less compared to that of $Li_{1.2}Mn_{0.8}O_2$ and $Li_{1.2}Mn_{0.6}Ni_{0.2}O_2$, this is because $Li_{1.2}Mn_{0.3}Ni_{0.5}O_2$ has more Ni atoms than Mn atoms and Ni has a smaller atomic radius than Mn.

Table 9: calculated lattice parameters, volume and heats of formation of the $Li_{1.2}Mn_{0.3}Ni_{0.5}O_2$ structure.

Lattice parameters		Heats of formation (kJ/mol)	Volume ($Å^3$)
a=4.929 b=4.916 c=8.391	α=90.003° β=90.032° γ= 108.269°	-3901.45	193.093

3.10 Mechanical properties

As in section 3.7 above, elastic constants of the $Li_{1.2}Mn_{0.3}Ni_{0.5}O_2$ structure were calculated to evaluate the mechanical stability of the structure, and these were calculated using a strain of 0.001 since it was found in section 3.3 to be the strain in which these types of structures exhibit mechanical stability.

The structure $Li_{1.2}Mn_{0.3}Ni_{0.5}O_2$ has 21 independent elastic constants as illustrated in table 10 below suggesting that it has a triclinic crystal shape, hence for $Li_{1.2}Mn_{0.3}Ni_{0.5}O_2$ to be considered mechanically stable, its elastic constants must adhere to the triclinic mechanical stability criteria listed in equations 3.7-1 to 3.7.4. The calculated elastic constants as shown in table 10 satisfy the mechanical stability criteria in equations 3.7-1 to 3.7-4 suggesting that the structure $Li_{1.2}Mn_{0.3}Ni_{0.5}O_2$ is mechanically stable under the applied strain of 0.001.

Table 10: Elastic constants of the $Li_{1.2}Mn_{0.3}Ni_{0.5}O_2$ structure calculated with a strain of 0.001.

Elastic Constant (C_{ij})	$Li_{1.2}Mn_{0.3}Ni_{0.5}O_2$
C_{11}	198.68
C_{12}	-31.23
C_{13}	153.70
C_{14}	0.36
C_{15}	121.51
C_{16}	-94.36
C_{22}	26.46
C_{23}	69.67
C_{24}	-29.89
C_{25}	141.36
C_{26}	-116.00
C_{33}	283.22
C34	3.12
C_{35}	145.45
C_{36}	-7.10
C_{44}	64.66
C_{45}	-2.55
C_{46}	-4.72
C_{55}	176.22
C_{56}	26.62
C_{66}	79.05

The elastic moduli of the material were further considered to evaluate the mechanical stability of the material and table 11 below shows the bulk, shear, and Young's moduli. $Li_{1.2}Mn_{0.3}Ni_{0.5}O_2$ was found to have less shear, bulk, and Young's modulus values of than those of Li_2MnO_3, $Li_{1.2}Mn_{0.8}O_2$ and $Li_{1.2}Mn_{0.6}Ni_{0.2}O_2$ reported in the sections above. This implies that $Li_{1.2}Mn_{0.3}Ni_{0.5}O_2$ has less compressive strength, less stiffness, and is less resistant to elastic deformation. These findings show that with increasing nickel content,

the compressive strength, stiffness, and resistance to elastic deformation of the structure decreases. Moreover, the Pugh ratio was considered to evaluate the ductility of the structure and it was found that $Li_{1.2}Mn_{0.3}Ni_{0.5}O_2$ is brittle since it has a Pugh ratio less than 1.75 as indicated in table 11. This further indicates that an increase in the Ni content results in increased brittleness of the structure.

Table 11: Bulk, Shear, Young's modulus and Pugh's ratio of the $Li_{1.2}Mn_{0.3}Ni_{0.5}O_2$ structure.

Structure	Bulk (GPa)	Shear (GPa)	Young's (GPa)	Pugh's ratio B/G	Ductility
$Li_{1.2}Mn_{0.3}Ni_{0.5}O_2$	99.18	85.07	198.46	1.17	Brittle

3.11 Density of states

To study the electronic behaviour of the $Li_{1.2}Mn_{0.3}Ni_{0.5}O_2$ structure, the density of states was calculated, and the results are depicted in the density of states against energy plot in Figure 20 below.

From the partial density of states (PDOS) of the manganese atom it is observed that the Mn-d states are dominant more than the Mn-p states which show little contribution and the Mn-s states which do not show any contribution. We further observed that the shape of the Mn PDOS in the conduction region from 0.5eV to 2eV matches that of the total density of states (TDOS) of the bulk material in this region better than the other three atoms do, which suggests that the Mn atom has greater contribution to the TDOS of the material in the conduction band.

The PDOS of the Ni-atom shows that the Ni-d states are the most dominant states, and they show great contribution in the valence band between -2eV and -0.5eV and in the conduction band between -0.5eV and 1eV. The Ni-p states show little contribution, while the Ni-s states show no contribution. Furthermore, the shape of the Ni-d states resembles that of the TDOS in the valence band between -2eV and -0.5eV, implying that in the valence band the Ni-atom has greater contribution to the TDOS of the bulk material as compared to the other three atoms. Moreover, the Ni atom has a higher density of states

compared to the other three atoms implying that Ni has a great effect in the conductivity of the material.

The contribution of the O-atom and the Li-atom is little compared to that of the Ni and Mn atoms. Unlike in the other 3 atoms were the d-states are dominant, the O-p states are dominant in the PDOS of the oxygen atom, on the other hand, the O-d states have less contribution and the O-s states do not show any contribution. of all three atoms, the Li-atom show the least contribution to the TDOS of the bulk material. The dominant states in the PDOS of the Li-atom are the d-states.

Looking at the TDOS of the bulk structure $Li_{1.2}Mn_{0.3}Ni_{0.5}O_2$ it is observed that there is an overlap of electrons from the valence band to the conduction band resulting in no band gap at the Fermi level, these observations suggest that the structure is a conductor.

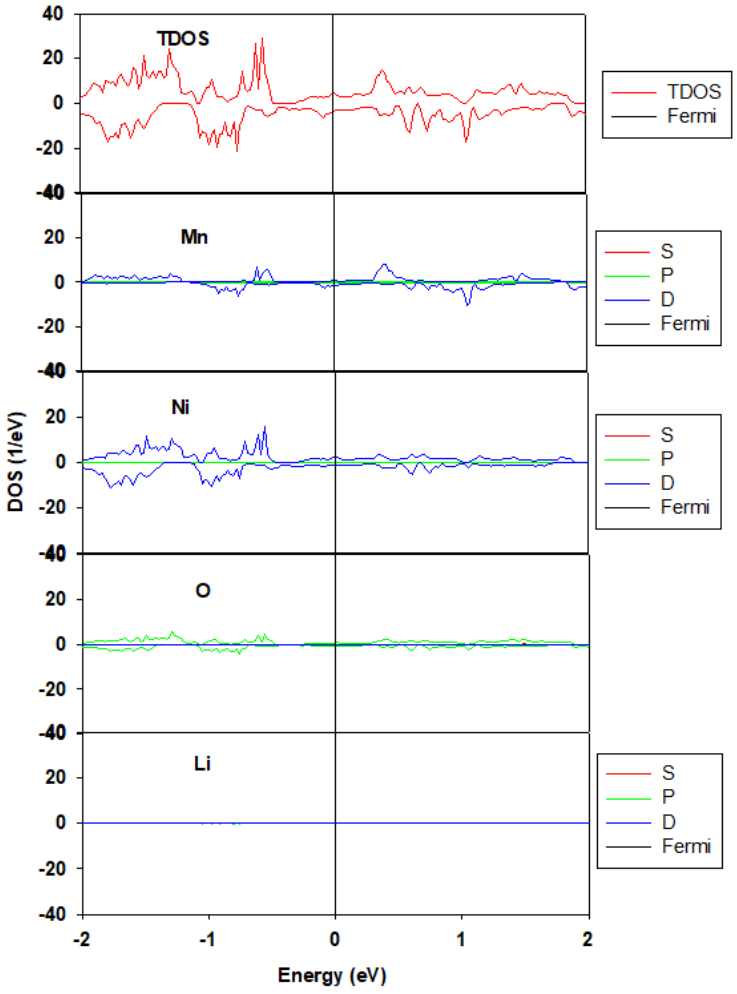

Figure 20: Spin polarized density of states of $Li_{1.2}Mn_{0.3}Ni_{0.5}O_2$ showing the total density of states of the bulk structure and partial density of states of the Li, Mn, Ni, and O atom and the contributions of their s, p, and d orbitals.

Structural, mechanical, and electronic properties of Co-doped $Li_{1.2}Mn_{0.6}Ni_{0.2}O_2$ phases.

This section details the analysis of structural and mechanical properties of phases obtained from the cluster expansion of Co-doped $Li_{1.2}Mn_{0.6}Ni_{0.2}O_2$ which is detailed in chapter 4. The structure $Li_{1.2}Mn_{0.6}Ni_{0.2}O_2$ was found as one of the generated stable structures by the cluster expansion of Ni-doped $Li_{1.2}Mn_{0.8}O_2$. After analysing the structure, it was found that the addition of nickel has enhanced the thermodynamic and electronic properties of the structure but compromised the ductility of the material as it was found to be more brittle than the pristine $Li_{1.2}Mn_{0.8}O_2$ structure. One Mn site was doped with 1 Co to investigate the effect that the presence of Co will have on the mechanical stability and ductility of the $Li_{1.2}Mn_{0.6}Ni_{0.2}O_2$ structure. Co was chosen due to the improved mechanical properties it exhibits when covalently bonded to Ni [111].

3.12 Structural analysis

Table 12 below details the cell parameters, volume, and heats of formation of the stable structures that lie on the DFT ground state line of the Co-doped $Li_{1.2}Mn_{0.6}Ni_{0.2}O_2$ binary diagram.

According to the lattice parameters shown in table 12 below, the cell parameters a, b, and c of the generated materials are large compared to those of the initial structure $Li_{1.2}Mn_{0.6}Ni_{0.2}O_2$. The volumes of the generated phases are also larger than the volumes of the parent structure $Li_{1.2}Mn_{0.6}Ni_{0.2}O_2$ and this suggests a successful insertion of cobalt into the system.

All the generated stable structures have heats of formation values less than that of the initial structure $Li_{1.2}Mn_{0.6}Ni_{0.2}O_2$, which implies that the addition of cobalt to the material does not compromise the thermal stability of the material. The most thermodynamically stable phase is $Li_{1.2}Mn_{0.63}Co_{0.04}Ni_{0.17}O_2$ since it has the lowest heat of formation.

Table 12: Calculated lattice parameters, volume, and heats of formation of the 4 most stable structures generated by the Co-doped $Li_{1.2}Mn_{0.6}Ni_{0.2}O_2$ cluster expansion.

Structure	Lattice parameters		Volume (Å^3)	Heats of formation (kJ/mol)
$Li_{1.2}Mn_{0.56}Co_{0.11}Ni_{0.17}O_2$	a=4.948 b=8.503 c=13.978	α=90.00 β=90.51 ɣ=90.00	588.107	-13003.70
$Li_{1.2}Mn_{0.61}Co_{0.06}Ni_{0.17}O_2$	a=4.969 b=8.535 c=14.001	α=90.00 β=90.76 ɣ=90.00	593.857	-13061.70
$Li_{1.2}Mn_{0.5}Co_{0.13}Ni_{0.17}O_2$	a=5.669 b=8.499 c=16.289	α=90.00 β=89.87 ɣ=90.00	784.889	-17276.46
$Li_{1.2}Mn_{0.63}Co_{0.04}Ni_{0.17}O_2$	a=5.799 b=16.264 c=8.660	α=90.00 β=90.00 ɣ=90.25	816.727	-60672.18

3.13 Mechanical properties

Elastic constants were calculated to evaluate the mechanical stability of the generated stable structures, these were calculated under a strain of 0.001. Some of the generated materials were found to be monoclinic with 13 independent elastic constants and some were found to be triclinic with 21 independent elastic constants. So, for these materials to be considered mechanically stable, the elastic constants need to satisfy the mechanical stability criteria of their respective crystal shapes, for which mechanical stability criteria for the monoclinic and triclinic crystals are listed in equations 3.3-1 to 3.3-5 and 3.7-1 to 3.7-4 respectively.

From the obtained elastic constants listed in table 13 below, $Li_{1.2}Mn_{0.5}Co_{0.13}Ni_{0.17}O_2$ has a negative C_{33} value, suggesting that this material is mechanically unstable as it does not satisfy all conditions of the monoclinic crystal stability criteria. On the other hand,

$Li_{1.2}Mn_{0.56}Co_{0.11}Ni_{0.17}O_2$, $Li_{1.2}Mn_{0.61}Co_{0.06}Ni_{0.17}O_2$, and $Li_{1.2}Mn_{0.63}Co_{0.04}Ni_{0.17}O_2$ adhere to all the conditions of the mechanical stability criteria of their crystal shapes implying that they are mechanically stable. There is no observed consistent trend with the elastic constants as the Co content increases, however the mechanical stability of the structure is maintained to a certain extant with the addition of Co.

Table 13: Elastic constants (calculated under strain 0.001) of the 4 stable phases that lie on the DFT ground state line of the Co-doped $Li_{1.2}Mn_{0.6}Ni_{0.2}O_2$ binary diagram.

Elastic constant C_{ij}	$Li_{1.2}Mn_{0.56}Co_{0.11}Ni_{0.17}O_2$	$Li_{1.2}Mn_{0.61}Co_{0.06}Ni_{0.17}O_2$	$Li_{1.2}Mn_{0.5}Co_{0.13}Ni_{0.17}O_2$	$Li_{1.2}Mn_{0.63}Co_{0.04}Ni_{0.17}O_2$
C_{11}	260.50	400.91	397.01	250.46
C_{12}	37.93	-39.42	70.16	66.66
C_{13}	32.23	89.65	-172.00	80.63
C_{22}	283.30	191.82	501.70	183.08
C_{23}	123.38	135.95	-54.59	80.38
C_{33}	362.44	238.21	-119.58	274.15
C_{44}	80.72	462.12	94.18	90.43
C_{46}	-6.18	123.27	-37.29	-1.37
C_{55}	105.88	33.19	112.50	39.51
C_{66}	56.49	95.84	31.37	107.37

Elastic moduli of the generated phases were considered for further evaluation of the mechanical stability of these phases and the results are tabulated in table 14 below. The bulk modulus was calculated to assess the phases' resistance to compression and the values obtained indicate that $Li_{1.2}Mn_{0.56}Co_{0.11}Ni_{0.17}O_2$ is the most resistant to compression as it has the highest bulk modulus values. The phase with the least resistance to compression is $Li_{1.2}Mn_{0.5}Co_{0.13}Ni_{0.17}O_2$ because it has the lowest bulk modulus value. From the shear modulus which indicates the stiffness of the material, it is observed that $Li_{1.2}Mn_{0.61}Co_{0.06}Ni_{0.17}O_2$ is the stiffest phase as it possesses the highest shear value. Furthermore, the Young's modulus was then used to evaluate the materials' resistance

to elastic deformation, and it is observed that $Li_{1.2}Mn_{0.61}Co_{0.06}Ni_{0.17}O_2$ has the highest Young's modulus value making it the most resistant to elastic deformation.

To check the ductility of the materials, the Pugh's ratio was calculated. $Li_{1.2}Mn_{0.56}Co_{0.11}Ni_{0.17}O_2$ and $Li_{1.2}Mn_{0.63}Co_{0.04}Ni_{0.17}O_2$ were found to be ductile whereas $Li_{1.2}Mn_{0.61}Co_{0.06}Ni_{0.17}O_2$ and $Li_{1.2}Mn_{0.5}Co_{0.13}Ni_{0.17}O_2$ are brittle. The presence of cobalt in $Li_{1.2}Mn_{0.6}Ni_{0.2}O_2$ has the ability to enhance the ductility of the material at certain Co, Ni, and Mn concentrations.

Table 14: Elastic moduli of the 4 phases that lie on the DFT ground state line of the Co-doped $Li_{1.2}Mn_{0.6}Ni_{0.2}O_2$ binary diagram.

Structure	Bulk (GPa)	Shear (GPa)	Young's (GPa)	Pugh's ratio B/G	Ductility
$Li_{1.2}Mn_{0.56}Co_{0.11}Ni_{0.17}O_2$	143.70	53.78	143.44	2.672	Ductile
$Li_{1.2}Mn_{0.61}Co_{0.06}Ni_{0.17}O_2$	91.07	135.64	271.92	0.671	Brittle
$Li_{1.2}Mn_{0.5}Co_{0.13}Ni_{0.17}O_2$	51.81	97.43	179.66	0.532	Brittle
$Li_{1.2}Mn_{0.63}Co_{0.04}Ni_{0.17}O_2$	129.23	63.66	164.04	2.029	Ductile

3.14 Fluorination

This section of chapter 3 focuses on the fluorination of $Li_{1.2}Mn_{0.8}O_2$ and $Li_{1.2}Mn_{0.6}Ni_{0.2}O_2$ wherein the materials are doped with fluorine on all oxygen sites then subjected to cluster expansion (detailed in chapter 4) for the generation of new phases of the doped systems. The reason for choosing fluorine is that it has been demonstrated that fluorination reduces oxygen loss and boosts power density in Li-rich cathode materials [112].

3.14.1 Fluorine doped $Li_{1.2}Mn_{0.8}O_2$

$Li_{1.2}Mn_{0.8}O_2$ was doped with fluorine on all oxygen 2e sites, thereafter, the genetic algorithm approach was employed for the generation of new phases of the fluorine doped $Li_{1.2}Mn_{0.8}O_2$. 78 new phases were generated and of the 78, 11 lie on the ground state line (depicted in chapter 4) and these are considered as the most stable phases. These phases are $Li_{1.2}Mn_{0.8}F_2$, $Li_{1.2}Mn_{0.8}O_{0.17}F_{1.83}$, $Li_{1.2}Mn_{0.8}O_{0.33}F_{1.67}$, $Li_{1.2}Mn_{0.8}O_{0.5}F_{1.5}$, $Li_{1.2}Mn_{0.8}O_{0.67}F_{1.33}$, $Li_{1.2}Mn_{0.8}O_{0.83}F_{1.17}$, $Li_{1.2}Mn_{0.8}OF$, $Li_{1.2}Mn_{0.8}O_{1.17}F_{0.83}$,

$Li_{1.2}Mn_{0.8}O_{1.33}F_{0.67}$, $Li_{1.2}Mn_{0.8}O_{1.5}F_{0.5}$, $Li_{1.2}Mn_{0.8}O_{1.67}F_{0.33}$, $Li_{1.2}Mn_{0.8}O_{1.83}F_{0.17}$, and $Li_{1.2}Mn_{0.8}O_2$.

Structural properties of the 11 stable phases were calculated to analyse the type of structures generated and the results are shown in Table 15 below. Some of the generated phases are triclinic with lattice parameters of the form a ≠ b ≠ c and α ≠ β ≠ ɣ and some of the phases are monoclinic with lattice parameters of the form a ≠ b ≠ c and α=ɣ=90º≠β. Furthermore, some of the new phases have space group symmetry of P1 and others have a P2 space group symmetry.

It is observed that for phases containing both Fluorine and Oxygen, the lattice parameters increase with the increase in the number of fluorine atoms and decrease for phases with no mixture of fluorine and oxygen, i.e., $Li_{1.2}Mn_{0.8}F_2$ and $Li_{1.2}Mn_{0.8}O_2$ and these are the parent structures. The heat of formation is less for the phases with more fluorine atoms than oxygen atoms, this suggests that the presence of fluorine enhances the thermodynamic stability of the structure. Apart from the parent structures, the most thermodynamically stable phase is $Li_{1.2}Mn_{0.8}O_{0.17}F_{1.83}$ as it has the lowest heat of formation. Although the addition of fluorine improves the thermodynamic stability, it is only to a certain extent meaning that the ratio of the oxygens to the fluorine also plays a part in the enhancement.

Table 15: Lattice parameters, volume, and heats of formation of the most stable phases generated by the ground state search of the F-doped $Li_{1.2}Mn_{0.8}O_2$ system.

Structure	Lattice parameters		Heats of formation (kJ/mol)	Volume ($Å^3$)	Raised symmetry
$Li_{1.2}Mn_{0.8}F_2$	a=4.98 b=11.58 c=4.79	α=90 β=85.47 γ=90	-5116.79	275.86	P2
$Li1.2Mn_{0.8}O_{0.17}F_{1.83}$	a=5.33 b= 5.47 c=10.4	α=92.74 β=83.02 γ=112.88	-5016.75	277.62	P1
$Li_{1.2}Mn_{0.8}O_{0.33}F_{1.67}$	a=5.49 b=5.49 c=9.50	α=89.97 β=90.8 γ= 111.67	-4587.26	266.17	P1
$Li_{1.2}Mn_{0.8}O_{0.5}F_{1.5}$	a=5.11 b=5.06 c=9.70	α=91.24 β=89.79 γ= 104.18	-4951.13	243.29	P1
$Li_{1.2}Mn_{0.8}O_{0.67}F_{1.33}$	a=5.19 b=9.51 c=5.00	α=90 β=74.68 γ= 90	-4421.33	238.09	P2
$Li_{1.2}Mn_{0.8}O_{0.83}F_{1.17}$	a=5.16 b=5.13 c=9.39	α=90.19 β=89.97 γ= 105.37	-4635.01	240.04	P1
$Li_{1.2}Mn_{0.8}OF$	a=5.03 b=5.05 c=9.49	α=89.33 β=89.58 γ= 103.49	-4611.32	234.737	P1
$Li_{1.2}Mn_{0.8}O_{1.17}F_{0.83}$	a=5.09 b=5.07 c=9.18	α=90.63 β=90.98 γ= 105.43	-4575.87	228.69	P1
$Li_{1.2}Mn_{0.8}O_8F_4$	a=5.05	α=89.98	-4820.94	223.69	P1

	b=5.04 c=9.12	β=90.16 γ= 105.31			
$Li_{1.2}Mn_{0.8}O_{1.5}F_{0.5}$	a=5.03 b=4.99 c=9.00	α=90.19 β=89.7 γ= 105.02	-4537.66	218.6	P1
$Li_{1.2}Mn_{0.8}O_{1.67}F_{0.33}$	a=4.94 b=4.97 c=9.07	α=89.16 β=88.35 γ= 105.56	-4648.20	214.21	P1
$Li_{1.2}Mn_{0.8}O_{1.83}F_{0.17}$	a=4.98 b=4.97 c=8.76	α=89.51 β=89.30 γ= 107.37	-4612.77	206.84	P1
$Li_{1.2}Mn_{0.8}O_2$	a=4.92 b=4.90 c=8.49	α=89.94 β=89.98 γ= 109.40	-4090.78	216.11	P2

3.14.1.1 Density of states

The density of states of the generated structures that lie on the ground state line of the binary phase diagram of the fluorine doped $Li_{1.2}Mn_{0.8}O_2$ were calculated to study the electronic behaviour of these structures and to evaluate the effect of the presence of fluorine on the conductivity of $Li_{1.2}Mn_{0.8}O_2$ structure. The results of the density of states of these new structures are shown in Figures 21 and 22 below.

Figure 21a shows the density of states of $Li_{1.2}Mn_{0.8}F_2$, this is the structure at x=0 on the binary diagram and it has no oxygen concentration. This material is a half metallic ferromagnet, and a half-metal ferromagnet is a material that has electrons at the Fermi level in a single spin state, either spin up or spin down. This means that it can act as a conductor with electrons of one spin orientation but an insulator or semiconductor to those of the opposite spin, in this regard, bands for spin 2 are metallic and bands of spin 1 are semiconducting. It was found that the material has an indirect band gap of 0.00eV at Fermi level, furthermore, the Fermi line falls onto a peak. The density of states of the structure $Li_{1.2}Mn_{0.8}O_{0.33}F_{1.67}$ showed that there is no overlap of electrons from the valence band to the conduction band, as a result there is a band gap of 0.341eV at the Fermi level

as shown in figure 21b. the presence of this band gap suggest that $Li_{1.2}Mn_{0.8}O_{0.33}F_{1.67}$ is a semiconductor.

The density of states of $Li_{1.2}Mn_{0.8}O_{0.5}F_{1.5}$ is shown in figure 21c, and with this structure it was also observed that the is no overlap of electrons from the valence band to the conduction band leading to an indirect band gap of 0.234eV at the Fermi level and implying that the structure is a semiconductor.

Figure 21d shows the density of states of $Li_{1.2}Mn_{0.8}O_{0.67}F_{1.33}$, as seen in the plot, the electrons overlap from the valence band to the conduction band leading to a system with no band gap at the Fermi level. As a result, the system is a half metallic ferromagnet with bands of spin 2 being metallic and bands of spin 1 are semiconducting.

With the $Li_{1.2}Mn_{0.8}O_{0.83}F_{1.17}$ structure, there is a band gap present at the Fermi level as seen in figure 21e. The band gap is of a value 0.022eV, and with this structure it is observed that the Fermi line falls into a pseudo gap. The presence of this band gap at the Fermi level suggests that the $Li_{1.2}Mn_{0.8}O_{0.83}F_{1.17}$ structure is a semiconductor.

$Li_{1.2}Mn_{0.8}OF$ which was predicted to be the most stable generated phase on the binary diagram contains an equal amount of fluorine and oxygen atoms. Its density of states is shown in figure 21f below and it was found that the structure has no band gap at the Fermi as there is an overlap of electrons from the valence band to the conduction band, this suggests that the structure is a magnetic metal and therefor a conductor.

In figure 22a we have a representation of the density of states plot of the $Li_{1.2}Mn_{0.8}O_{1.17}F_{0.83}$ structure. This structure has no band gap, and the Fermi level falls onto a pseudo gap as seen in the diagram. The structure is a half metallic ferromagnet with its bands for spin 2 being metallic and the bands for spin 1 are semiconducting. The density of states for the structure $Li_{1.2}Mn_{0.8}O_{1.33}F_{0.67}$ is shown in figure 22b and for this material it was observed that there is no overlap of electrons at Fermi level and the Fermi line falls into the gap. This led to an indirect band gap of 0.017eV suggesting that the $Li_{1.2}Mn_{0.8}O_{1.33}F_{0.67}$ structure is a magnetic semiconductor.

Figure 22c is the density of states of $Li_{1.2}Mn_{0.8}O_{1.5}F_{0.5}$ structure and from this plot it is evident that the electrons do not overlap from the valence band to the conduction band leading to an energy band gap at the Fermi level. The structure has a band gap of

0.232eV at the Fermi level and it is a half metallic ferromagnet wherein the bands for spin 1 are metallic and those of spin 2 are semiconducting.

Figure 22d is a representation of the density of states of the $Li_{1.2}Mn_{0.8}O_{1.67}F_{0.33}$ structure. The plot shows that electrons do not overlap from the valence band to the conduction band leading to a band gap at the Fermi level and a system that is a magnetic semiconductor with an indirect band gap of 0.019eV.

The phase with the lowest number of oxygen atoms from the generated phases is $Li_{1.2}Mn_{0.8}O_{0.17}F_{1.83}$ and its density of states is shown in figure 22e. The structure was found to be magnetic semiconductor with an indirect band gap of 0.028eV. The last phase is $Li_{1.2}Mn_{0.8}O_{1.83}F_{0.17}$ with the least number of fluorine atoms and the density of states represented in figure 22f. This structure was found to be a magnetic semiconductor with an indirect band gap of 0.039eV.

Of all the new phases, $Li_{1.2}Mn_{0.8}O_{0.33}F_{1.67}$ is the only phase whose band gap increased compared to that of the initial structure $Li_{1.2}Mn_{0.8}O_2$, it has a gap of 0.341eV which is greater than 0.269eV of $Li_{1.2}Mn_{0.8}O_2$. This implies that with this concentration of oxygen and fluorine, the conductivity of the material is not improved since a band gap of 0.341eV indicates that the structure $Li_{1.2}Mn_{0.8}O_{0.33}F_{1.67}$ is much closer to being an insulator than the parent structure is.

The phase which showed great improvement in conductivity is $Li_{1.2}Mn_{0.8}OF$ which is predicted to be a magnetic metal with no band gap at the Fermi level. From these densities of states, we can see that for the conductivity of the material to be good, the concentration difference of oxygen and fluorine must be little. For example, $Li_{1.2}Mn_{0.8}O_{0.83}F_{1.17}$ and $Li_{1.2}Mn_{0.8}OF$ show better conductivity compared to those with a large difference between the O and F concentration, for example $Li_{1.2}Mn_{0.8}O_{0.33}F_{1.67}$. Furthermore, it is observed that the presence of fluorine in the structure has potential to move the structure from being a semiconductor to a conductor since all the new phases with band gaps had band gaps that are very small compared to the band gap of the parent structure $Li_{1.2}Mn_{0.8}O_2$.

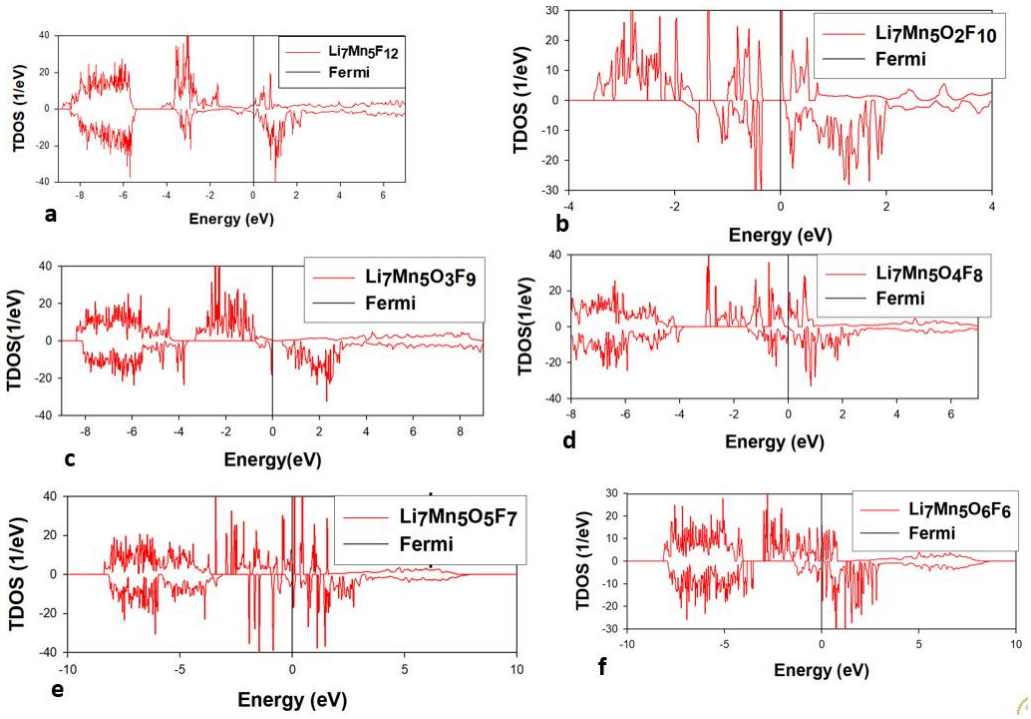

Figure 21: Spin polarized total densities of states of the stable phases generated from the ground state search of the F-doped $Li_{1.2}Mn_{0.8}O_2$ system.

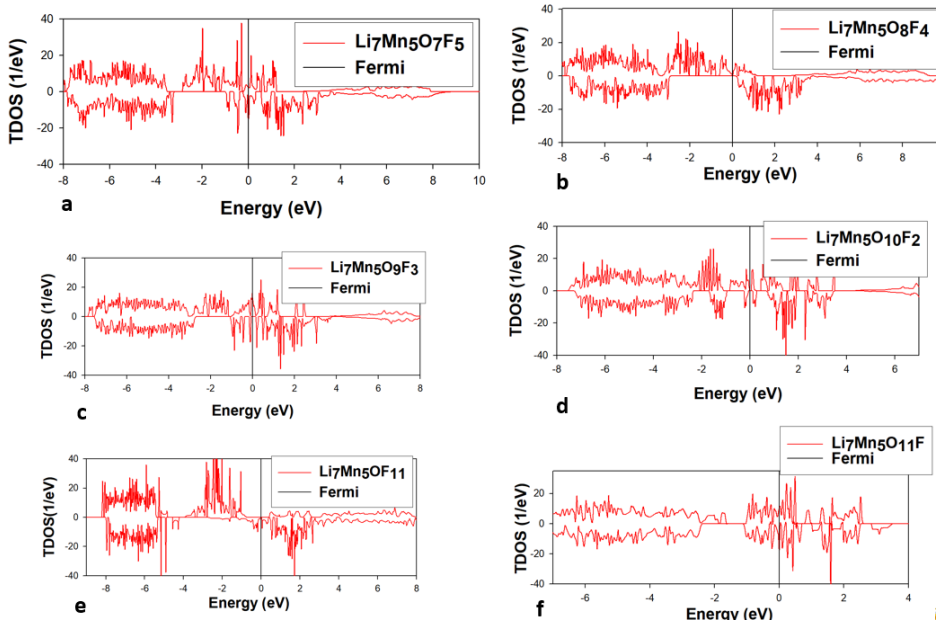

Figure 22: Spin polarized total densities of states of stable phases generated from F-doped $Li_{1.2}Mn_{0.8}O_2$ ground state search.

3.14.1.2 Mechanical properties

This section discusses the elastic properties of the stable phases that were generated from the F-doped $Li_{1.2}Mn_{0.8}O_2$, these elastic constants were calculated with a strain of 0.001 and the obtained elastic constants are listed in table 16 below.

Since the generated phases are monoclinic and some are triclinic, their elastic constants need to satisfy the mechanical stability criteria of their respective crystal shapes for the phases to be considered mechanically stable, for which the monoclinic and triclinic mechanical stability criteria are listed in equations 3.3-1 to 3.3-5 and 3.7-1 to 3.7-4 respectively.

From the calculated elastic constants listed in table 16 below, the structures $Li_{1.2}Mn_{0.8}F_2$, $Li_{1.2}Mn_{0.8}O_{0.17}F_{1.83}$, $Li_{1.2}Mn_{0.8}O_{0.33}F_{1.67}$, $Li_{1.2}Mn_{0.8}O_{0.5}F_{1.5}$, $Li_{1.2}Mn_{0.8}O_{0.83}F_{1.17}$, $Li_{1.2}Mn_{0.8}O_{1.33}F_{0.67}$, and $Li_{1.2}Mn_{0.8}O_{1.5}F_{0.5}$ are mechanically stable as their obtained elastic constants adhere to all the stability conditions of their crystal shapes. On the other hand, $Li_{1.2}Mn_{0.8}O_{0.67}F_{1.33}$, $Li_{1.2}Mn_{0.8}O_{0.5}F_{1.5}$, $Li_{1.2}Mn_{0.8}OF$, $Li_{1.2}Mn_{0.8}O_{1.67}F_{0.33}$, and $Li_{1.2}Mn_{0.8}O_{1.83}F_{0.17}$ are mechanically unstable since their elastic constants do not meet all the stability conditions. Of all the materials $Li_{1.2}Mn_{0.8}OF$ has the least C_{ij} values suggesting that it is the most mechanically unstable generated phase and the phase with the highest C_{ij} values is $Li_{1.2}Mn_{0.8}O_{1.83}F_{0.17}$ meaning that it is the most mechanically stable generated phase in relation to the elastic constants. There is no consistent trend with the elastic constants as we increase the fluorine content, however, majority of the structures with more fluorine atoms than oxygen atoms have low C_{ij} values than the structures with more oxygen atoms suggesting that a high content of fluorine in the structure reduces the mechanical stability of the material.

Table 16: Elastic constants of stable structures that lie on the DFT ground state line of the F-doped $Li_{1.2}Mn_{0.8}O_2$ binary diagram.

Elastic constant C_{ij}	C_{11}	C_{12}	C_{13}	C_{22}	C_{23}	C_{33}	C_{44}	C_{46}	C_{55}	C_{66}
$Li_{1.2}Mn_{0.8}F_2$	142.15	44.49	47.00	85.52	51.70	122.90	35.57	3.15	36.57	27.58
$Li_{1.2}Mn_{0.8}O_{0.17}F_{1.83}$	52.64	30.38	29.23	81.46	41.74	75.28	17.06	-4.06	23.44	12.36
$Li_{1.2}Mn_{0.8}O_{0.33}F_{1.67}$	84.90	34.90	49.37	98.05	39.72	24.41	15.84	4.99	29.44	11.58
$Li_{1.2}Mn_{0.8}O_{0.5}F_{1.5}$	152.92	57.27	62.03	159.44	55.84	116.31	26.15	2.50	34.88	41.32
$Li_{1.2}Mn_{0.8}O_{0.67}F_{1.33}$	2175.40	579.99	1793.27	740.14	1700.4	1954.99	1365.93	509.90	-1631	-1649.02
$Li_{1.2}Mn_{0.8}O_{0.83}F_{1.17}$	166.67	52.88	58.02	166.83	56.16	121.84	44.20	1.17	47.61	45.37
$Li_{1.2}Mn_{0.8}OF$	-1067.10	-877.61	-988.78	-1326.29	-962.96	-161.17	151.62	-324.47	-42.67	-293.52
$Li_{1.2}Mn_{0.8}O_{1.17}F_{0.83}$	183.87	44.37	53.46	160.85	42.64	134.67	32.86	-4.31	-96.9	56.24
$Li_{1.2}Mn_{0.8}O_{1.33}F_{0.67}$	179.97	16.39	58.36	159.52	45.00	137.08	37.28	4.70	48.64	45.22
$Li_{1.2}Mn_{0.8}O_{1.5}F_{0.5}$	208.60	54.54	63.90	220.65	68.36	185.91	61.97	-1.39	71.05	68.79
$Li_{1.2}Mn_{0.8}O_{1.67}F_{0.33}$	233.85	61.34	72.68	233.89	70.57	194.60	62.08	-3.16	81.02	78.35
$Li_7Mn_5O_{1.83}F_{0.17}$	1102.6	861.52	463.60	860.99	270.19	181.69	45.19	138.47	517.99	246.69
$Li_{1.2}Mn_{0.8}O_2$	227.58	81.87	85.11	246.05	89.46	257.89	78.51	11.27	96.45	84.79

To assess the mechanical stability of the materials even more, the elastic moduli of the generated phases were computed. The obtained bulk, shear, and Young's modulus along with the Pugh's ratio are listed in table 17 below, wherein the bulk modulus measures how resistant a material is to compression, shear modulus is a measure of a material's rigidity. If a material has a high shear value, it is a rigid solid and it implies that a large force is required to cause deformation on the material. Young's modulus defines a material's resistance to elastic deformation [113].

According to the bulk, shear, and Young's modulus values listed in table 17, $Li_{1.2}Mn_{0.8}OF$ has the lowest values which indicates that it has the least resistance to compression, it is less rigid and has the least resistance to elastic deformation out of all the generated materials. $Li_{1.2}Mn_{0.8}O_{1.83}F_{0.17}$ on the other hand has the highest shear, bulk, and Young's modulus values suggesting that it has the most resistance to compression, it is the most

rigid and it has the highest resistance to elastic deformation compared to the rest of the generated materials.

Furthermore, the structures with high modulus values are those with less fluorine atoms than oxygen atoms. The results of the elastic moduli correspond to those of the elastic constants such that $Li_{1.2}Mn_{0.8}OF$ has the least values and $Li_{1.2}Mn_{0.8}O_{1.83}F_{0.17}$ has the highest values. In addition, the Pugh's ratio of the materials was calculated to analyse the ductility of the materials. With the Pugh's ratio, if the value is >1.75 the material is considered ductile, otherwise it is brittle [114]. Majority of the generated phases are ductile, in addition, most of the ductile phases are those with more fluorine atoms than oxygen atoms. This suggests that the addition of fluorine to the structure $Li_{1.2}Mn_{0.8}O_2$ enhances the ductility of the material at certain concentrations of fluorine.

Table 17: Elastic moduli of stable structures constituting the DFT ground state line on the binary diagram of the F-doped $Li_{1.2}Mn_{0.8}O_2$.

Elastic moduli	Bulk (GPa)	Shear (GPa)	Young's (GPa)	Pugh's ratio	Ductility
$Li_{1.2}Mn_{0.8}F_2$	70.78	33.78	87.42	2.096	Ductile
$Li_{1.2}Mn_{0.8}O_{0.17}F_{1.83}$	45.79	17.77	47.21	2.576	Ductile
$Li_{1.2}Mn_{0.8}O_{0.33}F_{1.67}$	50.59	16.93	45.70	2.988	Ductile
$Li_{1.2}Mn_{0.8}O_{0.5}F_{1.5}$	86.55	37.37	98.01	2.316	Ductile
$Li_{1.2}Mn_{0.8}O_{0.67}F_{1.33}$	1446.44	-329.78	-1070.70	-4.386	Brittle
$Li_{1.2}Mn_{0.8}O_{0.83}F_{1.17}$	87.72	46.66	118.89	1.880	Ductile
$Li_{1.2}Mn_{0.8}OF$	-912.58	-18.60	-55.41	49.076	Ductile
$Li_{1.2}Mn_{0.8}O_{1.17}F_{0.83}$	84.48	21.03	58.27	4.016	Ductile
$Li_{1.2}Mn_{0.8}O_{1.33}F_{0.67}$	79.56	50.02	124.05	1.591	Brittle
$Li_{1.2}Mn_{0.8}O_{1.5}F_{0.5}$	109.86	68.92	171.00	1.594	Brittle
$Li_{1.2}Mn_{0.8}O_{1.67}F_{0.33}$	119.06	74.81	185.56	1.592	Brittle
$Li_{1.2}Mn_{0.8}O_{1.83}F_{0.17}$	592.76	198.68	536.13	2.984	Ductile
$Li_{1.2}Mn_{0.8}O_2$	143.82	86.96	217.11	1.654	Brittle

3.14.2 Fluorine doped $Li_{1.2}Mn_{0.6}Ni_{0.2}O_2$

$Li_{1.2}Mn_{0.6}Ni_{0.2}O_2$ was doped with fluorine on the 2e oxygen sites to investigate the effect of having both fluorine and nickel on the structural, mechanical, and electronic properties of the $Li_{1.2}Mn_{0.8}O_2$ structure. The doped structure was then subjected to cluster expansion for the generation of new structures by the genetic algorithm approach. 165 new phases were generated and out of the 165 generated phases, 8 of the phases lie on the DFT ground state line, these are regarded as the most stable phases. These phases are $Li_{1.2}Mn_{0.6}Ni_{0.2}O_{0.17}F_{1.83}$, $Li_{1.2}Mn_{0.6}Ni_{0.2}O_{0.33}F_{1.67}$, $Li_{1.2}Mn_{0.6}Ni_{0.2}O_{0.83}F_{1.17}$, $Li_{1.2}Mn_{0.6}Ni_{0.2}OF$, $Li_{1.2}Mn_{0.6}Ni_{0.2}O_{1.33}F_{0.67}$, $Li_{1.2}Mn_{0.6}Ni_{0.2}O_{1.5}F_{0.5}$, $Li_{1.2}Mn_{0.6}Ni_{0.2}O_{1.67}F_{0.33}$, and $Li_{1.2}Mn_{0.6}Ni_{0.2}O_{1.83}F_{0.17}$.

To analyse the types of structures that were formed, the structural parameters of the 8 stable phases were determined and the results are displayed in table 18 below. Some of the generated phases are triclinic with lattice parameters of the form $a \neq b \neq c$ and $\alpha \neq \beta \neq \gamma$ and some of the phases are monoclinic with lattice parameters of the form $a \neq b \neq c$ and $\alpha=\gamma=90^{o}\neq\beta$. Furthermore, the new phases have space group symmetry of P1.

The obtained cell parameter a and b of all the stable generated phases are greater than those of the parent structure $Li_{1.2}Mn_{0.6}Ni_{0.2}O_2$, furthermore, the cell volumes are also larger than the cell volume of the parent structure, which is an indication of fluorine being successfully added to the structures. The heats of formation of all the generated phases are negative indicating that the generated phases are thermodynamically stable. In addition, this suggests that the addition of fluorine into $Li_{1.2}Mn_{0.6}Ni_{0.2}O_2$ does not compromise the thermal stability of the material. The most thermodynamically stable phase is $Li_{1.2}Mn_{0.6}Ni_{0.2}O_{1.33}F_{0.67}$ as it has the lowest heat of formation.

Table 18: Cell parameters, heats of formation, volume and cell symmetry of stable structures generated by the F-doped $Li_{1.2}Mn_{0.6}Ni_{0.2}O_2$ cluster expansion.

Structure	Lattice parameters		Heats of formation (kJ/mol)	Volume (Å^3)	Symmetry
$Li_{1.2}Mn_{0.6}Ni_{0.2}O_{0.17}F_{1.83}$	a=5.200 b=10.737 c=5.161	α=82.504 β=110.045 ɣ=101.138	-4026.46	264.977	P1
$Li_{1.2}Mn_{0.6}Ni_{0.2}O_{0.33}F_{1.67}$	a=6.275 b=8.474 c=6.355	α=85.032 β=126.554 ɣ=87.743	-3962.26	268.661	P1
$Li_{1.2}Mn_{0.6}Ni_{0.2}O_{0.83}F_{1.17}$	a=5.403 b=8.887 c=5.317	α=90.922 β=113.117 ɣ=91.395	-4024.09	234.622	P1
$Li_{1.2}Mn_{0.6}Ni_{0.2}OF$	a=5.293 b=8.835 c=5.274	α=90.296 β=112.707 ɣ=90.565	-4046.27	227.505	P1
$Li_{1.2}Mn_{0.6}Ni_{0.2}O_{1.33}F_{0.67}$	a=5.064 b=9.148 c=5.071	α=92.995 β=107.256 ɣ=93.193	-4061.86	223.374	P1
$Li_{1.2}Mn_{0.6}Ni_{0.2}O_{1.5}F_{0.5}$	a=5.143 b=8.621 c=5.163	α=90.023 β=111.906 ɣ=89.985	-4059.69	212.378	P1
$Li_{1.2}Mn_{0.6}Ni_{0.2}O_{1.67}F_{0.33}$	a=5.077 b=8.712 c=5.076	α=89.549 β=109.408 ɣ=90.381	-4014.12	211.758	P1
$Li_{1.2}Mn_{0.6}Ni_{0.2}O_{1.83}F_{0.17}$	a=5.011 b=8.581 c= 5.069	α=90.744 β=111.155 ɣ= 90.572	-4026.46	203.232	P1

3.14.2.1 Density of states

The density of states of the stable generated structures that lie on the DFT ground state line of the binary diagram of the F-doped $Li_{1.2}Mn_{0.6}Ni_{0.2}O_2$ were calculated to investigate the effect of fluorine on the electronic conductivity of the material $Li_{1.2}Mn_{0.6}Ni_{0.2}O_2$. The results of the density of states of these new structures are plotted in Figures 23 and 24 below.

Figure 23a shows the density of states of the $Li_{1.2}Mn_{0.6}Ni_{0.2}O_{0.17}F_{1.83}$ structure, this structure contains 8.33% of oxygen and 91.67% of fluorine, of all the stable generated phases it contains the least amount of oxygen. As seen in the diagram, there is no overlap of electrons from the valence band to the conduction band and as a result this structure does not have a band gap at the Fermi level suggesting that the structure is a magnetic metal.

The density of states of the $Li_{1.2}M_{0.6}Ni_{0.2}O_{0.33}F_{1.67}$ structure is depicted in Figure 23b, with this structure it is observed that at the Fermi level there is an electron overlap from the valence band to the conduction band resulting in a band gap at the Fermi level. This structure has a band gap of 0.473eV at the Fermi level and the presence of this band gap at the Fermi level suggests that the structure is a semi-conductor.

The density of states of $Li_{1.2}Mn_{0.6}Ni_{0.2}O_{0.83}F_{1.17}$ is shown in figure 23c and it is observed that for this structure the Fermi line falls onto the peak and there is an observed overlap of electrons from the valence band to the conduction band at the Fermi level, however, there exists a band gap after the Fermi level. The material was predicted to a half-metallic ferromagnet with bands of spin 1 being metallic and bands of spin 2 being semi-conducting, furthermore, it was predicted to have a band gap of 1.589eV.

$Li_{1.2}Mn_{0.6}Ni_{0.2}OF$ containing 50% fluorine and 50% oxygen is a magnetic semiconductor with an indirect band gap of 0.165eV at the Fermi level as shown in figure 23d. As seen in the plot, the Fermi level falls into a gap and there is no overlap of electrons from the valence band to the conduction band which resulted in the band gap.

The density of states of the $Li_{1.2}Mn_{0.6}Ni_{0.2}O_{1.33}F_{0.67}$ structure is represented in figure 24a. As shown in the diagram, the electrons do not overlap from the valence to the conduction band leading to a band gap at the fermi level. This structure has an indirect band gap of 0.232eV and it is predicted to be a semiconductor.

$Li_{1.2}Mn_{0.6}Ni_{0.2}O_{1.5}F_{0.5}$ containing 75% O and 25% F is a half-metallic ferromagnet with an indirect band gap of 0.00eV and the bands for spin 1 in this structure are semiconducting and the bands for spin 2 are metallic. It is evident from the DOS plot in figure 24b that there is an overlap of electrons from the valence band to the conduction band which then results to the absence of a band gap for this material. $Li_{1.2}Mn_{0.6}Ni_{0.2}O_{1.66}F_{0.33}$ with the density of states shown in figure 24c shows an overlap of electrons from the valence band to the conduction band, as a result the structure was found to be a half metallic ferromagnet with an indirect band gap of 0.00eV. In this structure bands for spin 1 are semiconducting and bands for spin 2 are metallic. $Li_{1.2}Mn_{0.6}Ni_{0.2}O_{1.83}F_{0.16}$ containing the least amount of fluorine was found to be a metal with no band gap at Fermi level as depicted in figure 24d, for this reason it is the most favourable structure in terms of electric conductivity out of all the generated structures. Most the structures have band gaps that are larger than the band gap of the parent structure $Li_{1.2}Mn_{0.8}O_2$, and larger than the band gaps of the structures that were obtained from the F-doped $Li_{1.2}Mn_{0.8}O_2$. These findings suggest that having both Ni and F in the $Li_{1.2}Mn_{0.8}O_2$ structure increases the band gap and hence tempers with the electronic conductivity of the structure.

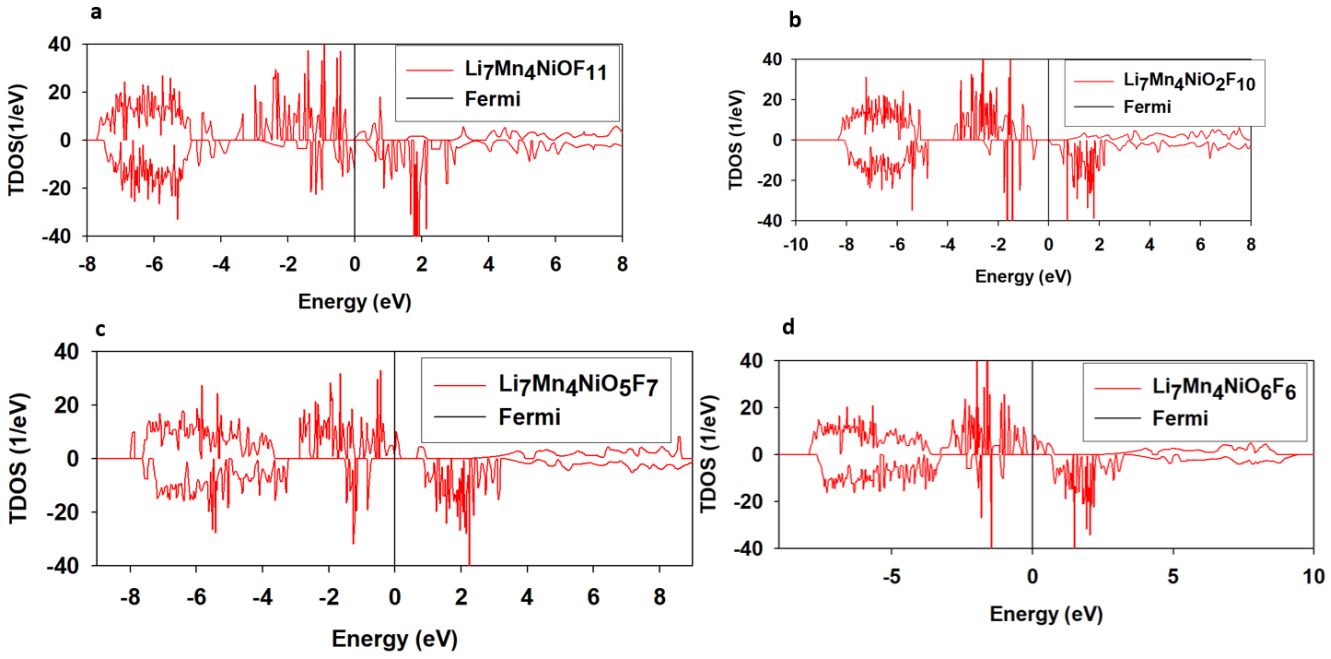

Figure 23: Spin polarized total densities of states of stable phases generated by the F-doped $Li_{1.2}Mn_{0.6}Ni_{0.2}O_2$ cluster expansion.

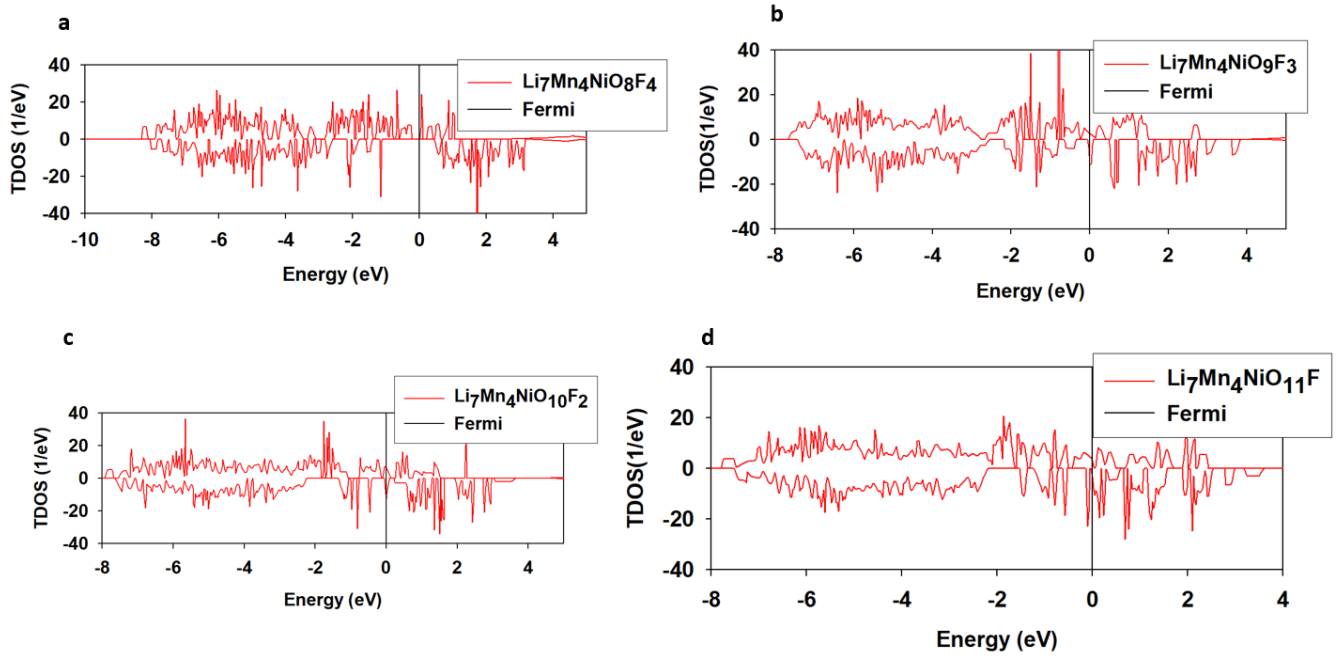

Figure 24: Spin polarized total densities of states of stable phases generated by the F-doped $Li_{1.2}Mn_{0.6}Ni_{0.2}O_2$ cluster expansion.

3.14.2.2 Mechanical properties

To determine the mechanical stability of the generated phases, the elastic constants of the phases were assessed and a strain of 0.001 was used to compute the elastic constants. All the generated phases are triclinic crystals with 21 independent elastic constants and for these phases to be mechanically stable, their elastic constants need to satisfy the mechanical stability criteria of triclinic crystals listed in equations 3.7-1 to 3.7-4.

The structures $Li_{1.2}Mn_{0.6}Ni_{0.2}O_{0.33}F_{1.67}$ and $Li_{1.2}Mn_{0.6}Ni_{0.2}OF$ are mechanically unstable because for $Li_{1.2}Mn_{0.6}Ni_{0.2}O_{0.33}F_{1.67}$ the C_{44} and C_{55} values are less than 0 and for $Li_{1.2}Mn_{0.6}Ni_{0.2}OF$ the C_{66} value is less than 0 and thus violating the criteria that $C_{11}>0$, $C_{22}>0$, $C_{33}>0$, $C_{44}>0$, $C_{55}>0$, and $C_{66}>0$. When incorporating the C_{ij} values listed in table 19 below into equations 3.7-1 to 3.7-4, the conditions are satisfied for all the structures excluding $Li_{1.2}Mn_{0.6}Ni_{0.2}O_{0.33}F_{1.67}$ and $Li_{1.2}Mn_{0.6}Ni_{0.2}OF$ stated above, this suggest that 6 out of the 8 phases are mechanically stable.

The most mechanically stable structure with the highest C_{ij} values is $Li_{1.2}Mn_{0.6}Ni_{0.2}O_{1.83}F_{0.17}$ and the structure with the lowest values and hence the least

stability is $Li_{1.2}Mn_{0.6}Ni_{0.2}OF$. As with the phases generated in F-doped $Li_{1.2}Mn_{0.8}O_2$ when there is an equal amount of fluorine and oxygen the structures tend to be mechanically unstable. On the other hand, when the is less fluorine than oxygen the structures are mechanically stable. This solidifies that only a minimum amount of fluorine is needed for the structure to be mechanically stable.

Table 19: Elastic constants of phases constituting the DFT ground state line of the F-doped $Li_{1.2}Mn_{0.6}Ni_{0.2}O_2$ binary diagram calculated under a strain of 0.001.

Elastic constant C_{ij}	C_{11}	C_{12}	C_{13}	C_{22}	C_{23}	C_{33}	C_{44}	C_{46}	C_{55}	C_{66}
$Li_{1.2}Mn_{0.6}Ni_{0.2}O_{0.17}F_{1.83}$	94.25	34.67	24.05	88.25	28.47	78.48	24.77	-3.32	27.35	26.29
$Li_{1.2}Mn_{0.6}Ni_{0.2}O_{0.33}F_{1.67}$	11.60	37.94	37.67	49.15	12.45	68.20	-2.03	-6.66	-9.58	20.59
$Li_{1.2}Mn_{0.6}Ni_{0.2}O_{0.83}F_{1.17}$	36.95	8.77	30.21	86.88	21.85	84.44	20.51	-9.34	19.05	23.93
$Li_{1.2}Mn_{0.6}Ni_{0.2}OF$	59.60	-28.06	-4.23	17.23	-17.97	66.20	24.90	-10.70	14.31	-3.98
$Li_{1.2}Mn_{0.6}Ni_{0.2}O_{1.33}F_{0.67}$	132.39	19.07	12.46	60.24	5.65	132.16	25.51	-17.97	29.22	42.83
$Li_{1.2}Mn_{0.6}Ni_{0.2}O_{1.5}F_{0.5}$	156.97	59.12	48.49	174.16	43.06	166.23	55.66	-6.81	49.77	64.19
$Li_{1.2}Mn_{0.6}Ni_{0.2}O_{1.67}F_{0.33}$	173.35	48.05	41.21	138.20	31.06	178.15	30.64	-28.80	43.75	52.77
$Li_{1.2}Mn_{0.6}Ni_{0.2}O_{1.83}F_{0.17}$	163.88	77.13	55.80	143.66	50.66	210.95	58.58	-13.71	49.02	64.57

Table 20 below summarises the bulk, shear, Young's modulus, and Pugh's ratio values that were obtained after the elastic moduli of the generated phases were calculated to further study the mechanical stability of these phases.

It was found that the $Li_{1.2}Mn_{0.6}Ni_{0.2}O_{1.83}F_{0.17}$ structure has the highest bulk and Young's values, suggesting that it is the most resistant to compression and the most resistant to elastic deformation. On the other hand, $Li_{1.2}Mn_{0.6}Ni_{0.2}O_{1.5}F_{0.5}$ has the highest shear value implying that it is the most stiff or rigid phase. $Li_{1.2}Mn_{0.6}Ni_{0.2}OF$ has the least compressive strength since it has the lowest bulk modulus value and the phase with the least stiffness and least resistance to elastic deformation is $Li_{1.2}Mn_{0.6}Ni_{0.2}O_{0.33}F_{1.67}$ because it has the lowest shear and Young's values respectively. These results correspond to the elastic constants' results as the structure with equal amount of fluorine and oxygen is unstable and the most stable one has the minimum amount of fluorine. Additionally, the Pugh ratio predicted majority of the materials to be brittle. The ductile materials consist of a high number of fluorine atoms than oxygen atoms, so as the amount of fluorine decreases the

structures move from being ductile to brittle. This suggests that the presence of fluorine atoms in $Li_{1.2}Mn_{0.6}Ni_{0.2}O_2$ enhances the ductility of the material.

Table 20: Elastic moduli of the stable phases constituting the DFT ground state line on the binary diagram of F-doped $Li_{1.2}Mn_{0.6}Ni_{0.2}O_2$ system calculated with an applied strain of 0.001.

Elastic moduli	Bulk (GPa)	Shear (GPa)	Young's (GPa)	Pugh's ratio	Ductility
$Li_{1.2}Mn_{0.6}Ni_{0.2}O_{0.17}F_{1.83}$	48.37	27.27	68.86	1.77	Ductile
$Li_{1.2}Mn_{0.6}Ni_{0.2}O_{0.33}F_{1.67}$	33.90	4.52	12.99	7.49	Ductile
$Li_{1.2}Mn_{0.6}Ni_{0.2}O_{0.83}F_{1.17}$	36.66	22.53	56.09	1.63	Brittle
$Li_{1.2}Mn_{0.6}Ni_{0.2}OF$	4.72	19.93	24.84	0.24	Brittle
$Li_{1.2}Mn_{0.6}Ni_{0.2}O_{1.33}F_{0.67}$	44.35	38.69	89.91	1.15	Brittle
$Li_{1.2}Mn_{0.6}Ni_{0.2}O_{1.5}F_{0.5}$	88.74	57.04	140.92	1.56	Brittle
$Li_{1.2}Mn_{0.6}Ni_{0.2}O_{1.67}F_{0.33}$	81.15	50.06	124.56	1.62	Brittle
$Li_{1.2}Mn_{0.6}Ni_{0.2}O_{1.83}F_{0.17}$	98.41	56.76	142.82	1.73	Brittle

Chapter 4

Cluster Expansion

This chapter details the cluster expansions of the Ni-doped $Li_{1.2}Mn_{0.8}O_2$, F-doped $Li_{1.2}Mn_{0.8}O_2$, F-doped $Li_{1.2}Mn_{0.6}Ni_{0.2}O_2$, and Co-doped $Li_{1.2}Mn_{0.6}Ni_{0.2}O_2$ systems. It further details the iterative progress of these cluster expansions.

4.1. Ni-doped $Li_{1.2}Mn_{0.8}O_2$ cluster expansion

The binary ground state diagram of the Ni-doped $Li_{1.2}Mn_{0.8}O_2$ displayed in figure 25 below, is a plot of the heats of formation against varying concentration of Mn and Ni, this was obtained after the Ni-doped structure was subjected to cluster expansion. A single unit cell was considered for exploring the configuration space and the genetic algorithm detailed in chapter 2.5 was utilised to fit the effective cluster interactions. The fitting scheme ran for a maximum of 20 iterations adding a maximum of 20 structures per iteration and started with an initial training set of 10 structures.

On the binary diagram, cluster expansion predictions are represented by the grey crosses, while the green crosses represent the cluster expansion training set predictions, and the green squares represent the training set of the DFT inputs. The red line is the DFT ground state line and structures that lie on this line are regarded to be the most stable of the generated structures. The y-axis is the energies of formation predicted by the cluster expansion and calculated based on the DFT and the x-axis is the varying concentration of Ni and Mn such that at x=0 there is no Mn and at x=1 there is no Ni, so this variation moves from $Li_7Ni_5O_{12}$ to $Li_7Mn_5O_{12}$. These two structures $Li_7Ni_5O_{12}$ to $Li_7Mn_5O_{12}$ are the parent structures used to conduct the search for new structures.

The cluster expansion generated 12 new phases with negative energies of formation, implying that they are miscible constituents. Of the 12 generated phases, 4 lie on the binary line, out of the 4 phases that lie on the binary line, 2 are the most stable generated phases and the other 2 at x=0 and x=1 are the parent structures. The most stable phase is $Li_7Mn_2Ni_3O_{12}$ ($Li_{1.2}Mn_{0.3}Ni_{0.5}O_2$) at x=0.4 because it has the lowest energy of formation. Although the most stable structure is $Li_{1.2}Mn_{0.3}Ni_{0.5}O_2$ from the cluster expansion, high interest was given to $Li_{1.2}Mn_{0.6}Ni_{0.2}O_2$ which contains the least amount of Ni. Properties

of these structures are discussed in detail in chapter 3, whereafter a comparison of the 2 was made.

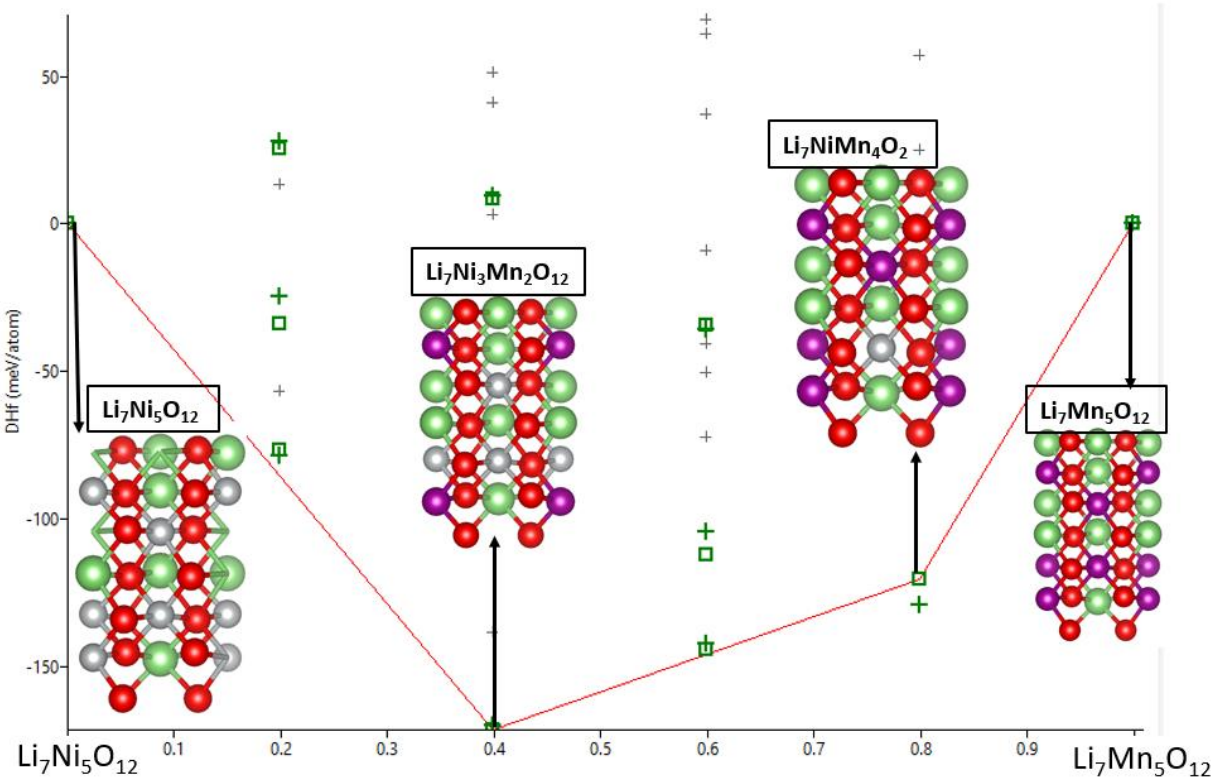

Figure 25: Binary ground state diagram of Ni-doped $Li_{1.2}Mn_{0.8}O_2$ with a CVS of 4.9meV illustrating the most stable generated structures that lie on the DFT ground state line (red line).

Table 21 below is a summary of the iterative optimization progress, giving the number of iterations used to converge the ground state search. It gives the number of new structures, the cross-validation score (CVS) for each iteration which is essential in assessing the reliability of the model since cluster expansion is a stochastic process, and the percentage of structures with standard deviation less than 5 meV.

The second column is a list of new structures produced in each iteration and the third column is the CVS, which gives an indication of whether the cluster expansion was a good one or not. A good cluster expansion is indicated by a CVS of less than 5meV per active position and according to the CVS in table 21, this cluster expansion was a good one since the CVS is 4.9meV/pos which is within the required 5meV/pos. The first 2 structures under column 2 are the parent structures, that is $Li_7Mn_5O_{12}$ and $Li_7Ni_5O_{12}$. 11

new structures were generated in the initial iteration and 1 structure was generated in the second iteration making up a total of 12 new structures.

Table 21: Iterative optimization progress of the Ni-doped $Li_{1.2}Mn_{0.8}O_2$ system, displaying the total number of iterations that converged the system and the CVS.

Iteration	Number of new structures	CVS (meV/pos)	% Structures with SD below 5meV
0	2	-	-
0	11	-	-
1	1	4	-
2	0	4.9	-

4.2 F-doped $Li_{1.2}Mn_{0.8}O_2$ cluster expansion

Figure 26 below is a representation the binary ground state diagram which was obtained after a ground state search of new structures for F-doped $Li_{1.2}Mn_{0.8}O_2$ system, it is a plot of heats of formation against varying concentration of fluorine and oxygen. 4-unit cells were considered for exploring the configuration space and the genetic algorithm detailed in chapter 2.5 was utilised to fit the effective cluster interactions. The fitting scheme ran for a maximum of 20 iterations adding a maximum of 20 structures per iteration and started with an initial training set of 10 structures.

As in figure 25 above, on the binary diagram, the grey crosses represent the cluster expansion predictions, the cluster expansion training set predictions are represented by the green crosses, and green squares represent the training set of the DFT inputs. The red line is the DFT ground state line and the phases that lie on this line are regarded as the most stable of the generated phases.

The y-axis is the energies of formation predicted by the cluster expansion and calculated based on the DFT inputs the x-axis is the varying concentration of F and O. At x=0 there is no oxygen, it is added as we move to the right while the concentration of fluorine decreases from the left to right such that at x=1 there is no fluorine.

The ground state search generated 78 new phases that are miscible constituents since the have negative enthalpies of formation. Of the generated phases, 11 lie on the binary line of the ground state diagram and these are predicted to be the most stable phases. The phase that is predicted to be the most thermodynamically stable phase having the lowest heat of formation is $Li_7Mn_5O_5F_7$ ($Li_{1.2}Mn_{0.8}O_{0.8}F_{1.2}$) which lies at x=0.42 on the binary diagram.

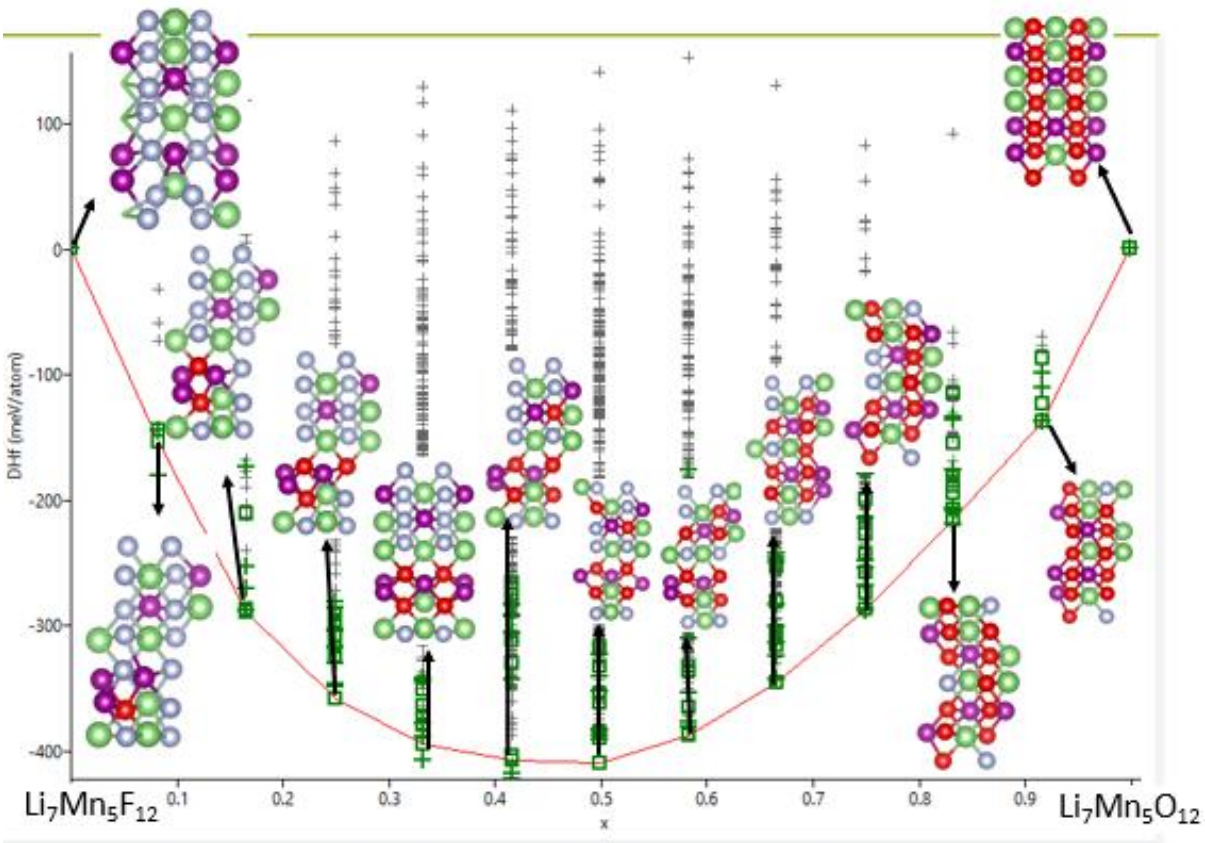

Figure 26: Binary ground state diagram of F-doped $Li_{1.2}Mn_{0.8}O_2$ exhibiting the most stable generated phases on the DFT ground state line, and systems with miscible constituents.

Table 22 below summarises the iterative optimization progress of the ground state search for the F-doped $Li_{1.2}Mn_{0.8}O_2$ system. It shows the number of new structures, the CVS for each iteration, and the percentage of structures with standard deviation below 5meV. The CVS gives accuracy of the predictions, and a good cluster expansion is indicated by CVS less than 5meV and for this for this ground state search the CVS is greater than 5meV implying that the energies where not accurately predicted hence there is a need to

optimize structures before performing further calculations. The column of percentage of structures with standard deviation less than 5meV remained empty and this might be because the genetic algorithm optimization did not use the miscibility gap procedure.

Table 22: Iterative optimization progress for the F-doped $Li_{1.2}Mn_{0.8}O_2$ system, with the number of iterations, CVS and the number of new structures added per iteration.

Iteration.	Number of new structures.	CVS (meV/pos.)	% Structures with SD below 5meV.
0	2	-	-
0	12	-	-
1	10	14	-
2	10	2.7	-
3	10	7.2	-
4	10	19	-
5	8	20	-
6	5	20	-
7	7	22	-
8	6	23	-
9	0	23	-

4.3 F-doped $Li_{1.2}Mn_{0.6}Ni_{0.2}O_2$ cluster expansion

The structure $Li_{1.2}Mn_{0.6}Ni_{0.2}O_2$ was doped with fluorine to investigate the effects of having both Ni and F in the structure $Li_{1.2}Mn_{0.8}O_2$, the doped structure was then subjected to cluster expansion for the generation of new structures. A single unit cell was considered for exploring the configuration space and the genetic algorithm detailed in chapter 2.5 was utilised to fit the effective cluster interactions. The fitting scheme ran for a maximum of 20 iterations adding a maximum of 20 structures per iteration and started with an initial training set of 10 structures.

Figure 27 below is a representation of the binary ground state diagram of fluorine doped $Li_{1.2}Mn_{0.6}Ni_{0.2}O_2$ system, it consists of cluster expansion predictions represented by the grey crosses, the training set cluster expansion predictions represented by the green crosses, the green squares representing the training set DFT inputs and the red line which is the DFT ground state line.

The x-axis consists of varying concentration of F and O, such that at x=0 there is 100% F, and it decreases until x=1 where there is 100% O and 0% F. The two structures $Li_7Mn_4NiF_{12}$ and $Li_7Mn_4NiO_{12}$ positioned at x=0 and x=1 respectively are the parent structure from which the new phases are generated in a genetic algorithm approach The search generated 165 new phases, and out of these 165 new phases 8 lie on the ground state line, these phases that lie on the ground state line are regarded as the stable phases.

The 8 stable phases constituting the ground state line are $Li_{1.2}Mn_{0.6}Ni_{0.2}O_{0.17}F_{1.83}$, $Li_{1.2}Mn_{0.6}Ni_{0.2}O_{0.83}F_{1.17}$, $Li_{1.2}Mn_{0.6}Ni_{0.2}OF$, $Li_{1.2}Mn_{0.6}Ni_{0.2}O_{1.33}F_{0.67}$, $Li_{1.2}Mn_{0.6}Ni_{0.2}O_{1.5}F_{0.5}$, $Li_{1.2}Mn_{0.6}Ni_{0.2}O_{1.67}F_{0.33}$, and $Li_{1.2}Mn_{0.6}Ni_{0.2}O_{1.83}F_{0.17}$, and the structural, mechanical, and electronic properties of these phases are detailed in section 3.15.2.

The cluster expansion generated phases with negative heats of formation implying that the structures are miscible constituents, they are thermodynamically stable and are ordered structures. The most thermodynamically stable structure is $Li_{1.2}Mn_{0.6}Ni_{0.2}O_{0.83}F_{1.17}$ since it has the lowest energy of formation.

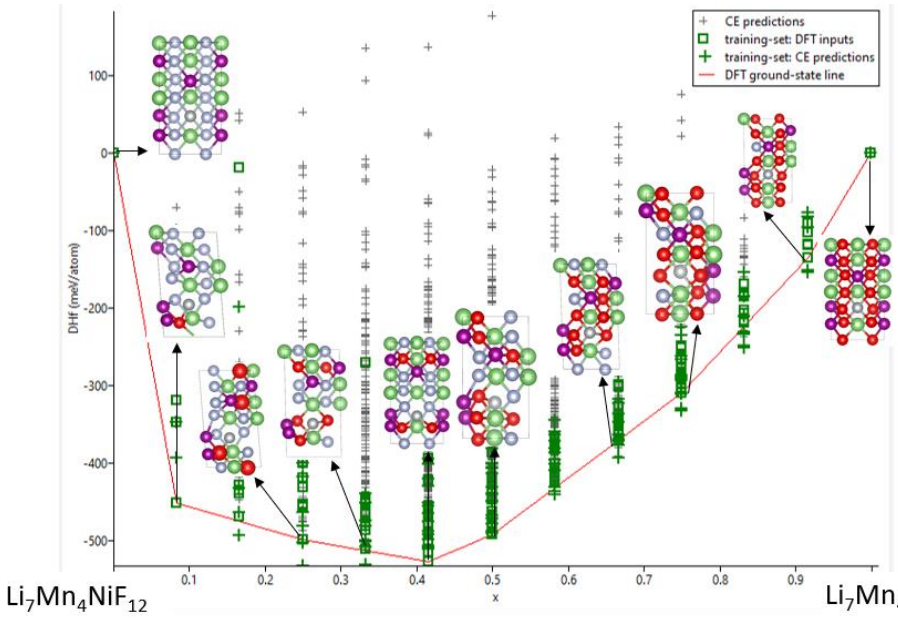

Figure 27: Binary ground state diagram of the F-doped $Li_{1.2}Mn_{0.6}Ni_{0.2}O_2$ with miscible constituents, showing the 9 most stable generated phases that lie on the DFT ground state line.

The iterative procedure of the ground state search for the F-doped $Li_{1.2}Mn_{0.6}Ni_{0.2}O_2$ system is depicted in table 23 below. The table shows the iteration number, number of new structures per iteration, the cross-validation score (CVS), and the percentage of structures with standard deviation below 5meV. The CVS indicates how well the energies of the structures in the training set compare with each other, and a good cluster expansion is indicated by CVS less than 5meV/pos. This cluster expansion had 20 iterations and for all the phases produced, the CVS was found to be 46 which is greater than the required 5meV/pos. this suggests that there are errors in the predicted energies. The column with percentage of structures with standard deviation less than 5meV remained empty and this is because the genetic algorithm optimization did not use the miscibility gap procedure.

Table 23: Iterative optimization progress of the F-doped $Li_{1.2}Mn_{0.6}Ni_{0.2}O_2$ system, showing the number of iterations used to converge the cluster expansion, the number of structures added per iteration and the CVS of the system.

Iteration.	Number of new structures.	CVS (meV/pos.)	% Structures with SD below 5meV.
0	2	-	-
0	22	-	-
1	10	3	-
2	10	1.7	-
3	10	14	-
4	10	32	-
5	10	47	-
6	9	50	-
7	10	52	-
8	9	51	-
9	8	54	-
10	8	55	-
11	6	49	-
12	6	51	-
13	7	52	-
14	7	52	-
15	3	51	-
16	7	47	-
17	6	47	-
18	2	47	-
19	5	48	-
20	0	46	-

4.4 Co-doped $Li_{1.2}Mn_{0.6}Ni_{0.2}O_2$ cluster expansion

The $Li_{1.2}Mn_{0.6}Ni_{0.2}O_2$ structure was doped with cobalt on one manganese position to determine whether the presence of cobalt will improve the mechanical stability of the

material. Once doped with Co on one Mn site, a ground state search for new structures was done to generate new structures of the Co-doped $Li_{1.2}Mn_{0.6}Ni_{0.2}O_2$. A single unit cell was considered for exploring the configuration space and the genetic algorithm detailed in chapter 2.5 was utilised to fit the effective cluster interactions. The fitting scheme ran for a maximum of 20 iterations, adding a maximum of 20 structures per iteration and started with an initial training set of 10 structures.

The obtained binary diagram for this system is depicted in Figure 28 below, as in the other binary diagrams, this is a plot of the heats of formation against varying concentration of Co and Mn. On the diagram, the grey crosses represent the cluster expansion predictions, the cluster expansion training set predictions are represented by the green crosses, and green squares represent the training set of the DFT inputs. The red line is the DFT ground state line and the phases that lie on this line are regarded as the most stable of the generated phases.

This ground state search generated a total of 48 new phases, and of the 48 phases, 6 lie on the ground state line with 2 (at x=0 and x=1) being the parent structures and 4 being the most stable of the generated phases. Out of these 4 structures, the structure with the lowest heat of formation is $Li_{1.2}Mn_{0.5}Co_{0.11}Ni_{0.17}O_2$ suggesting that it is the most thermodynamically stable structure out of all the 48 generated phases.

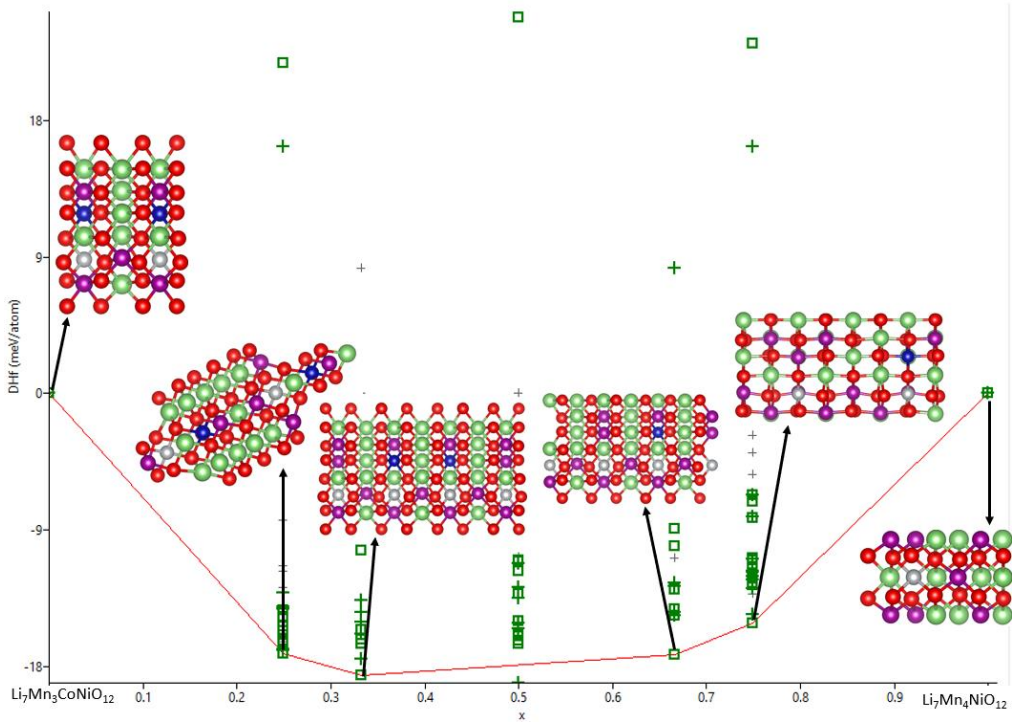

Figure 28: Binary ground state diagram of Co-doped $Li_{1.2}Mn_{0.6}Ni_{0.2}O_2$ system, displaying the 4 most stable generated phases that lie on the DFT ground state line.

Table 24 shows the iterative optimisation progress of the ground state search for the Co-doped $Li_{1.2}Mn_{0.6}Ni_{0.2}O_2$ system. It displays the number of iterations along with the number of new structures, the CVS, and percentage of structures with standard deviation less than 5meV. The CVS of the generated structures is within 5meV/pos. This suggests that the structures were accurately predicted by the cluster expansion. The column of percentage of structures with standard deviation less than 5meV remained empty for all iterations meaning that the genetic algorithm optimisation did not use the miscibility gap procedure.

Table 24: Iterative optimization progress of the Co-doped $Li_{1.2}Mn_{0.6}Ni_{0.2}O_2$ system giving the number of iterations, new structures, and the CVS of the system.

Iteration.	Number of new structures.	CVS (meV/pos.)	% structures with SD below 5meV.
0	0	-	-
0	0	-	-
1	12	1.7	-
2	17	0.18	-
3	22	0.65	-
4	27	0.3	-
5	30	0.98	-
6	35	0.91	-
7	37	5.1	-
8	40	4.5	-
9	43	2.6	-
10	46	3.5	-
11	48	5.5	-

Chapter 5

Experimental results.

5.1 Tapped density.

Tapped density is the density obtained after mechanically tapping a container containing the powder sample, it is also referred to as an increased density of a powder sample. Tapped density is different from bulk density in that the bulk density includes the contribution of the interparticle void volume whereas in tapped density the void volume is minimised.

$Li_{1.2}Mn_{0.8}O_2$

The tapped density of the sample was obtained by tapping the sample in a graduated cylinder for 1500 times at a position of 14mm and 300 taps per minute. The obtained volumes are shown in the calculations below where initial volume is the volume of the sample before tapping and the final volume is the volume of the sample after it had been tapped.

Sample weight= 30g

Initial volume=24cm^3

Final volume=19cm^3

Bulk density= $\frac{m}{v} = \frac{30g}{24cm^3} = 1.25g/cm^3$

Tapped density= $\frac{m}{v} = \frac{30g}{19cm^3} = 1.58g/cm^3$

$Li_{1.2}Mn_{0.6}Ni_{0.2}O_2$

The final volume of the sample is less than the initial volume of the sample as indicated in the calculations below, and this is an indication that the sample was successfully tapped.

Sample weight= 30g

Initial volume=24cm^3

Final volume=21cm^3

Bulk density= $\frac{m}{v} = \frac{30g}{24cm^3} = 1.25g/cm^3$

Tapped density= $\frac{m}{v} = \frac{30g}{21cm^3} = 1.43g/cm^3$

The obtained tap density is in good agreement with the one reported by Wang et, al., which is 1.73g/cm^3 obtained using the carbonate co-precipitation method [115].

$Li_{1.2}Mn_{0.4}Ni_{0.2}Co_{0.2}O_2$

The sample was tapped in a graduated cylinder 1500 times at a position of 14mm and 300 taps per minute. According to the obtained tapped density, the sample $Li_{1.2}Mn_{0.4}Ni_{0.2}Co_{0.2}O_2$ is the less dense material compared to the $Li_{1.2}Mn_{0.8}O_2$ and $Li_{1.2}Mn_{0.6}Ni_{0.2}O_2$ materials.

Sample weight= 30g

Initial volume=36cm^3

Final volume=27cm^3

Bulk density=$\frac{m}{v} = \frac{30g}{36cm^3} = 0.83g/cm^3$

Tapped density=$\frac{m}{v} = \frac{30g}{27cm^3} = 1.11g/cm^3$

5.2 XRF analyses

$Li_{1.2}Mn_{0.4}Ni_{0.2}Co_{0.2}O_2$

XRF analysis was performed to quantify the metals in the synthesized materials. Table 25 below shows the XRF results of the $Li_{1.2}Mn_{0.4}Ni_{0.2}Co_{0.2}O_2$ material. When performing the analysis, 8.66g of the precursor sample powder was mixed with 2.47g of a binding pill making up a powder with total mas of 11.1g. This implies that of the sample that was loaded into the XRF machine 78% was the precursor sample and 22% was the binding pill. The metal content amounted to 69%, the other 9% can be accounted for by the Li and O atoms in the material.

To determine the NMC ratio of the product, the following conversions were made. Firstly, the percentage compositions of the Ni, Mn, and Co elements were converted to mass compositions, thereafter the grams were converted to mols from which the ratios were determined.

Percentage compositions to mass compositions.

$$\frac{33.544\%Mn}{100} \times 11.1g = 3.72g\ of\ Mn$$

$$\frac{19.037\%Co}{100} \times 11.1g = 2.11g\ of\ Co$$

$$\frac{16.901\%Ni}{100} \times 11.1g = 1.876g\ of\ Ni$$

Masses to moles

$$3.72g\ Mn \times \frac{1mol\ Mn}{\frac{54.938g}{mol}} = 0.068mol\ Mn$$

$$2.11g\ Co \times \frac{1mol\ Co}{\frac{58.933g}{mol}} = 0.036mol\ Co$$

$$1.876g\ Ni \times \frac{1mol\ Ni}{\frac{58.693g}{mol}} = 0.032mol\ Ni$$

From the calculations, the ratio of Ni: Mn: Co is 1:2:1. The expected ratio was 2:4:2 and from the one obtained it is evident that the Metal content is much less than what was expected. This might suggest that the metals were lost with the waste product when filtering the final synthesis product.

Table 25: XFR analysis of the $Li_{1.2}Mn_{0.4}Ni_{0.2}Co_{0.2}O_2$ material.

Atom	Content (%)
Mn	33.544
Co	19.037
Ni	16.901

$Li_{1.2}Mn_{0.6}Ni_{0.2}O_2$

The XRF result of the material $Li_{1.2}Mn_{0.6}Ni_{0.2}O_2$ are shown in table 26 below. 8.89g of the material was mixed with 2.86g of the binding pill amounting to 11.75g of the sample that was loaded to the XRF machine. For the sample that was loaded for analysis, 75.66% is the material composition and 24.34% is the binding pill composition. The total of the metal content obtained is 64.92%, implying that 10.74% might consist of the Li and O elements, or compounds that are not within the detection limits of the XRF instrument. The obtained Mn: Ni ratio as found to be 3:1 as shown in the calculation below.

Percentage compositions to mass compositions.

$$\frac{48.635\%Mn}{100} \times 11.750g = 5.706g\ of\ Mn$$

$$\frac{16.187\%Ni}{100} \times 11.750g = 1.899g\ of\ Ni$$

Masses to moles

$$5.706g\ Mn \times \frac{1mol\ Mn}{\frac{54.938g}{mol}} = 0.104mol\ Mn$$

$$1.899g\ Ni \times \frac{1mol\ Ni}{\frac{58.693g}{mol}} = 0.032mol\ Ni$$

Table 26: XRF results of the $Li_{1.2}Mn_{0.6}Ni_{0.2}O_2$ material.

Atom	Content (%)
Mn	48.635
Ni	16.187

$Li_{1.2}Mn_{0.8}O_2$

With the $Li_{1.2}Mn_{0.8}O_2$ material, the only metal expected to be in the material is Mn. However, according to the XRF results tabulated in table 27 below, there is a very small amount of Ni and Co that was detected, this Ni and Co present in the material might be a result of contamination during the synthesis and analysis process. 8.81g of the material plus 2.839g of the binding pill amounting to 11.613g of the sample was analysed suggesting that 75.86% of the sample consisted of the material $Li_{1.2}Mn_{0.8}O_2$ and 24.14% consisted of the binding pill. The total of the metal content detected by the XRF machine amounted to 61.13%, the remaining 14.73% to make up the total of the material analysed can be accounted for by the Li and O elements that were not detected by the XRF machine.

Table 27: XRF results of the $Li_{1.2}Mn_{0.8}O_2$ material.

Atom	Content (%)
Mn	60.746
Co	0.152
Ni	0.230

5.3 SEM analyses

Scanning electron microscopy was performed on the samples to study the morphology of the synthesized materials.

Figure 29 below is a representation of the SEM image of $Li_{1.2}Mn_{0.6}Ni_{0.2}O_2$ material. The material has primary particles with irregular shapes. The agglomeration of primary particles forms secondary particles with spherical shapes. The primary particles are 2µm in size and the secondary particles are about 10µm. The advantage of spherical particles is that they allow high packing density which is crucial for practical applications [116]. The irregular primary particle shapes and spherical shapes of the secondary particles is also observed in reference work shown in figure 29 b. There are large empty spaces between the particles, and this is in good agreement with what was found in literature as depicted in figure 30 below. The analysis further showed that the secondary particles have a porous nature, which can also be seen in the sample images from literature in figure 30.

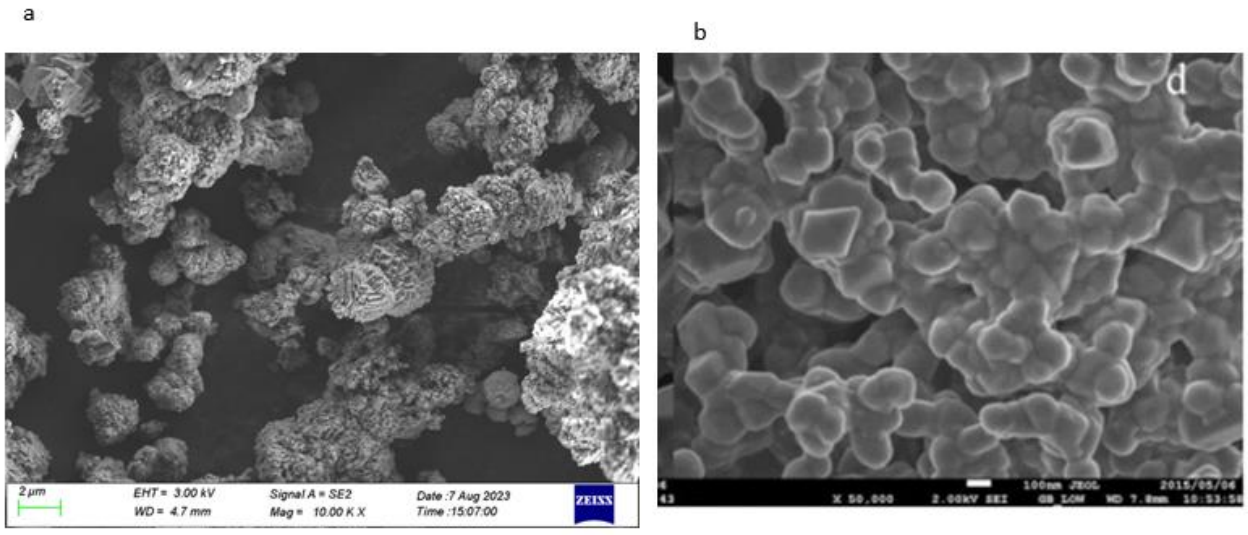

Figure 29: SEM images of the $Li_{1.2}Mn_{0.6}Ni_{0.2}O_2$ material from this work (a) and reference *[29]* **work (b) taken with 10000X and 50000X magnification respectively.**

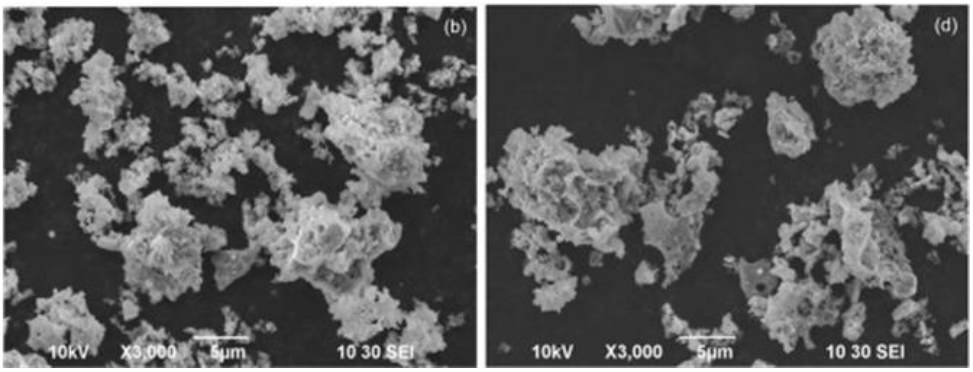

Figure 30: SEM images of $Li_{1.2}Mn_{0.6}Ni_{0.2}O_2$ at 3000X magnification *[117]*.

The SEM images of the $Li_{1.2}Mn_{0.8}O_2$ material are shown in figure 31 below. The SEM analysis showed that the material is composed of spherical particles that are scattered. These particles are about 8.232μm in size. The particles' spherical shapes are well defined as compared to those of the $Li_{1.2}Mn_{0.6}Ni_{0.2}O_2$ and $Li_{1.2}Mn_{0.4}Ni_{0.2}Co_{0.2}O_2$ materials. This suggests that the co-precipitation technique is well suited for the synthesis of the layered $Li_{1.2}Mn_{0.8}O_2$ material. There is less agglomeration of primary particles in the $Li_{1.2}Mn_{0.8}O_2$ material unlike in the $Li_{1.2}Mn_{0.6}Ni_{0.2}O_2$ material.

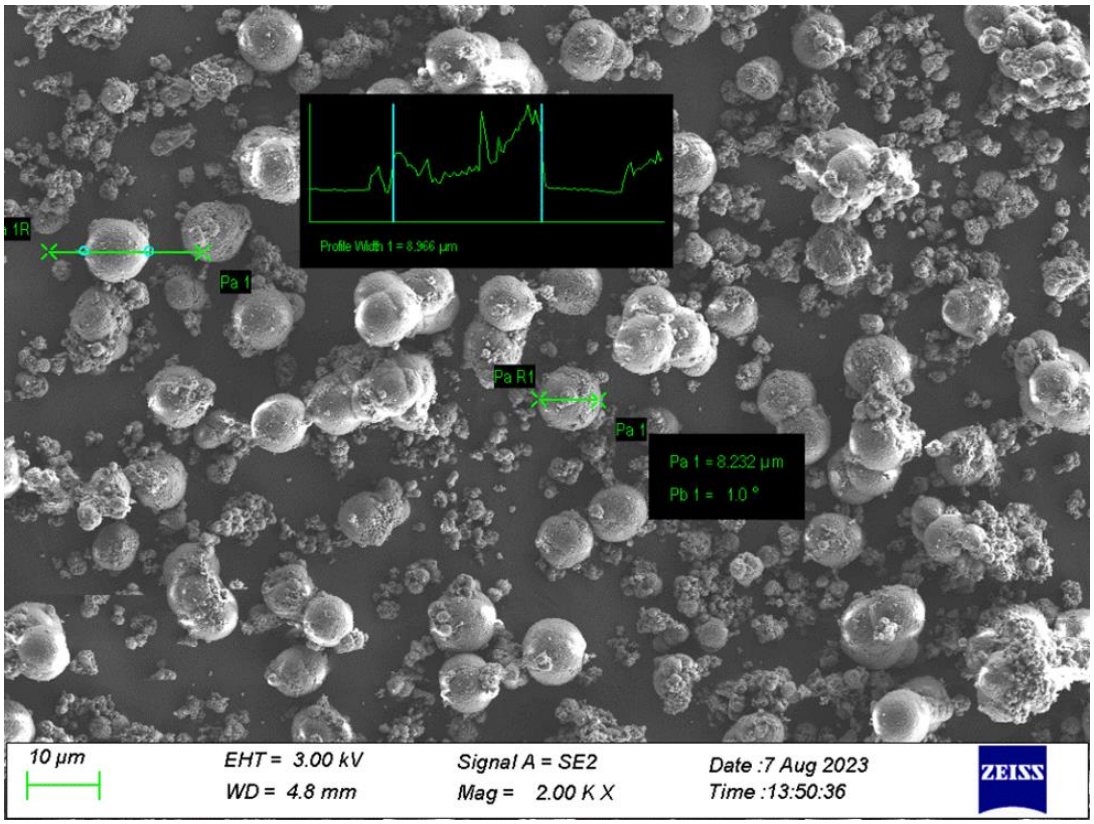

Figure 31: SEM image of the $Li_{1.2}Mn_{0.8}O_2$ structure at 1000X magnification.

The SEM analysis of the $Li_{1.2}Mn_{0.4}Ni_{0.2}Co_{0.2}O_2$ as depicted in figure 32 below showed that the material is made up of spherical primary particles. These primary particles bind together forming secondary particles that are also spherical in shape. This material has empty spaces in between the particles. From the 3 samples $Li_{1.2}Mn_{0.6}Ni_{0.2}O_2$, $Li_{1.2}Mn_{0.8}O_2$, and $Li_{1.2}Mn_{0.4}Ni_{0.2}Co_{0.2}O_2$ morphologies, it is evident that the co-precipitation method with the semi-batch technique can produce materials with spherical particles.

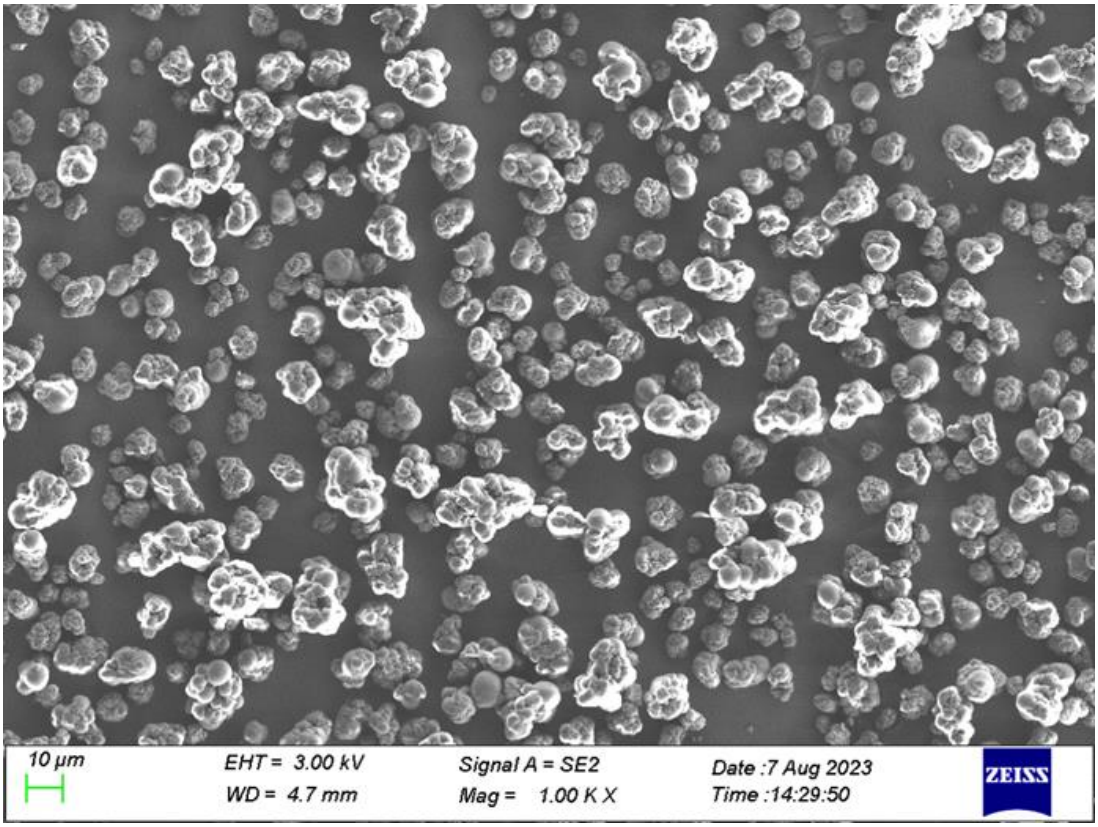

Figure 32: SEM images of the $Li_{1.2}Mn_{0.4}Ni_{0.2}Co_{0.2}O_2$ at (a) 1000X magnification and (b) 6000X magnification.

5.4 Particle size distribution

$Li_{1.2}Mn_{0.6}Ni_{0.2}O_2$

Particle size analysis was performed on the $Li_{1.2}Mn_{0.6}Ni_{0.2}O_2$ cathode material using the wet method analysis to study the particle sizes and how they are distributed within the material, and the results are shown in figure 33 below. Particle size distribution shows percentage of particles with a specific size. The analysis showed that 10% of the smallest particles have diameters less than 14.29µm i.e., D10=14.29µm. The central point of the distribution is D50=22.95µm. This suggests that the half of the particles have diameters

smaller than 22.95µm and half of them have diameters larger than 22.95µm. The largest particle size is 33.16µm i.e., D90=33.16µm. Small particles are essential in cathode materials for LIBs as they imply a larger specific surface area enabling a large portion of the active material to take part in the electrochemical reaction [118].

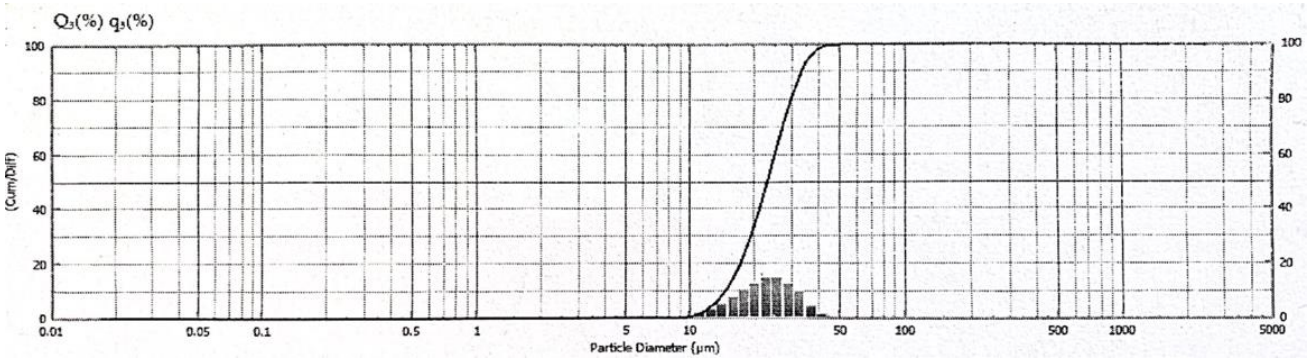

Figure 33: Particle size distribution of the $Li_{1.2}Mn_{0.6}Ni_{0.2}O_2$ material.

Chapter 6

Conclusion

First-principles calculations were systematically performed to study properties of the $Li_{1.2}Mn_{0.8}O_2$ material. For starters, structural, electronic, and mechanical properties of the $Li_{1.2}Mn_{0.8}O_2$ structure were studied alongside those of Li_2MnO_3 for comparison. Both materials exhibit negative energy of formation which suggested that they are thermodynamically stable, additionally, $Li_{1.2}Mn_{0.8}O_2$ was found to have a more negative heat of formation than Li_2MnO_3 implying that $Li_{1.2}Mn_{0.8}O_2$ is more thermodynamically stable than Li_2MnO_3. The density of states calculations showed that $Li_{1.2}Mn_{0.8}O_2$ is more favourable in terms of electric conductivity as it was found to be a semi-conductor with a band gap of 0.269eV which is less than 1.888eV of the Li_2MnO_3. Elastic constants were considered to deduce the mechanical stability of the materials under strains 0.001, 0.005, and 0.025. Li_2MnO_3 was found to be mechanically stable under all strains. On the other hand, $Li_{1.2}Mn_{0.8}O_2$ is only mechanically stable under strain 0.001. Furthermore, the Pugh ratio predicted Li_2MnO_3 brittle under all 3 strains while $Li_{1.2}Mn_{0.8}O_2$ was predicted to be brittle under strain 0.001 and ductile under 0.005 and 0.025.

$Li_{1.2}Mn_{0.8}O_2$ was doped with Ni on the Mn site and subjected to cluster expansion. The cluster expansion successfully generated new phases of the Ni-doped structure. $Li_{1.2}Mn_{0.6}Ni_{0.2}O_2$ and $Li_{1.2}Mn_{0.3}Ni_{0.5}O_2$ were the most stable generated phases that lie on the binary DFT ground state line. These structures were found to be thermodynamically stable. Their densities of states showed great improvement in conductivity as they both do not have band gaps at the Fermi level. The obtained elastic constants for $Li_{1.2}Mn_{0.6}Ni_{0.2}O_2$ and $Li_{1.2}Mn_{0.3}Ni_{0.5}O_2$ satisfied the mechanical stability criteria for triclinic crystals implying that they are mechanically stable. However, the Pugh ratio suggested that the materials are brittle. These results suggest that the presence of Ni in the $Li_{1.2}Mn_{0.8}O_2$ structure maintains the thermodynamic stability of the structure, improves the electronic conductivity of the structure, and maintain the mechanical stability of the structure but compromises the ductility of the structure.

The $Li_{1.2}Mn_{0.8}O_2$ structure was fluorinated by doping the O sites with F. Adding fluorine to the layered $Li_{1.2}Mn_{0.8}O_2$ structure enhances the thermal stability of the structure with the

most stable structure being $Li_{1.2}Mn_{0.8}O_{0.17}F_{1.83}$ containing 91.5% F and 8.5% O. The presence of fluorine in $Li_{1.2}Mn_{0.8}O_2$ shows an improvement in electric conductivity because some of the generated phases have no band gaps and some have band gaps less than that of the pristine $Li_{1.2}Mn_{0.8}O_2$. From the elastic constants of the generated phases, it was found that the mechanically stable phases are those with less F atoms than O atoms. The most mechanically stable phase is $Li_{1.2}Mn_{0.8}O_{1.83}F_{0.17}$ which contains 91.5% O and 8.5%F.

$Li_{1.2}Mn_{0.6}Ni_{0.2}O_2$ was also fluorinated by doping the O sites with F. Phases generated by the cluster expansion of this system are thermodynamically stable with negative heats of formation. The density of states of the phases showed that some of the generated phases are semi-conductors and some are magnetic metals. The generated phases were found to be mechanically stable with the exception of the phase that contained an equal amount of F and O atoms i.e., $Li_{1.2}Mn_{0.6}Ni_{0.2}OF$. The most mechanically stable phase is $Li_{1.2}Mn_{0.6}Ni_{0.2}O_{1.83}F0._{17}$.

From the two fluorinated systems, it can be concluded that the presence of fluorine in the materials enhances the thermodynamic stability of the materials. It retains the electric conductivity of the materials. The presence of fluorine has potential to improve the mechanical stability of these materials. it can also be concluded that a minimum amount of fluorine is required for the materials to be mechanically stable.

The co-precipitation reaction using semi-batch synthesis method was used to synthesize the $Li_{1.2}Mn_{0.8}O_2$, $Li_{1.2}Mn_{0.6}Ni_{0.2}O_2$, and $Li_{1.2}Mn_{0.4}Ni_{0.2}Co_{0.2}O_2$ materials. This method successfully produced materials with spherical particles. XRF analysis of the $Li_{1.2}Mn_{0.4}Ni_{0.2}Co_{0.2}O_2$ showed that the metal content in the synthesized product is less than the expected content. The $Li_{1.2}Mn_{0.6}Ni_{0.2}O_2$ material was found to have a tapped density of 1.43g/cm^3 which agrees well with what has been reported. Particle size distribution showed that the particles within the $Li_{1.2}Mn_{0.6}Ni_{0.2}O_2$ material are distributed in such a way that D10=14.29µm, D50=22.95µm, and D90=33.16µm.

This work has successfully generated new cathode materials with better structural, mechanical, and electronic properties. Furthermore, the experimental synthesis method was able to achieve the desired particles for Li-rich Mn-based layered oxide cathode materials.

References

[1] Wei Luo, Siling Cheng, Meng Wu, Xianghua Zhang, Dan Yang, Xianhong Rui, “A review of advanced separators for rechargeable batteries,” *Journal of Power Sources,* vol. 509, 2021.

[2] Zhangxian Chen and Weixin Zhang and Zeheng Yang, “A review on cathode materials for advanced lithium ion batteries: microstructure designs and performance regulations,” *Nanotechnology,* vol. 31, p. 012001, 2019.

[3] Gong, Zhengliang and Yang, Yong, “Recent advances in the research of polyanion-type cathode materials for Li-ion batteries,” *Energy Environ. Sci,* vol. 4, no. 9, pp. 3223-3242, 2011.

[4] Xu Terrence, Wang Wei, Gordin Mikhail L.,Wang Donghai,Choi Daiwon, “Lithium-ion batteries for stationary energy storage,” *Energy Storage Technologies,* vol. 62, no. 9, 2010.

[5] Yameng Fan, Wenchao Zhang, Yunlong Zhao, Zaiping Guo, Qiong Cai, “Fundamental understanding and practical challenges of lithium-rich oxide cathode materials: Layered and disordered-rocksalt structure,” *Energy Storage Materials,* vol. 50, pp. 51-71, 2021.

[6] Juyan Zhang, Xuhui Yao, Ravi K. Misra, Qiong Cai, Yunlong Zhao, “Progress in electrolytes for beyond-lithium-ion batteries,” *Journal of Materials Science & Technology,* vol. 44, pp. 237-257, 2020.

[7] K. Mizushima, P.C. Jones, P.J. Wiseman, J.B. Goodenough, “Li_xCoO_2 ($0<x<-1$): A new cathode material for batteries of high energy density,” *Materials Research Bulletin,* vol. 15, no. 6, pp. 783-789, 1980.

[8] Shuoqing Zhao, Ziqi Guo, Kang Yan, Shuwei Wan, Fengrong He, Bing Sun, Guoxiu Wang, “Towards high-energy-density lithium-ion batteries: Strategies for developing high-capacity lithium-rich cathode materials,” *Energy Storage Materials,* vol. 34, pp. 716-734, 202.

[9] Gurbinder Kaur and Byron D. Gates, “Review—Surface Coatings for Cathodes in Lithium Ion Batteries: From Crystal Structures to Electrochemical Performance,” *Journal of The Electrochemical Society,* vol. 169, no. 4, p. 043504, 2022.

[10] Zhang, Hanlei and May, Brian M. and Omenya, Fredrick and Whittingham, M. Stanley and Cabana, Jordi and Zhou, Guangwen, “Layered Oxide Cathodes for Li-Ion Batteries: Oxygen Loss and Vacancy Evolution,” *Chemistry of Materials,* vol. 31, no. 18, pp. 7790-7798, 2019.

[11] Jason R. Croy, Kevin G. Gallagher, Mahalingam Balasubramanian, Brandon R. Long and Michael M. Thackeray, “Quantifying Hysteresis and Voltage Fade in $xLi_2MnO_3(1-x)LiMn_{0.5}Ni_{0.5}O_2$ Electrodes as a Function of Li_2MnO_3 Content,” *Journal of The Electrochemical Society,* vol. 161, pp. 318-325, 2013.

[12] Fan, Jianming and Li, Guangshe and Li, Baoyun and Zhang, Dan and Chen, Dandan and Li, Liping, “Reconstructing the Surface Structure of Li-Rich Cathodes for High-Energy Lithium-Ion Batteries,” *ACS Applied Materials \& Interfaces,* vol. 11, no. 22, pp. 19950-19958, 2019.

[13] M.M. Thackeray, W.I.F. David, P.G. Bruce, J.B. Goodenough, “Lithium insertion into manganese spinels,” *Materials Research Bulletin,* vol. 18, no. 4, pp. 461-472, 1983.

[14] Yiqi Cui, Chengyi Zhu, Rui Huang, Jiaming Liu, Yannan Zhang, “Improved Electrochemical Cyclic Performances of Spinel $LiMn_2O_4$ by Coating with Lanthanum Phosphate,” *International Journal of Electrochemical Science,* vol. 15, no. 6, pp. 5440-5448, 2020.

[15] Shan Wang, Shijie Jiang, Yunjiao Li, Zhouliang Tan, Shuaipeng Hao, Jiachao Yang, Zhengjiang He, “Interface dual-engineering strategy boosting the excellent high-temperature electrochemical properties of $LiMn_2O_4$,” *Journal of Power Sources,* vol. 579, p. 233292, 2023.

[16] Goodenough, John B. and Park, Kyu-Sung, “The Li-Ion Rechargeable Battery: A Perspective,” *Journal of the American Chemical Society,* vol. 135, no. 4, pp. 1167-1176, 2013.

[17] Goodenough, John B. and Kim, Youngsik, “Challenges for Rechargeable Li Batteries,” *Chemistry of Materials,* vol. 22, no. 3, pp. 587-603, 2010.

[18] Zhi-Liang Wu, Hanjie Xie, Yingzi Li, Fangchang Zhang, Zhenyu Wang, Wei Zheng, Mingyang Yang, Zhenghe Xu, Zhouguang Lu, “$Li_{1.2}Ni_{0.25}Mn_{0.55}O_2$: A high-capacity cathode material with a homogeneous monoclinic Li_2MnO_3-like superstructure,” *Journal of Alloys and Compounds,* vol. 827, 2020.

[19] Ya Sun, Minghui Guo, Siwei Shu, Deng Ding, Chunlei Wang, Youxiang Zhang, Juntao Yan, “Preparation of Li_2MnO_3 nanowires with structural defects as high rate and high capacity cathodes for lithium-ion batteries,” *Applied Surface Science,* vol. 585, 2022.

[20] Sathiya, M. and Ramesha, K. and Rousse, G. and Foix, D. and Gonbeau, D. and Prakash, A. S. and Doublet, M. L. and Hemalatha, K. and Tarascon, J.-M, “High Performance $Li_2Ru_{1-y}Mn_yO_3$ ($0.2 \leq y \leq 0.8$) Cathode Materials for Rechargeable Lithium-Ion Batteries: Their understanding,” *Chemistry of Materials,* vol. 25, no. 7, pp. 1121-1131, 2013.

[21] Croy, Jason R. and Park, Joong Sun and Dogan, Fulya and Johnson, Christopher S. and Key, Baris and Balasubramanian, Mahalingam, “First-Cycle Evolution of Local Structure in Electrochemically Activated Li_2MnO_3,” *Chemistry of Materials,* vol. 26, pp. 7091-7098, 2014.

[22] Sun-Ho Kang, Michael M. Thackeray, “Enhancing the rate capability of high capacity $xLi_2MnO_3{\cdot}(1-x)LiMO_2$ (M=Mn, Ni, Co) electrodes by Li–Ni–PO_4 treatment,” *Electrochemistry Communications ,* vol. 11, no. 4, pp. 748-751, 2009.

[23] Z.Q. Wang, M.S. Wu, B. Xu, C.Y. Ouyang, “Improving the electrical conductivity and structural stability of the Li_2MnO_3 cathode via P doping,” *Journal of Alloys and Compounds,* vol. 65, pp. 818-823, 2016.

[24] Yujuan Zhao, Minghua Xia, Xinsa Hu, Zongkui Zhao, Yang Wang, Zhi Lv, “Effects of Sn doping on the structural and electrochemical properties of $Li_{1.2}Ni_{0.2}Mn_{0.8}O_2$ Li-rich cathode materials,” *Electrochimica Acta,* vol. 17, pp. 1167-1174, 2015.

[25] Sun-Mi Kim, Sae-A Lee, Bo-Young Kim, Sun-Sik Bae, Seong-Kug Eo, Koanhoi Kim, “Hydroxycholesterol induces recruitment of monocytic cells by enhancing

CCL2 production," *Biochemical and Biophysical Research Communications,* vol. 442, pp. 159-164, 2013.

[26] Chong, Shaokun & Liu, You-Ning & Yan, Wuwei & Chen, Yuanzhen., "Chong, Shaokun & Liu, You-Ning & Yan, "Effect of valence states of Ni and Mn on the structural and electrochemical properties of $Li_{1.2}Ni_xMn_{0.8-x}O_2$ cathode materials for lithium-ion batteries," *Royal Society of Chemistry,* vol. 6, 2016.

[27] Mengchu Yang, Bei Hu, Fushan Geng, Chao Li, Xiaobing Lou, Bingwen Hu, "Mitigating voltage decay in high-capacity $Li_{1.2}Ni_{0.2}Mn_{0.6}O_2$ cathode material by surface K+ doping," *Electrochimica Acta,* vol. 291, pp. 278-286, 2018.

[28] Santhanamoorthi Nachimuthu, Han-Wen Huang, Kuan-Yu Lin, Ching Yu, Jyh-Chiang Jiang, "Direct visualization of lattice oxygen evolution and related electronic properties of $Li_{1.2}Ni_{0.2}Mn_{0.6}O_2$ cathode materials," *Applied Surface Science,* vol. 563, p. 150334, 2021.

[29] Nomasonto Rapulenyane, Ernst Ferg, Hongze Luo, "High-performance $Li_{1.2}Mn_{0.6}Ni_{0.2}O_2$ cathode materials prepared through a facile one-pot co-precipitation process for lithium ion batteries," *Journal of Alloys and Compounds,* vol. 762, pp. 272-281, 2018.

[30] Xuwang Hou, Yong Wang, Jinhua Song, Haitao Gu, Rui Guo, Wen Liu, Ya Mao, Jingying Xie., "Electrochemical behavior of Mn-based Li-rich cathode material $Li_{1.15}Ni_{0.17}Co_{0.11}Mn_{0.57}O_2$ fluorinated by NH4F,," *Solid State Ionics,* vol. 325, pp. 1-6, 2018.

[31] L. Li, B.H. Song, Y.L. Chang, H. Xia, J.R. Yang, K.S. Lee, L. Lu, "Retarded phase transition by fluorine doping in Li-rich layered $Li_{1.2}Mn_{0.54}Ni_{0.13}Co_{0.13}O_2$ cathode material," *Journal of Power Sources,* vol. 283, pp. 162-170, 2015.

[32] Jay Hyok Song, Andrei Kapylou, Hee Sung Choi, Byong Yong Yu, Evegeniya Matulevich, Sun Ho Kang, "Suppression of irreversible capacity loss in Li-rich layered oxide by fluorine doping," *Journal of Power Sources,* vol. 313, pp. 65-72, 2016.

[33] Zhihao Guo, Lin Li, Zihao Su, Gongchang Peng, Meizhen Qu, Yuanxiang Fu, Hao Wang, Wujie Ge, "Enhancing cyclic performance of lithium-rich manganese-based

cathode via in-situ co-doping of magnesium and fluorine," *Electrochimica Acta,* vol. 437, p. 141525, 2023.

[34] Ngoc Hung Vu, Hai-Linh Thi Dang, Hong-Ha Thi Vu, Phan Thi Dien, Dang Viet Cuong, Vu Tue Anh, Do Thi Lien, Tran Van Tan, Nang Xuan Ho, Van-Duong Dao, "Ti- and F- co-doped $Li_{1.2}Mn_{0.75}Ni_{0.25}O_2$ as efficient cathode materials for Li-ion batteries," *Journal of Energy Storage,* vol. 72, p. 108251, 2023.

[35] Ya Sun, Minghui Guo, Siwei Shu, Deng Ding, Chunlei Wang, Youxiang Zhang, Juntao Yan, "Preparation of Li_2MnO_3 nanowires with structural defects as high rate and high capacity cathodes for lithium-ion batteries," *Applied Surface Science,* vol. 585, p. 152605, 2022.

[36] Ohlinger, W. S. and Klunzinger, P. E. and Deppmeier, B. J. and Hehre, W. J., "Efficient Calculation of Heats of Formation," *The Journal of Physical Chemistry A,* vol. 113, no. 10, pp. 2165-2175, 2009.

[37] Prabir Basu, "Biomass Gasification, Pyrolysis and Torrefaction," *Academic Press,* pp. 49-91, 2018.

[38] J.M. Seddon and J.D. Gale, "Thermodynamics and statistical mechanics Cambridge," *Royal Society of Chemistry,* 2001.

[39] S. Boucetta, F. Zegrar, "Density functional study of elastic, mechanical and thermodynamic properties of MgCu with a CsCl-type structure," *Journal of Magnesium and Alloys,* vol. 1, pp. 128-133, 2013.

[40] M. M. A. C. M. S. D.A. Papaconstantopoulos, "Tight-binding method in electronic structure," in *Reference Module in Materials Science and Materials Engineering*, Elsevier, 2022.

[41] Vajeeston, P. and Fjellvåg, H, "First-principles study of structural stability, dynamical and mechanical properties of Li_2FeSiO_4 polymorphs," *Royal Society of Chemistry ,* vol. 7, pp. 16843-16853, 2017.

[42] Andrew Horwood, Nachiappan Chockalingam, "Principles of materials science," in *Clinical Biomechanics in Human Locomotion*, Academic Press, 2023, pp. 91-174.

[43] Sanjeev Rajput, Naresh Kumar Thakur, “Chapter 5 - Rock Properties,” in *Geological Controls for Gas Hydrate Formations and Unconventionals*, Elsevier, 2016, pp. 131-164.

[44] Fabian Konstantiniuk, Martin Krobath, Werner Ecker, Christoph Czettl, Nina Schalk, Michael Tkadletz, “Influence of the aspect ratio of the micro-cantilever on the determined Young’s modulus using the Euler-Bernoulli equation,” *Materials Today Communications,* vol. 35, p. 106225, 2023.

[45] K.K. Phani, Dipayan Sanyal, “The relations between the shear modulus, the bulk modulus and Young's modulus for porous isotropic ceramic materialS,” *Materials Science and Engineering: A,* vol. 490, pp. 305-312, 2008.

[46] Michael Y. Toriyama, Alex M. Ganose, Maxwell Dylla, Shashwat Anand, Junsoo Park, Madison K. Brod, Jason M. Munro, Kristin A. Persson, Anubhav Jain, G. Jeffrey Snyder, “How to analyse a density of states,” *Materials Today Electronics,* vol. 1, p. 100002, 2022.

[47] Suraj Kumar, Shisak Sharma, Rituparna Karmaker, Dipak Sinha, “DFT study on the structural, optical and electronic properties of platinum group doped graphene,” *Materials Today Communications,* vol. 26, p. 101755, 2021.

[48] Yeo, Byung Chul, Kim, Donghun, Kim, Chansoo, Han, Sang Soo, “Pattern Learning Electronic Density of States,” *Scientific Reports,* vol. 9, p. 5879, 2019.

[49] Mintmire, J. W. and White, C. T., “Universal Density of States for Carbon Nanotubes,” *Physical Review Letters,* vol. 81, pp. 2506-2509, 1998.

[50] Abayev I, Zaban A, Kytin V.G, Danilin A.A, Garcia-Belmonte G and Bisquert J, “Properties of the electronic density of states in TiO_2 nanoparticles surrounded with aqueous electrolyte,” *Journal of Solid State Electrochem ,* vol. 11, p. 2007, 647-653.

[51] Movilla J.L, Garcia-Belmonte G, Bisquert J and Planelles J, “Calculation of electronic density of states induced by impurities in TiO_2 quantum dots,” *Physical Review B,* vol. 72, pp. 153313(1)-153313(4), 2005.

[52] S. Francis Amalraj, Daniel Sharon, Michael Talianker, Christian M. Julien, Luba Burlaka, Ronit Lavi, Ekaterina Zhecheva, Boris Markovsky, Ella Zinigrad, Daniela Kovacheva, Radostina Stoyanova, Doron Aurbach,, “Study of the nanosized Li_2MnO_3: Electrochemical behavior, structure, magnetic properties, and vibrational modes,” *Electrochimica Acta,* vol. 97, pp. 259-270, 2013.

[53] Boulineau, A. and Croguennec, L. and Delmas, C. and Weill, F, “Reinvestigation of Li_2MnO_3 Structure: Electron Diffraction and High Resolution TEM,” *Chemistry of Materials,* vol. 21, pp. 4216-4222, 2009.

[54] R. Veena, J. Anbu Dinesh, S. Raman, P. Panigrahi, N. Ganapathi Subramaniam, “Li and Mn-rich $Li_4Mn_5O_{12}$–Li_2MnO_3 composite cathode for next generation lithium-ion batteries.,” *Journal of Energy Storage,* vol. 24, p. 100754, 2019.

[55] S.H. Kim, S.J. Kim, K.S. Nahm, H.T. Chung, Y.S. Lee, J. Kim, “Synthesis of Li_2MnO_3-like electrode materials by reaction in solutions,” *Journal of Alloys and Compounds,* vol. 449, no. 1–2, pp. 339-342, 2008.

[56] Mitsuharu Tabuchi, Yoko Nabeshima, Tomonari Takeuchi, Kuniaki Tatsumi, Junichi Imaizumi, Yoshiaki Nitta, “Fe content effects on electrochemical properties of Fe-substituted Li_2MnO_3 positive electrode material,” *Journal of Power Sources,* vol. 195, no. 3, pp. 834-844, 2010.

[57] Mitsuharu Tabuchi, Yoko Nabeshima, Tomonari Takeuchi, Hiroyuki Kageyama, Kuniaki Tatsumi, Junji Akimoto, Hideka Shibuya, Junichi Imaizumi, “Synthesis and electrochemical characterization of Fe and Ni substituted Li_2MnO_3—An effective means to use Fe for constructing “Co-free” Li_2MnO_3 based positive electrode material,” *Journal of Power Sources,* vol. 196, no. 7, pp. 3611-3622, 2011.

[58] Daisuke Mori, Hikari Sakaebe, Masahiro Shikano, Hiroshi Kojitani, Kuniaki Tatsumi, Yoshiyuki Inaguma, “Synthesis, phase relation and electrical and electrochemical properties of ruthenium-substituted Li_2MnO_3 as a novel cathode material,” *Journal of Power Sources,* vol. 196, no. 16, pp. 6934-6938, 2011.

[59] Xin Dong, Youlong Xu, Lilong Xiong, Xiaofei Sun, Zhengwei Zhang, “Sodium substitution for partial lithium to significantly enhance the cycling stability of Li_2MnO_3 cathode material,” *Journal of Power Sources,* vol. 243, pp. 78-87, 2013.

[60] Jay Hyok Song, Andrei Kapylou, Hee Sung Choi, Byong Yong Yu, Evegeniya Matulevich, Sun Ho Kang, “Suppression of irreversible capacity loss in Li-rich layered oxide by fluorine doping,” *Journal of Power Sources,* vol. 313, pp. 65-72, 2016.

[61] J.P. Perdew and Y. Wang, “Accurate and simple analytic representation of the electron-gas correlation energy,” *Physical Review B,* vol. 45, 1992.

[62] P. Hohenberg and W. Kohn, “Inhomogeneous Electron Gas,” *Physical Review B,* vol. 136, 1964.

[63] W. Kohn and L.J. Sham, “Self consistent equation including exchange and correlation effect,” *Physical Review A,* vol. 140, 1965.

[64] S. Kurth, M.A.L. Marques, E.K.U. Gross, “Density-Functional Theory,” *Encyclopedia of Condensed Matter Physics,* pp. 395-402, 2005.

[65] Miguel A.L. Marques, Micael J.T. Oliveira, Tobias Burnus, “A library of exchange and correlation functionals for density functional theory,” *Computer Physics Communications,* vol. 183, pp. 2272-2281, 2012.

[66] Parr R.G, “Density Functional Theory of Atoms and Molecules,” *Horizons of Quantum Chemistry,* pp. 5-15, 1980.

[67] Vosko S.H, Wilk L and Nusair M, “Accurate spin-dependent electron liquid correlation energies for local spin density calculations: a critical analysis,” *Canadian Journal of Physics,* vol. 58, pp. 1200-1211, 1980.

[68] Perdew J.P and Zunger A, “Self-interaction correction to density-functional approximations for many-electron systems,” *Physical Review B,* vol. 23, pp. 5048-5079, 1981.

[69] Chakraverty M, Kittur H.M and Kumar P.A, “First Principle Simulations of Various Magnetic Tunnel Junctions for Applications in Magnetoresistive Random Access Memories,” *Transactions on Nanotechnology,* vol. 12, pp. 971-977, 2013.

[70] Horn K and Scheffler M, “Electronic Structure,” *Elsevier,* vol. 2, pp. 9-17, 2000.

[71] Ceperley D.M and Alder B.J, “Ground state of the electron gas by a stochastic method,",” *Physical Review Letters,* vol. 45, pp. 566-569, 1980.

[72] Becke A.D, “Density-functional exchange-energy approximation with correct asymptotic behaviour,” *Physical review A,* vol. 38, pp. 3098-3100, 1988.

[73] Perdew J.P, “Density-functional approximation for the correlation energy of the inhomogeneous electron gas,” *Physical Review B,* vol. 33, pp. 8822-824, 1986.

[74] Becke A.D, “Density-functional exchange-energy approximation with correct asymptotic behavior,” *Physical review A,* vol. 38, pp. 3098-3100, 1998.

[75] Perdew J.P and Wang Y, “Accurate and simple analytic representation of the electron-gas correlation energy,” *Physical Review B,* vol. 45, pp. 13244-13249, 1992.

[76] Perdew J.P, Burke K and Ernzerhof M, “Generalized Gradient Approximation Made Simple,” *Physical review letters,* vol. 77, pp. 3865-3888, 1996.

[77] Wimmer J and Andzelm E, “Density functional Gaussian-type-orbital approach to molecular geometries, vibrations, and reaction energies,” *The Journal of Chemical Physics,* vol. 96, pp. 1280-1303, 1992.

[78] Perdew J.P, “Density-functional approximation for the correlation energy of the inhomogeneous electron gas,” *Physical Review B,* vol. 33, pp. 8822-8824, 1986.

[79] Cohen D. J and Chadi M. L, “Special Points in the Brillouin Zone,” *Physical Review B,* vol. 8, pp. 5747-5735, 1973.

[80] Pack H.J and Monkhorst J.D, “Special points for Brillouin-zone integrations,” *Physical review B,* vol. 13, pp. 5188-5192, 1976.

[81] Blöchl P.E, “Projector augmented-wave method,” *Physical review B,* vol. 50, pp. 17953-17979, 1994.

[82] Pierre Strobel, Bernadette Lambert-Andron, “Crystallographic and magnetic structure of Li_2MnO_3,” *Journal of Solid State Chemistry,* vol. 75, pp. 90-98, 1988.

[83] Qu Wu, Bing He, Tao Song, Jian Gao, Siqi Shi, “Cluster expansion method and its application in computational materials science,” *Computational Materials Science,* vol. 125, pp. 243-254, 2016.

[84] Sergios Theodoridis, “Monte Carlo Methods,” *Machine Learning, Academic Press,* pp. 707-744, 2015.

[85] J. M. Sanchez, F. Ducastelle, and D. Gratias, “Generalized cluster description of multicomponent systems,” *Physica A: Statistical and Theoretical Physics,* vol. 128, p. 334, 1984.

[86] D Lerch and O Wieckhorst and G L W Hart and R W Forcade and S Müller, “UNCLE: a code for constructing cluster expansions for arbitrary lattices with minimal user-input,” *Modelling and Simulation in Materials Science and Engineering,* vol. 17, no. 5, p. 055003, 2009.

[87] Seko, Atsuto and Koyama, Yukinori and Tanaka, Isao, “Cluster expansion method for multicomponent systems based on optimal selection of structures for density-functional theory calculations,” *Phys. Rev. B,* vol. 80, no. 16, pp. 1-7, 2009.

[88] Volker Blum, Gus L. W. Hart, Michael J. Walorski, and Alex Zunge, “Using genetic algorithms to map first-principles results to model Hamiltonians: Application to the generalized Ising model for alloys,” *Phys. Rev. B,* vol. 72, no. 16, pp. 165-185, 2005.

[89] Maurice Gonon, “Case Studies in the X-ray Diffraction of Ceramics,” *Encyclopedia of Materials: Technical Ceramics and Glasses,* vol. 1, pp. 560-577, 2021.

[90] Seifollah Nasrazadani, Shokrollah Hassani, “Chapter 2 - Modern analytical techniques in failure analysis of aerospace, chemical, and oil and gas industries,” in *Handbook of Materials Failure Analysis with Case Studies from the Oil and Gas Industry*, Butterworth-Heinemann, 2016, pp. 39-54.

[91] N. Fleck, H. Amli, V. Dhanak, Waqar Ahmed, “Characterization techniques in energy generation and storage,” *Emerging Nanotechnologies for Renewable Energy,* pp. 259-285, 2021.

[92] Nidhi Raval, Rahul Maheshwari, Dnyaneshwar Kalyane, Susanne R. Youngren-Ortiz, Mahavir B. Chougule, Rakesh K. Tekade, “Importance of Physicochemical Characterization of Nanoparticles in Pharmaceutical Product Development,” in *Basic Fundamentals of Drug Delivery*, Academic Press, 2019, pp. 369-400.

[93] Macdonald, H., “Geologic Puzzles: Morrison Formation, Starting Point,” 9 September 2004. [Online]. Available:

http://serc.carleton.edu/introgeo/interactive/examples/morrisonpuzzle.html. [Accessed 4 April 2023].

[94] Mukesh Kumar Singh, Annika Singh, “Scanning electron microscope,” in *Characterization of Polymers and Fibres*, Woodhead Publishing, pp. 387-419. 2022.

[95] Franzini, M and Leoni, L and Saitta, M, “A simple method to evaluate the matrix effects in X-Ray fluorescence analysis,” *X-ray Spectrometry,* vol. 1, pp. 151-154, 1972.

[96] Yong-Joon Choi, Kazuaki Sawada, “Physical Sensors: Fluorescence Sensors,” in *Encyclopedia of Sensors and Biosensors (First Edition)*, Elsevier, pp. 1-19. 2023.

[97] Abbireddy, Chandra OR, and Chris RI Clayton, “A review of modern particle sizing methods,” *Proceedings of the Institution of Civil Engineers-Geotechnical Engineering,* vol. 162, no. 4, pp. 193-201, 2009.

[98] ISO13320 (2009) Particle size analysis, “Laser diffraction methods,” Dansk standard, 2009.

[99] Oukahou, Said and Maymoun, Mohammad and Elomrani, Abdelali and Sbiaai, Khalid and Hasnaoui, Abdellatif, “Enhancing the Electrochemical Performance of Olivine $LiMnPO_4$ as Cathode Materials for Li-Ion Batteries by Ni–Fe Codoping,” *ACS Applied Energy Materials,* vol. 5, no. 9, pp. 10591-10603, 2022.

[100] Pierre Strobel, Bernadette Lambert-Andron, “Crystallographic and magnetic structure of Li_2MnO_3,” *Journal of Solid State Chemistry,* vol. 75, no. 1, pp. 90-98, 1988.

[101] Murat Çanlı, Esin İlhan, Nihat Arıkan, “First-principles calculations to investigate the structural, electronic, elastic, vibrational and thermodynamic properties of the full-Heusler alloys X2ScGa (X = Ir and Rh),” *Materials Today Communications,* vol. 26, pp. 198-207, 2021.

[102] Christelle Ivane Azambou, Fredy Harcel Kamgang Djioko, Osita Obineche Obiukwu, Patrice Kenfack Tsobnang, Egwu Eric Kalu, Ignas Tonle Kenfack, Emeka Emmanuel Oguzie, “Structural, electronic, mechanical and thermodynamic

properties of lithium-rich layered oxides cathode materials for lithium-ion battery: Computational study," *Materials Today Communications,* vol. 35, p. 105738, 2023.

[103] Zhi-jian Wu, Er-jun Zhao, Hong-ping Xiang, Xian-feng Hao, Xiao-juan Liu, and Jian Meng, "Crystal structures and elastic properties of superhard IrN_2 and IrN_3 from first principles," *Phys. Rev. B,* vol. 76, no. 5, p. 15, 2007.

[104] Georgia Kimbell, Mohammad A. Azad, "Chapter FIFTEEN - 3D printing: Bioinspired materials for drug delivery," *Bioinspired and Biomimetic Materials for Drug Delivery,* pp. 295-318, 2021.

[105] R. Marchiori, "Mathematical Fundamentals of Nanotechnology," *Nanostructures,* pp. 209-232, 2017.

[106] Fatima, Yangchao Liao, Sara A. Tolba, Luis Alberto Ruiz Pestana, Wenjie Xia, "Electronic structure and density functional theory," in *Fundamentals of Multiscale Modeling of Structural Materials*, Elsevier, 2023, pp. 3-35.

[107] E.V. Lanina, V.D. Zhuravlev, L.V. Ermakova, A.N. Petrov, A.V. Pachuev, N.V. Sheldeshov, "ELECTROCHEMICAL PERFORMANCES OF COMPOSITE CATHODE MATERIALS $Li_{1.2}Ni_{0.17}Co_{0.10}Mn_{0.53}O_2$ and $Li_{1.2}Ni_{0.2}Mn_{0.6}O_2$," *Electrochimica Acta,* vol. 212, pp. 810-821, 2016.

[108] Nakamura, Takashi and Ohta, Kento and Kimura, Yuta and Tsuruta, Kazuki and Tamenori, Yusuke and Aso, Ryotaro and Yoshida, Hideto and Amezawa, Koji, "Impact of Oxygen Defects on Electrochemical Processes and Charge Compensation of Li-Rich Cathode Material $Li_{1.2}Mn_{0.6}Ni_{0.2}O_{2-\delta}$," *ACS Applied Energy Materials,* vol. 3, no. 10, pp. 9703-9713, 2020.

[109] Guo, Qing and Lau, Kah Chun and Pandey, Ravindra, "Thermodynamic and Mechanical Stability of Crystalline Phases of Li_2S_2," *The Journal of Physical Chemistry C,* vol. 123, no. 8, pp. 4674-4681, 2019.

[110] Peter Dowben, "Half Metallic Ferromagnets," *Journal of Physics: Condensed Matter,* vol. 19, no. 31, p. 310301, 2007.

[111] Peng Liu, Dengfu Chen, Qinzheng Wang, Pei Xu, Mujun Long, Huamei Duan, "Crystal structure and mechanical properties of nickel–cobalt alloys with different

compositions: A first-principles study," *Journal of Physics and Chemistry of Solids,* vol. 137, p. 109194, 2020.

[112] Lee, G. H., Lim, J., Shin, J., Hardwick, L. J., & Yang, W., "Towards commercialization of fluorinated cation-disordered rock-salt Li-ion cathodes," *Frontiers in Chemistry,* vol. 11, p. 1098460, 2023.

[113] Andrew Horwood, Nachiappan Chockalingam, "Principles of materials science," in *Clinical Biomechanics in Human Locomotion*, Academic Press, 2023, pp. 91-174.

[114] S.F. Pugh, "Relations between the elastic moduli and the plastic properties of polycrystalline pure metals," *The London, Edinburgh, and Dublin Philosophical Magazine and Journal of Science,* vol. 45, no. 367, pp. 823-843, 1954.

[115] G. Wang, X. Wang, L. Yi, L. Wang, R. Yu, M. Liu, D. Wang, Q. Ren, , "The effects of $LiTi_2(PO_4)_3$ modification on the performance of spherical $Li_{1.5}Ni_{0.25}Mn_{0.75}O_{2+\delta}$ cathode material," *Royal Society of Chemistry,* vol. 6, p. 46325, 2016.

[116] Noko Ngoepe, Arturo Gutierrez, Pallab Barai, Jiajun Chen, Phuti E. Ngoepe, Jason R. Croy, "The effects of process parameters on the properties of manganese-rich carbonate precursors," *Chemical Engineering Science,* vol. 241, p. 116694, 2021.

[117] E.V. Lanina, V.D. Zhuravlev, L.V. Ermakova, A.N. Petrov, A.V. Pachuev, N.V. Sheldeshov, "Electrochemical Performances Of Composite Cathode Materials $Li_{1.2}Ni_{0.17}Co_{0.10}Mn_{0.53}O_2$ and $Li_{1.2}Ni_{0.2}Mn_{0.6}O_2$," *Electrochimica Acta,* vol. 212, pp. 810-821, 2016.

[118] Hyeongseon Choi, Annika Regitta Schuer, Hyein Moon, Matthias Kuenzel, Stefano Passerini, "Investigating the particle size effect on the electrochemical performance and degradation of cobalt-free lithium-rich layered oxide $Li_{1.2}Ni_{0.2}Mn_{0.6}O_2$," *Electrochimica Acta,* vol. 430, p. 141047, 2022.

[119] Sangchoon KIM and Kyoungsoo SON and Bongsoon KANG, "An ML Timing Estimator in UWB Communication Systems," *IEICE Transactions on Communications,* vol. E91.B, pp. 339-342, 2008.